Study of momentum correlations in ultra-relativistic proton-proton and heavy-ion collisions

Mads Stormo Nilsson

Thesis submitted as requirement for the degree PhD

Department of Physics, University of Oslo

2012

Fysisk institutt, Universitetet i Oslo

Series of dissertations submitted to the
Faculty of Mathematics and Natural Sciences, University of Oslo
No. 1304

ISSN 1501-7710

Cover: Inger Sandved Anfinsen.
Printed in Norway: AIT Oslo AS.

Produced in co-operation with Akademika publishing.
The thesis is produced by Akademika publishing merely in connection with the thesis defence. Kindly direct all inquiries regarding the thesis to the copyright holder or the unit which grants the doctorate.

Preface

This thesis represent the results of nearly five years of work with femtoscopic correlations of particles produced in heavy-ion collisions. The thesis presents both studies of published experimental results using numerical models, and analysis of recent data from the ALICE experiment at CERN. A lot of time has been devoted to the process of fitting the data in order to extract the femtoscopic observables. The fitting process is not only a source of statistical errors, but also helps to fuel our understanding of the non-femtoscopic correlations which might be present and must be accounted for. The identification and removal of such backgrounds form the majority of the work in the experimental analysis presented.

The thesis is structured as follows:

- Chapter 1 gives a general introduction to the subject of heavy-ion collisions, the history of the field, the theory and the current status.
- Chapter 2 presents in detail the ALICE experiment, introducing the experimental setup and the many different experimental observables.
- Chapter 3 is dedicated to the underlying theory of femtoscopic correlations. Formalism for both identical and non-identical correlations is presented, along with implementation for models and experiments. Recent results from the ALICE experiment are discussed.
- Chapter 4 discusses numerical models for heavy-ion collisions. Microscopic models are presented in detail, with both theory and current results.
- Chapter 5 presents the results obtained with the QGSM model and compares them to published data from the STAR and ALICE experiments.
- Chapter 6 includes the experimental analysis of pion-kaon correlations in the ALICE experiment. Particle identification is discussed, as well as the fitting procedures. The main topic is the removal of the complicated non-femtoscopic background. Results from the PYTHIA model is used as a reference in the study.
- Chapter 7 draws the conclusions and contains the finishing remarks.
- Part II of the thesis includes published papers.

Acknowledgements

This has been a long road. When you stumble it is nice to have somebody to help you to keep going forward. Many people deserve thanks for their support whatever form it came in. If I forget someone I beg your forgiveness. In no particular order they are:

My supervisors Larissa Bravina and Trine Tveter. Evgeny Zabrodin who is always available to give his valuable advice, and who has probably read more revisions of the thesis than anyone. Ludmila Malinina who has helped me more than I probably deserve, and who have despaired when I sometimes took a little to long answering my mails. Adam Kisiel for his advice and help.

Rodion Kolavatov who have been helpful with my struggles in understanding string models. Guylnara Eyyubova who have shared my struggles as a fellow PhD student in the group.

My parents and my sister who have always been supportive of my education. All my friends who have given me a social life and probably strength to go on.

My girlfriend.

Mads Stormo Nilsson 31. Oct 2012

Contents

List of Figures

List of Tables

List of papers

Paper I: M. S. Nilsson, L. V. Malinina, J. Bleibel, L. Bravina, E. Zabrodin,
Study of $\pi\pi$ Correlations at RHIC and LHC Energies in pp Collisions within the Quark-Gluon String Model,
Phys. Part. Nucl. Lett. **8** (2011) 1000-1003.

Paper II: M. S. Nilsson, L. Bravina, E. Zabrodin, L. V. Malinina, J. Bleibel,
Study of $\pi\pi$ correlations at LHC and RHIC energies in pp collisions within the quark-gluon strong model,
Phys. Rev. **D84**, 054006 (2011).

Paper III: L. Bravina, R. Kolevatov, L. Malinina, M. S. Nilsson, E. Zabrodin,
Bulk observables, long-range correlations and flow in pp collisions at LHC,
Acta. Phys. Polon. Supp. **5** (2012) 419-424.

Part I

Introduction

Chapter 1

Introduction

The idea that the world consists of small indivisible components was first introduced by early Greek and Indian philosophers. The term atom was coined by Democritus, from the Greek "atomos" meaning indivisible. This idea was revived in the early 17th century, giving birth to modern chemistry and later nuclear physics. In the beginning of the twentieth century the famous Geiger-Marsden experiments were conducted under the supervision of Ernest Rutherford [1]. The experiment, in which gold foil was bombarded with α-particles, revealed the nuclear nature of atoms. As more discoveries were made, driven by both experimental and theoretical activity, it became clear that the atom was not indivisible and consisted of even smaller parts.

The modern theory of interactions at subatomic level is known as the Standard Model. It includes electromagnetism, the strong nuclear force and the weak nuclear force. The elementary particles of the theory are the quarks, leptons, gauge particles and scalar particles. Quarks interact through all three forces of the model, and it is the lightest quarks that form the protons and neutrons which our world is predominately made of. The gauge particles are the photons, gluons, W and Z bosons. They are the force carriers of the theory. The Higgs boson is required by the theory to give particles mass, but was undiscovered until very recently. Recent discoveries made by the ATLAS and CMS collaborations shows the existence of a new particle which exhibit properties consistent with what is known of the Higgs boson [2, 3]. Both experiments have shown a high statistical significance for their results, and the newly discovered particle is highly likely the elusive Higgs boson. An overview of the elementary particles in the Standard Model can be seen in Fig. 1.1.

At small scales the strong nuclear force is dominant. The strong interaction part of the Standard Model is called Quantum Chromo Dynamics (QCD) [4], and governs the interactions of quarks and gluons. Predictions made by QCD have helped to fuel the large interest in high energy nuclear physics the last 30 years.

1.1 Quantum Chromo Dynamics

QCD is a quantum theory of dynamical interactions between quarks and gluons, which both carry the strong charge. In the model the strong charge comes in three variations, which have

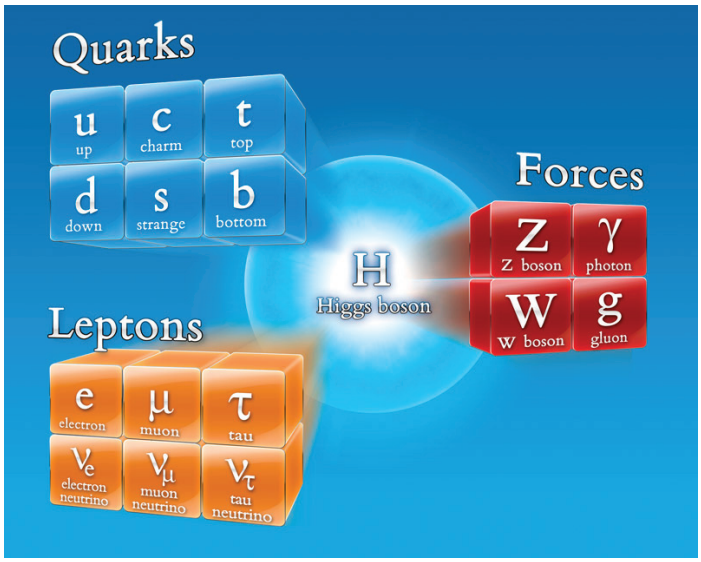

Figure 1.1: Elementary particles and force carriers in the Standard Model. Picture taken from [27]

been named red, blue and green. Consequently the strong charge is known as the colour charge, and the model is named Chromo after the Greek *kroma*, meaning colour.

The gluons are the force carriers of QCD. The force carrier of electromagnetism, the photon, is electrically neutral and the force carriers of the weak nuclear force, W and Z, do not carry the weak charge. The gluons however carry a colour charge, this makes strong interactions extremely complex as the boson force carriers can also interact with each other or the quarks.

The strength of the strong interaction is governed by the effective coupling constant α_S. It has been found through experiments to be dependent on the energy scale of the interaction as shown in Fig. 1.2. The interaction is much stronger at low energy scales (large distances) than at high energy scales (small distances). If we move two quarks apart the strong interaction between them becomes stronger as the distance increases, the only way for the quarks to move freely is at high energy scales, meaning short distances. This is known as *asymptotic freedom* and is the complete opposite to the forces we are able to observe daily, gravity and electromagnetism. A direct consequence of this is the phenomenon known as quark confinement. All observed particles are colour neutral as a result, meaning they consist of either three quarks with three different colour charges (baryons), or they consist of a quark anti-quark pair (mesons). Predictions have been made of exotic particles such as pentaquarks [5] consisting of four quarks and an anti-quark, but have never been observed.

One way to understand quark confinement is through the string picture. We can imagine that the colour field between two or more quarks is isolated in a colour flux tube, known as a string.

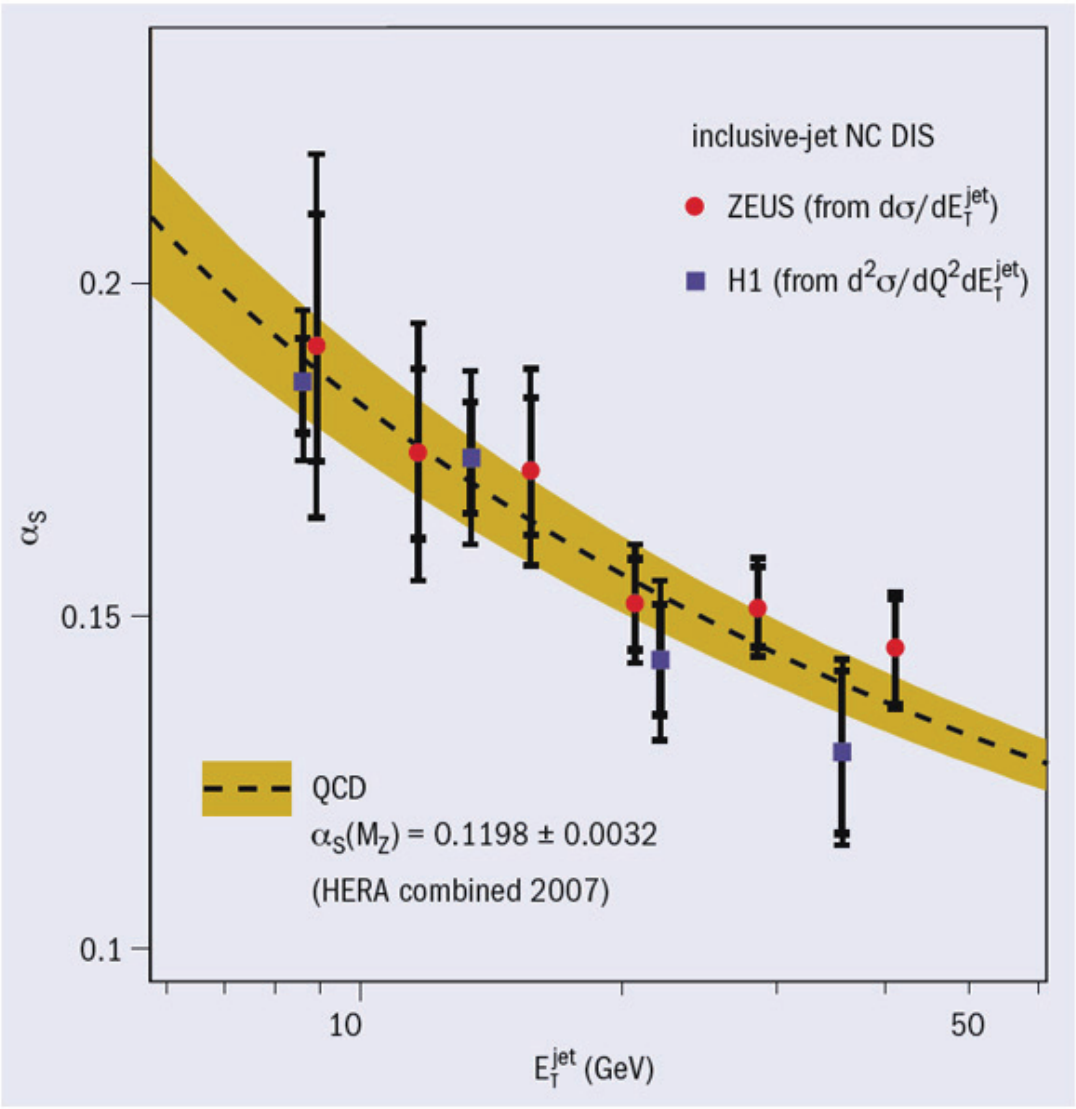

Figure 1.2: The dependence of the strong coupling constant as a function of energy scale. Picture taken from [6]

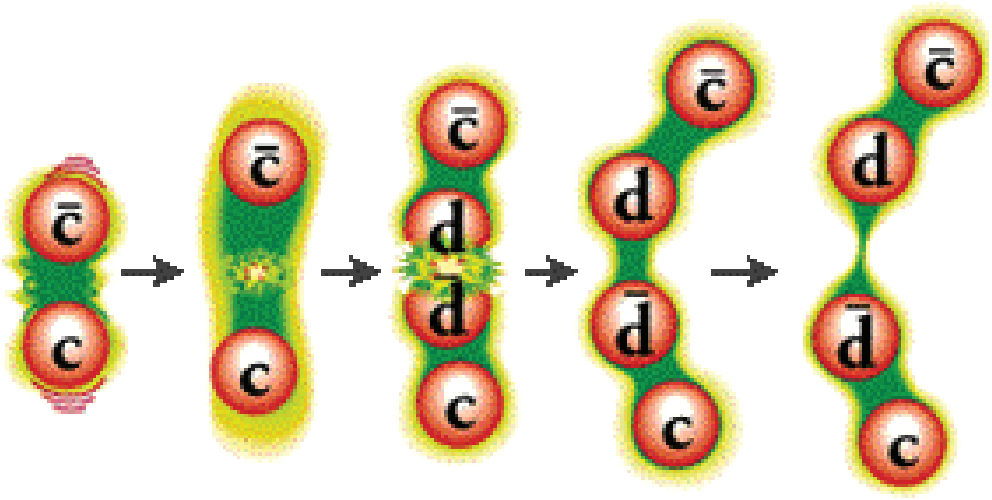

Figure 1.3: Illustration of the creation of new particles when attempting to separate two quarks. Picture taken from [27]

As long as the quarks stay together they can move freely, forming a baryon of three quarks or a meson with a quark anti-quark pair. If you try to separate them the string will stretch, and as it stretches the strong interaction grows stronger and more and more energy is stored in it. At some point it will become more energetically favourable to create a new quark-antiquark pair rather than continuing to stretch the string. The new pair will couple to the existing quarks, forming new hadrons. The attempt to separate the two quarks have ended with particle production instead. This process is illustrated in Fig. 1.3, where a J/Ψ particle decays as the $c\bar{c}$ pair is separated and a $d\bar{d}$ pair is created. The d-quark couple to the $\bar{c}$ and vice versa, forming two D mesons.

The existence of asymptotic freedom has led to the prediction of a new phase of matter at very high densities and temperatures. At these high energies quarks are predicted to be deconfined and be able to move freely in a larger volume. This new form of matter, Quark Gluon Plasma (QGP) [7] is thought to have existed at the very beginning of our universe just after the Big Bang. The search for Quark Gluon Plasma and its properties has led to an intensive experimental effort to reproduce the high density and temperature of the early universe. The study of QGP allows us to understand the conditions of the early universe, and it probes extreme conditions of QCD. The specific properties of QGP means it will have a characteristic behaviour, different from all other forms of matter.

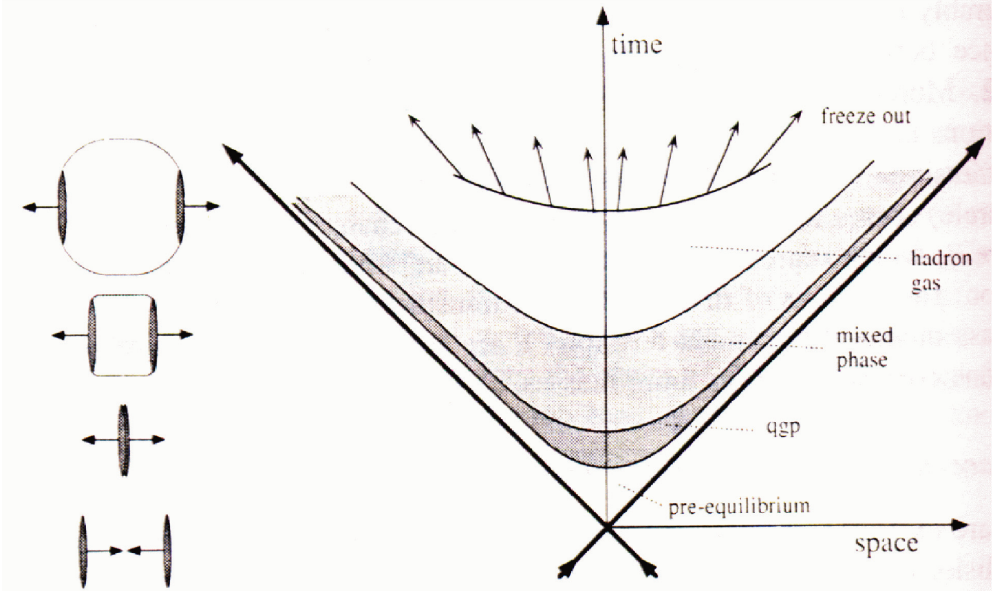

Figure 1.4: The evolution of a heavy-ion collision in the hydrodynamic model. Picture taken from [8].

1.2 Heavy-Ion Physics

Hot and dense nuclear matter can be created experimentally through ultra-relativistic heavy-ion collisions. Ions of heavy elements such as gold or lead are accelerated and collided in huge experimental facilities, creating highly energetic systems with large particle production. This particle production includes the creation of the heavier quarks, c, s, t, b, as well as baryons and mesons consisting of such quarks. These particles are often very short lived, decaying into more stable configurations. After more than 50 years of experimental activity the collision energy of heavy-ion collisions has seen a sharp rise. The Alternating Gradient Synchrotron at Brookhaven had a centre of mass energy of $\sqrt{s_{NN}} \approx 5\ GeV$, while the CERN LHC can go up to $\sqrt{s_{NN}} \approx 5.5\ TeV$.

A heavy-ion collision can be subdivided into distinct stages. In the initial state, pre-collision, the two nuclei are moving towards each other at relativistic speeds. Seen from the lab frame the nuclei are Lorentz contracted into flat "pancake" shapes. As they collide we get a pre-equilibrium stage of a hot and dense nuclear matter fireball. In this fireball the quark gluon plasma forms, and will rapidly reach thermal equilibrium. As the plasma expands hydrodynamically it will cool and the deconfined quarks will start forming hadrons. This mixed phase will end with chemical freeze-out and the hadronic stage will continue with expansion and elastic interactions until we get thermal freeze-out.

During this evolution the created matter will rapidly change both temperature and density. This means that heavy-ion collisions can be used as a tool to study the phase diagram of QCD. It is of great interest to study the phase transition from normal matter to QGP, and specifically whether it is a first or second order transition, and to search for a potential critical point in the phase diagram. The path the nuclear matter takes through the phase diagram is illustrated in Fig. 1.5. This diagram is rich in information and it is of interest to study it in more detail.

Along the x-axis we have baryonic chemical potential, and along the y-axis we have temperature. Vacuum is at the lower left of the diagram with zero temperature and chemical potential. At low temperature and medium chemical potential we find normal nuclear matter. And at higher chemical potential there exists different possible exotic states of matter such as colour superconductors and neutron stars. By increasing the temperature at low chemical potential, matter exists as a hadronic gas, a weakly interacting system of hadrons. By increasing the temperature further one can achieve a phase transition and form quark-gluon plasma. Somewhere along this phase transition a critical point might exist. At this critical point the first order quark-hadron phase transition is transformed to a second-order transition. After this point one will observe a smooth crossover between the phases.

The path taken by a heavy-ion collision in the diagram starts at normal nuclear matter, and quickly goes up in temperature and down in chemical potential. After the system reaches maximum temperature it will start cooling at a low chemical potential, and return to a hadron gas state. As seen in the figure different collision energies causes one to probe different parts of the phase diagram, and by using large enough collision energies the evolution of the system will mirror that of the early universe. In order to fully explore the properties of the phase diagram, collisions of many different energies are needed. This is the basis for the RHIC beam energy scan program which is being undertaken at BNL [9], and more such programs are being planned at the *GSI Helmholtz Centre for Heavy Ion Research* in Darmstadt and at the *Joint Institute for Nuclear Research* (JINR) in Dubna. The purpose of these programs is to probe the phase diagram at lower energies and search for the possible critical point.

In 2005 scientists at RHIC announced that they had produced a “perfect” liquid in their collisions hot enough to produce a quark soup [10, 11, 12, 13]. This QGP acted as a perfect liquid and not a gas, which came as a surprise, and led to an increased theoretical activity studying the hydrodynamical properties of quark matter. The old view was that the QGP is an “ideal gas” of weakly interacting partons. This paradigm was overturned by the successful application of hydrodynamic models to the experimental data from RHIC [14]. In particular the results demanded the equilibration time of the plasma to be less than $0.5\ fm/c$, while the equilibration time of an ideal gas is on the order of $3.5\ fm/c$. The new matter created at RHIC becomes a strongly interacting perfect liquid with viscosity close to zero, and QGP has turned into strongly interacting Quark Gluon Plasma (sQGP).

1.3 Proton-proton collisions

The main focus for most particle physics is proton-proton collisions. The main areas of study are the search for the Higgs boson as well as probing for possible super-symmetry. These stud-

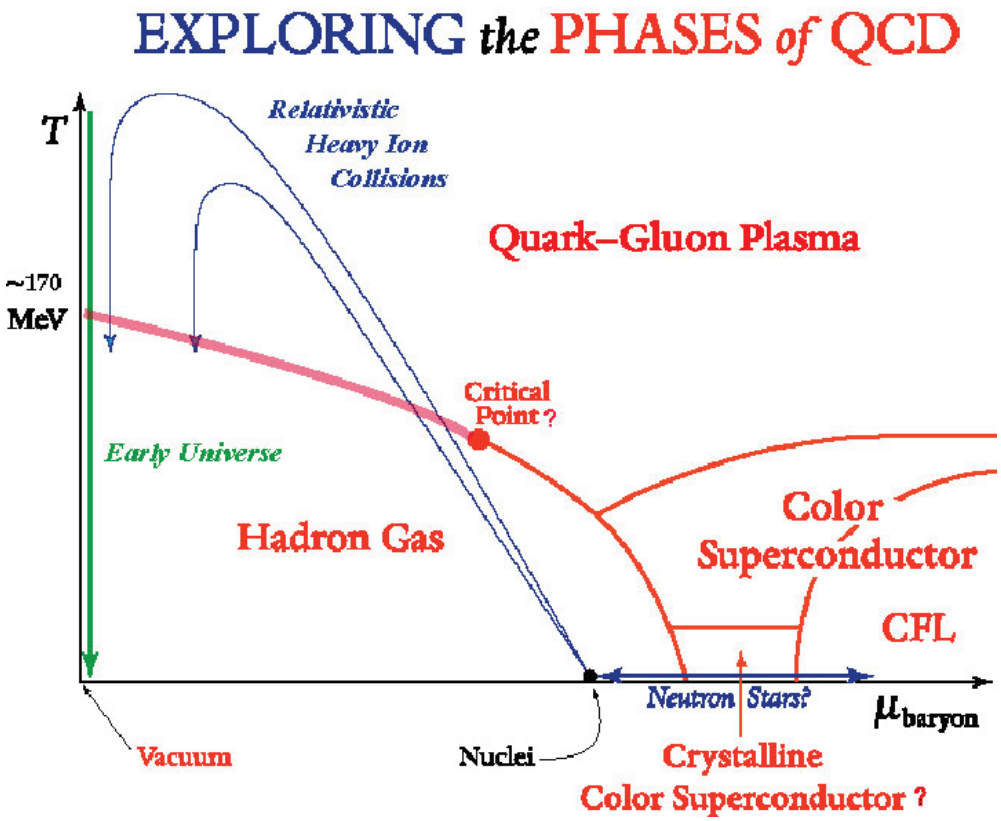

Figure 1.5: The phase diagram of QCD. Showing path of a Heavy-ion collision through the diagram, as well as potential exotic states of matter.

ies can reveal important information about elemental particle physics and the Standard Model, but proton-proton collisions can also be an important source of information from a heavy-ion perspective.

From a naive point of view one might think that a heavy-ion collision is nothing more than a scaled up proton-proton collision. The existence of collective effects however makes for a much more complicated picture. One can define the nuclear modification factor R_{AA} as the ratio of the invariant yield of a nucleus-nucleus collision to the scaled yield of a proton-proton collision.

$$R_{AA}(p_T) = \frac{d^2N_{AA}/d\eta dp_T}{\langle N_{coll}\rangle / \sigma_{pp}^{inel} d^2\sigma_{pp}/d\eta dp_T} \tag{1.1}$$

where $\langle N_{coll}\rangle$ is the average number of inelastic nucleus-nucleus collisions per event. In the absence of collective effects we expect $R_{AA} = 1$. For $R_{AA} < 1$ we have behaviour unique for heavy-ion collisions, such as jet quenching.

In addition there has also recently been an increased interest in measuring typical heavy-ion signals such as flow for proton-proton collisions. This is connected with the fact that proton-proton collisions at the LHC can reach energies far beyond what has been seen before, and these highly energetic protons might due to a large number of sea quarks behave more like heavy-ions and exhibit collective behaviour. In particular, event multiplicities reached in 7 TeV pp collisions at LHC [15] are comparable to those registered in peripheral AA collisions at RHIC, providing at interesting possibility to search for collectivity in pp interactions.

The study of such collective signals in pp collisions can reveal similarities and differences compared to the same signals in heavy-ion collisions. Energy scan programs might also be able to find at what energy collective behaviour starts to emerge in pp collisions.

Chapter 2

Experiments

Experimental efforts in the fields of particle and heavy-ion physics has been ongoing for over fifty years in laboratories all over the world. Some of the leading particle colliders today include the Large Hadron Collider (LHC) at CERN [16, 17], the Relativistic Heavy-Ion Collider (RHIC) at the Brookhaven National Laboratory (BNL) [18] and Tevatron at the Fermi National Accelerator Laboratory (Fermilab) [19]. This broad field of research is important because it allows for double-checking of important results, and for new facilities to be build using information gained at existing laboratories. Plans for upgrading existing facilities exist for both LHC and RHIC, as well as the building of new colliders in places such as GSI Darmstadt [20] and JINR Dubna [21]. The building of linear electron colliders is an exiting new prospect, which allows for precision measurement to be made of existing discoveries made with nucleus-nucleus colliding machines. Plans for linear electron colliders exist for both CERN (CLIC [22] or ILC [23]) and BNL (eRHIC [24]).

In this work the main focus will be to analyse proton-proton data taken at the ALICE experiment at CERN LHC [25], which will be described in greater detail below. In the theoretical part of the thesis data will also be compared with results from the STAR experiment at RHIC BNL [26]. RHIC is the second largest heavy-ion collider in the world, and was the first machine in the world capable of colliding beams of heavy ions. RHIC collides beams of gold ions head on at relativistic energies of up to $\sqrt{s} = 200\ GeV$. The STAR experiment is one of four experiments at RHIC, and specialises in tracking the thousands of particles created in heavy-ion collisions.

2.1 CERN and the Large Hadron Collider

Founded in 1954 along the Franco-Swiss border, CERN is the European Organization for Nuclear Research (Conseil Européen pour la Recherche Nucléaire). It is a multi-national collaboration run by 20 European member states, and whose activities also include those of numerous observer and non-member states. Scientists from 608 institutes from around the world uses CERN's facilities.

Founded after the second world war in order to unite European physicists and allow them to share the costs of nuclear physics facilities, the centre has been a pioneer for peaceful scientific

cooperation between nations during the years of the cold war.

The CERN site has expanded over the years as bigger and more powerful particle accelerators and colliders have been built in an ever growing search for answers about the fundamental nature of matter. This has culminated in the construction of the Large Hadron Collider (LHC) which is capable of colliding protons at an energy of up to $14\ TeV$ and lead ions at an energy of up to $5.5\ TeV$. The LHC ring houses four experiments which have been independently designed for different areas of study, but which also provide complementary results. The four experiments are the two general purpose experiments ATLAS and CMS whose main purpose is the search for the Higgs-boson and possible supersymmetries in pp collisions, LHCb which studies the nature of anti-matter, and the dedicated heavy-ion experiment ALICE. A schematic overview of the LHC ring can be found in Fig. 2.1. As seen in the figure a series of smaller accelerators are used to accelerate the colliding particles before they are injected into the LHC ring.

Although experiments at the LHC uses a proton beam for a majority of the time, collisions with heavy-ions are also performed. While the ATLAS [27], CMS [28] and LHCb [29] experiments are built and designed with proton-proton collisions in mind, and ALICE with heavy-ion collisions, all experiments except LHCb takes data during both types of collisions. The experimental focus of this thesis is to analyse proton-proton data taken by the ALICE experiment from the viewpoint of a heavy-ion physicist.

2.1.1 The ALICE experiment

The ALICE experiment is one out of four experiments at the LHC, and the only one designed specifically to study heavy-ion collisions. It was first suggested in [30], and it was approved of in February 1997.

The main role of ALICE is to make measurements of high energy heavy-ion collisions, in order to study and understand collective phenomena and macroscopic properties of dense and energetic quarkonic matter. Specifically the study of heavy-ion collisions probes the strong interactions of nuclear matter. Such studies allows a broadening understanding of the standard model, and an understanding of the conditions of the early universe. Data taken at ALICE will be from collisions which have by an order of magnitude higher energies than at RHIC, and will as such be able to test the extrapolation of the results obtained there. A schematic overview of the ALICE detector is shown in Fig. 2.2.

In addition to the study of heavy-ion physics, ALICE is also taking data during the proton-proton runs of the LHC. The study of proton-proton collision will not only provide important benchmarks that can be used as a reference in heavy-ion studies, such as the nuclear modification factor R_{AA} and physical observables such as multiplicity, but is also interesting in its own regard. In particular it has in later years become evident that one might also observe collective phenomena in high energy proton-proton collisions [31, 32]. The measurements of bulk properties in proton-proton physics can make clearer the origin of such phenomena also in heavy-ion collisions.

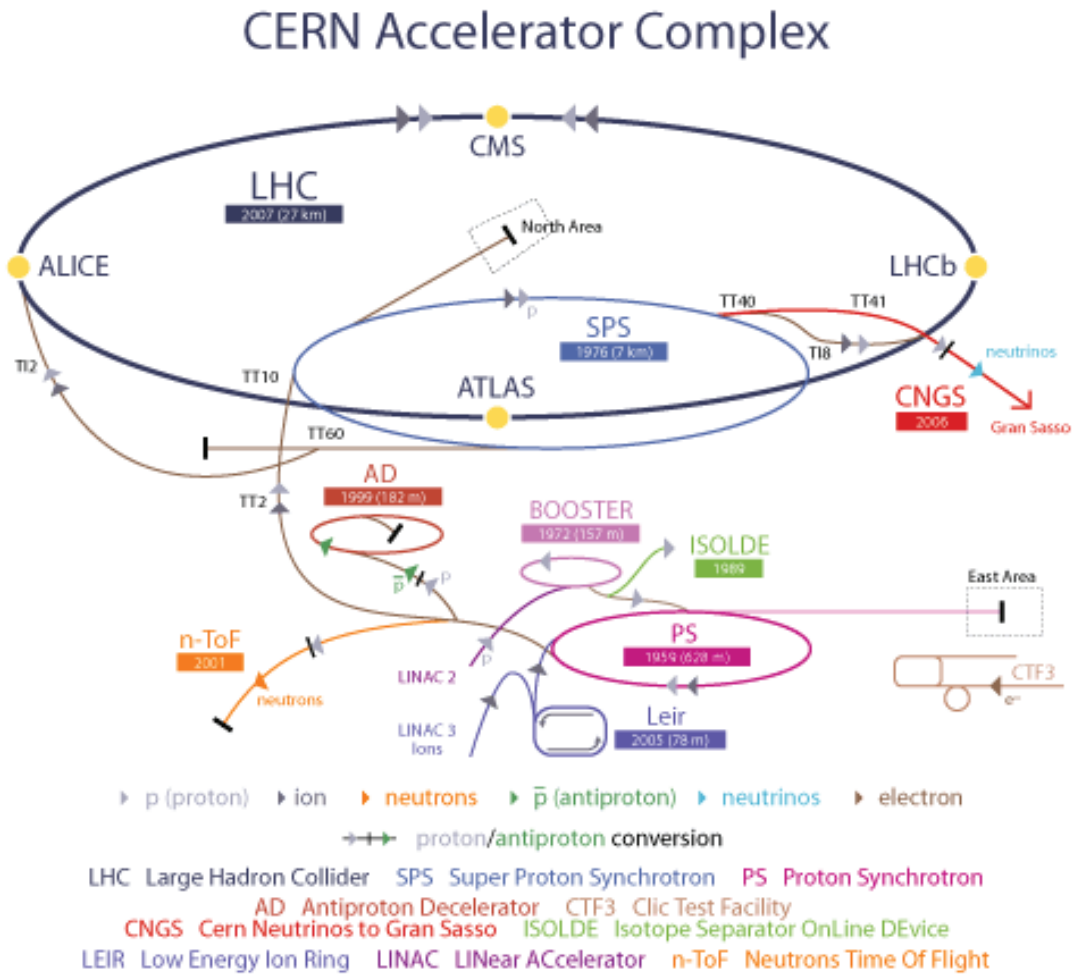

Figure 2.1: A schematic overview of the CERN accelerator complex. Image taken from [17]

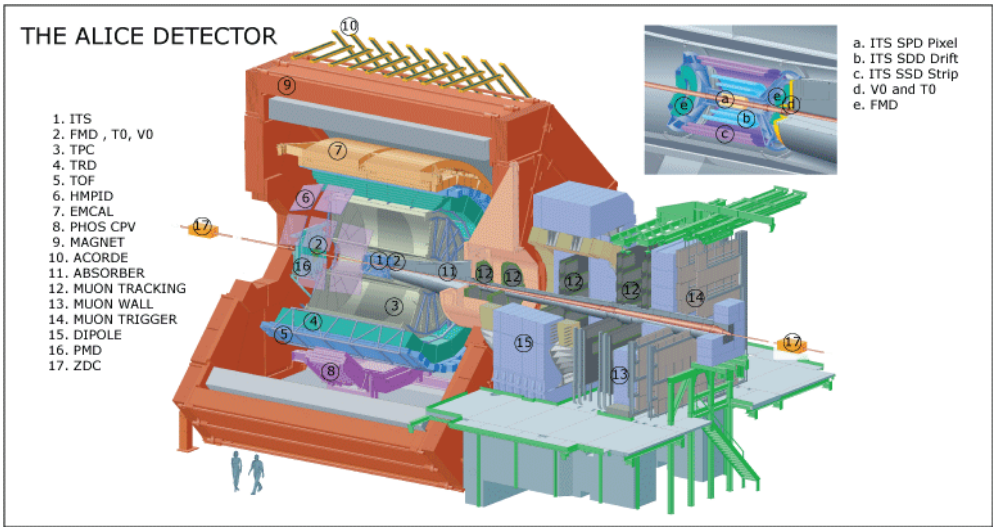

Figure 2.2: A schematic overview of the ALICE experiment. Figure taken from [25].

2.1.2 Experimental observables

The study of bulk phenomena relies on many experimental observables. These observables are often indirect effects of the phenomena that are being studied, and each observable constitutes a field of research on their own. It is important to note that all experimental observations are of a second hand nature. Particles in the detector are identified from the tracks they leave behind, and physical observables are constructed from this information. Even though giving a complete overview of is beyond the scope of this thesis some of these observables will be discussed in greater detail below.

Particle multiplicities

The most fundamental "day-one" observable is the average charged-particle multiplicity per rapidity unit: dN_{ch}/dy. It is related to the energy density of the system, and therefore enters the calculation of most other observables. The measurement of this quantity fixes the main unknowns in the detector performance, and largely determines the accuracy with which many observables can be measured.

There is no first-principles calculation that allows us to predict the multiplicity, this is due to the running coupling constant in QCD. The running coupling constant α_S is small for "hard" processes (large momentum transfer, $(p > 1\ GeV/c)$), but not for "soft" processes. Therefore for "soft" processes pertubative techniques (pQCD) doesn't work. Even at $\sqrt{s} = 14\ TeV$ many subprocesses at partonic level proceed via small momentum transfer $(p < 1\ GeV/c)$, i.e. these processes are "soft". As a result most theoretical predictions or extrapolations from SPS to RHIC

overshoot the measured experimental values as seen in Fig. 2.3. The increased multiplicity of ALICE is shown in Fig. 2.4 compared with earlier experiments, also shown is theoretical predictions. Many models, compensating for the RHIC results, ended up underpredicting the ALICE multiplicity.

The study of particle spectra yields information about the particles at freeze-out. This information constrains the dynamical evolution and gives indirect hints about the early stages of the collision. Of interest is the multiplicity distribution of the charged particle pseudorapidity and the charged particle transverse momentum. The experimentally measured pseudorapidity distributions of the ALICE collaboration are presented in Fig. 2.5, and the measured transverse momentum distributions are presented in Fig. 2.6.

Azimuthal correlations

The study of particle flow yields important information about the collective behaviour of the system. The different flow observables are given as the Fourier components of the transverse momentum distribution on the emission angle ϕ relative to the reaction plane [33, 34, 35]:

$$\frac{dN(b)}{m_t dy dm_t d\phi} = \frac{1}{2\pi}\frac{dN(b)}{m_t dy dm_t}\left(1 + 2\sum_{n=1}^{\infty} v_n(p_t, y)\cos[n(\phi)]\right) \tag{2.1}$$

The first component, known as the radial flow, is isotropic and thus always present even in central collisions. The two next components are the directed flow v_1 and elliptic flow v_2, which are anisotropic and arise from the asymmetries obtained in non-central collisions [36]. The radial flow is the azimuthally symmetric flow, in central collisions we expect the main flow component to be radial flow. The directed flow $v_1 = \frac{p_x}{\sqrt{p_x^2 + p_y^2}}$ has been measured at high energies to be close to zero at mid-rapidity. The elliptic flow is given as $v_2 = \frac{p_x^2 - p_y^2}{p_x^2 + p_y^2}$. An initial anisotropy in coordinate space will cause pressure gradients that will transform into an anisotropy in momentum space, as seen in Fig. 2.7.

The measurement of elliptic flow in heavy-ion collisions is an important indicator of collective behaviour. The evolution of the elliptic flow as a function of collision energy can give an important indication of the onset of QGP and its behaviour. Recent results from the ALICE experiment (Fig. 2.8) show that the plasma still behaves as a perfect liquid.

Higher moments of the flow (v_3, v_4, v_5 etc) can also be measured (Fig. 2.9) and correspond to higher order momentum anisotropies in the system. Interest in these higher moments of the flow has been renewed lately with the advent of using correlations in $\Delta\eta\Delta\phi$ as a technique to estimate the flow. These correlations give a wealth of information, including the femtoscopic peak at $\Delta\eta = \Delta\phi = 0$. The correlations for $2 < |\eta| < 5$ are expanded into a Fourier series with the coefficients $v_{n,n} = \langle\cos(n\Delta\phi)\rangle$ corresponding to the moments of the flow (Fig 2.10), this holds for moments of the flow larger than one [37].

There exist many different methods for measuring the flow in the system, including many particle correlation, event plane, Lee-Yang zero and scalar methods (see [38, 39] and references

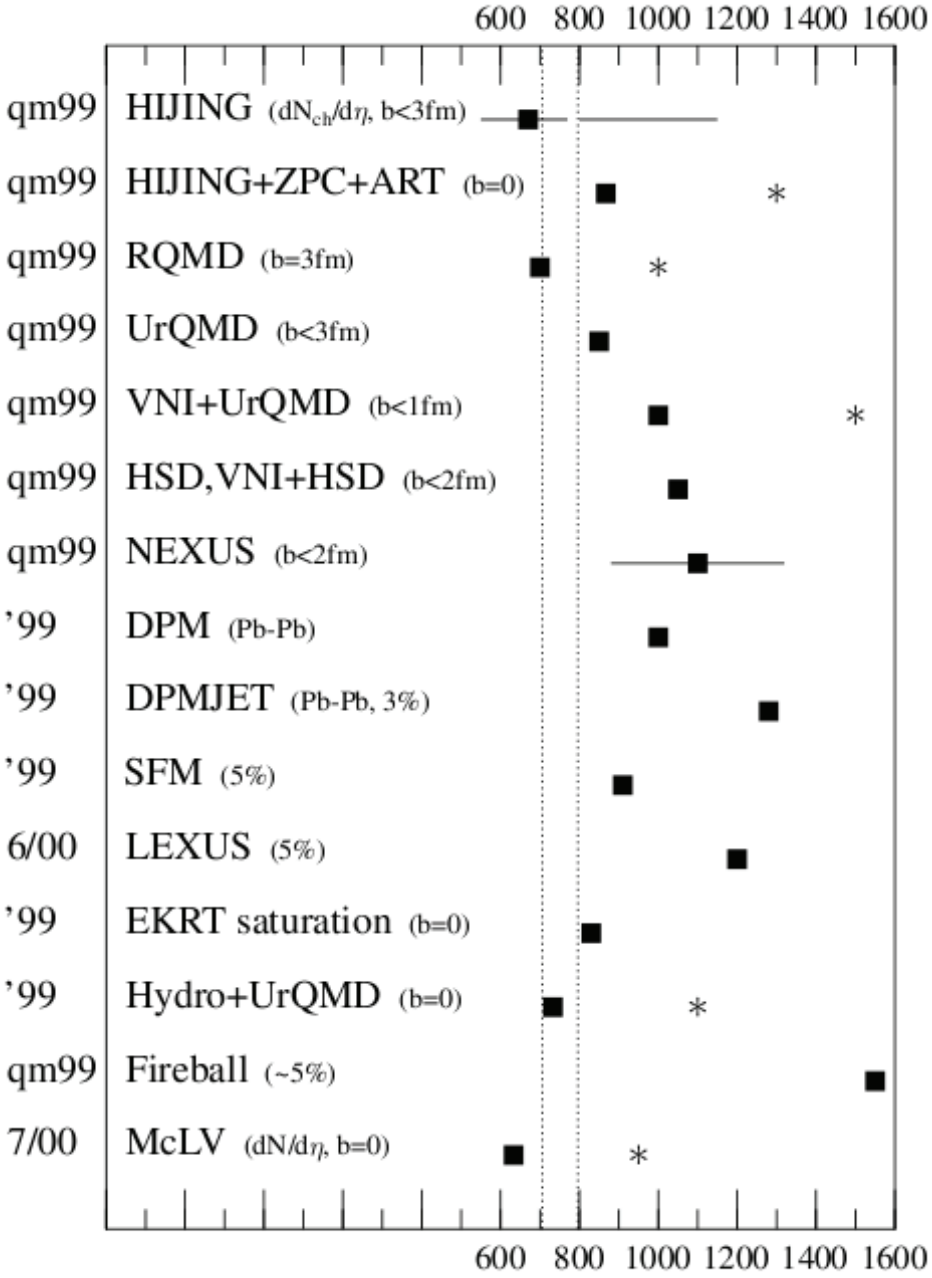

Figure 2.3: $dN_{ch}/d\eta$ calculated from different theoretical models compared with RHIC data (dotted lines). Figure taken from [40]

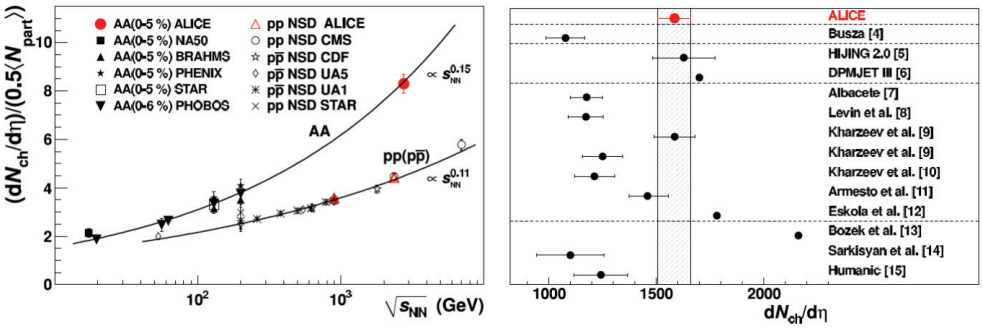

Figure 2.4: $dN_{ch}/d\eta$ measured in different experiments (left panel), and calculated from theoretical models compared to ALICE data (right panel). Figure taken from [41]

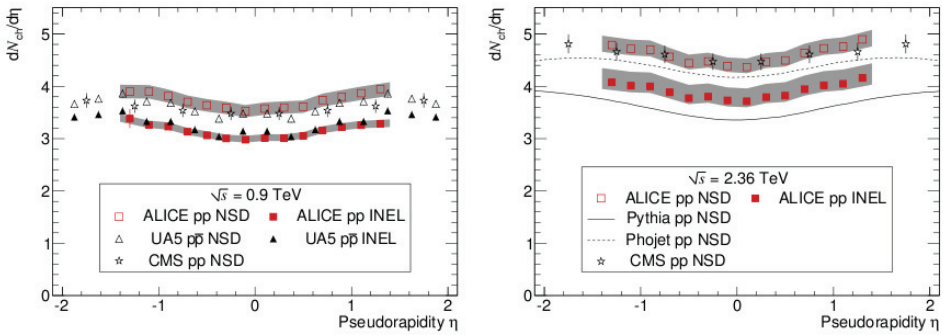

Figure 2.5: Left panel: pseudorapidity density distributions for inelastic (INEL) and Non-Single Diffractive (NSD) interactions at ALICE proton-proton collisions at $\sqrt{s} = 0.9\ TeV$, compared to UA5 and CMS data. Right panel: same for $\sqrt{s} = 2.36\ TeV$ data, compared to CMS results and predictions from PYTHIA and PHOJET. Figure taken from [42]

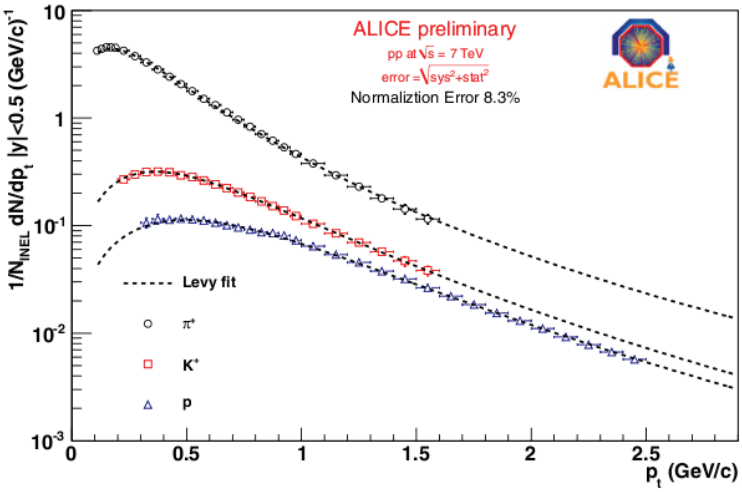

Figure 2.6: Combined p_T-spectra for positively charged particles in ALICE proton-proton collisions at $\sqrt{s} = 7\ TeV$. Lines are the fits of the Lévy function. Besides total uncertainties, there is additional 8.3% uncertainty due to the normalisation. Figure taken from [43]

therein). The main problems in extracting flow are finding the event plane, event-by-event fluctuations and identifying non-flow contributions. Methods for removing non-flow contributions exist, but require high multiplicities which are only found in heavy-ion collisions.

Momentum correlations

A distinguishing feature of heavy-ion collisions compared to simpler systems is the collective behaviour of matter. Particle correlations can be used as an indication of collective behaviour in the system. These correlations are dependent on the interactions in the medium, and the resulting particle production. The short range interferometric correlations known as femtoscopic correlations are the main topic of this thesis and will be discussed in detail in chapter 3.

Long-range correlations

The application of LUND type string models have successfully described the soft and semi hard parts of high energy pp collisions. These models characterise particle production as the breaking of colour strings. A more detailed description of string models will be given in chapter 4. In the case of heavy-ion collisions the growing number of strings causes increased interaction between the strings in form of string percolation [44]. Colour exchange between the endpoints of the strings causes long-range correlations between particles due to energy-momentum conservation.

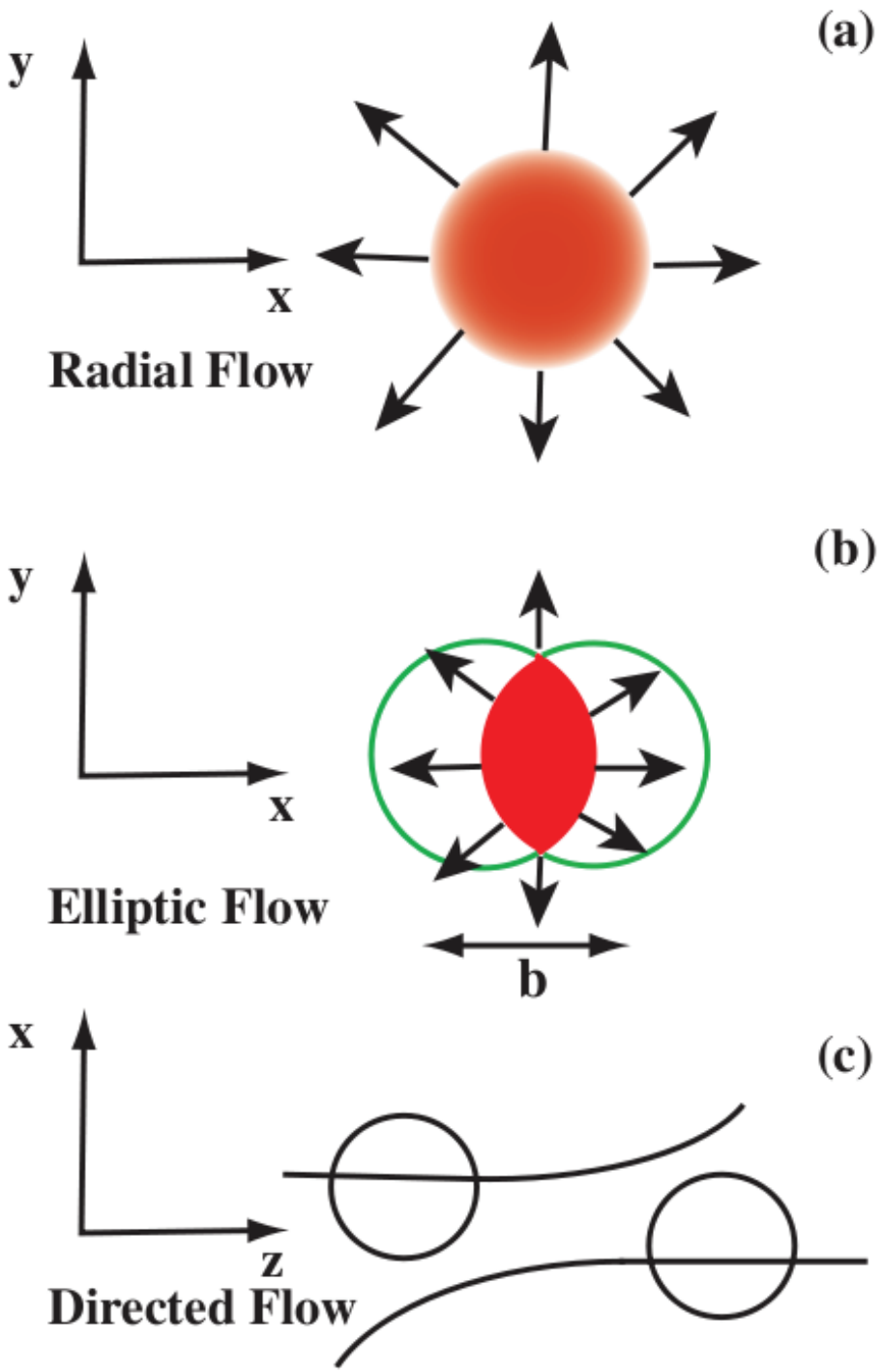

Figure 2.7: Illustration of the three most common flow phenomena. Figure taken from [46].
(a) Radial flow v_0, outward expansion from pressure gradients.
(b) Elliptic flow v_2, asymmetry in coordinate space creates an asymmetry in momentum space.

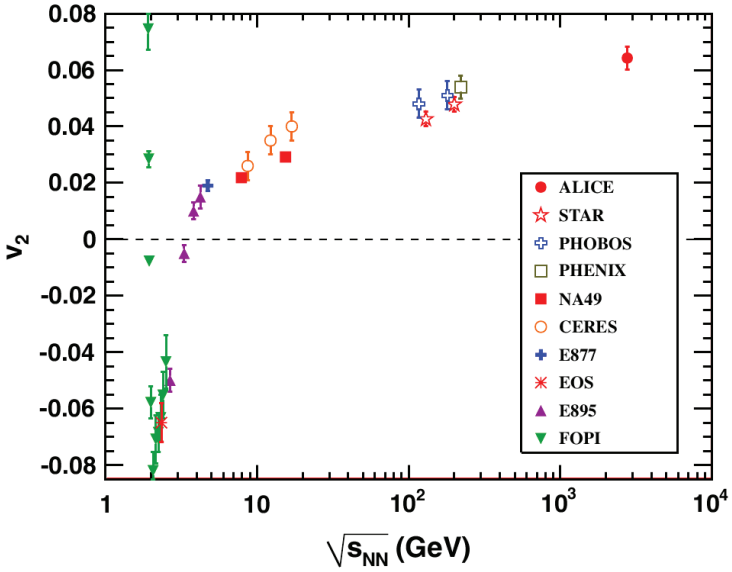

Figure 2.8: Elliptic flow measured as a function of collision energy. Figure taken from [47].

Long-range correlation studies are made with observables from two different and separated rapidity intervals, which are referred to as forward (F) and backward (B) rapidity windows. Correlations are calculated between two observables, the multiplicity of charged particles (n) and the mean transverse momenta (p_t). This gives us three types of long-range correlations between the two rapidity windows: $n - n$, $p_t - p_t$ and $p_t - n$. The correlations between forward and backward parameters are found to be close to a linear function:

$$\langle n_B \rangle = a + \beta_{nn} n_F \tag{2.2}$$

where n_F and n_B are the charged multiplicities in the forward and backwards regions and β_{nn} characterises the strength of the correlations.

Fluctuations

Physical quantities measured in an experiment will always be subject to fluctuations [49]. These fluctuations will depend on the properties of the system, and by studying them one can reveal information about the system. One of the ways to access this information is to study event-by-event fluctuations of a given observable. This will reveal the statistical and thermodynamical properties of the system.

The shape of fluctuations demonstrates whether or not the system is in thermal equilibrium, meaning the system can be described by statistical Gaussian fluctuations. Different methods are developed to analyse quantitatively the non-Gaussian shape of the fluctuations [45, 46].

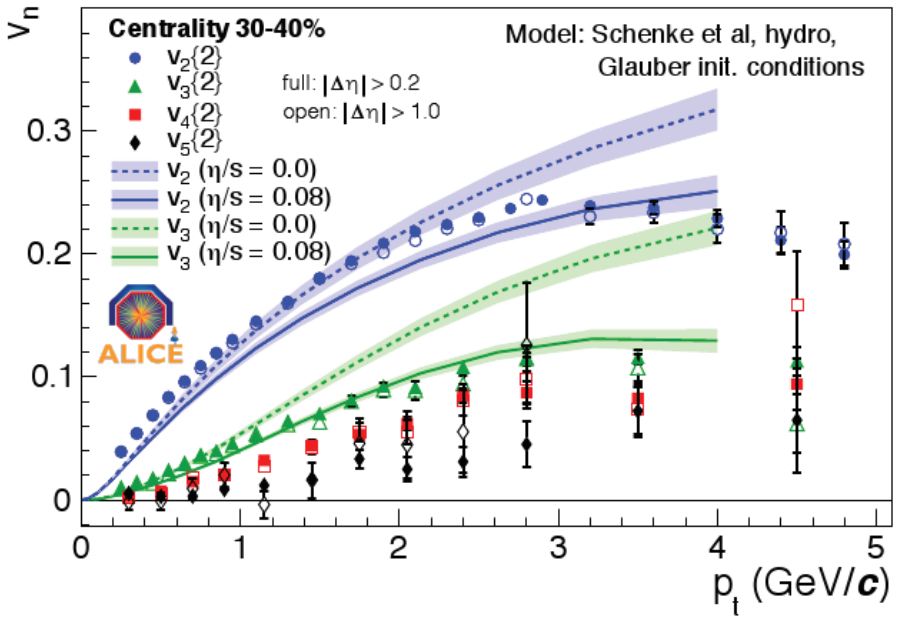

Figure 2.9: Higher order harmonics of the flow measured in the ALICE experiment. Figure taken from [48].

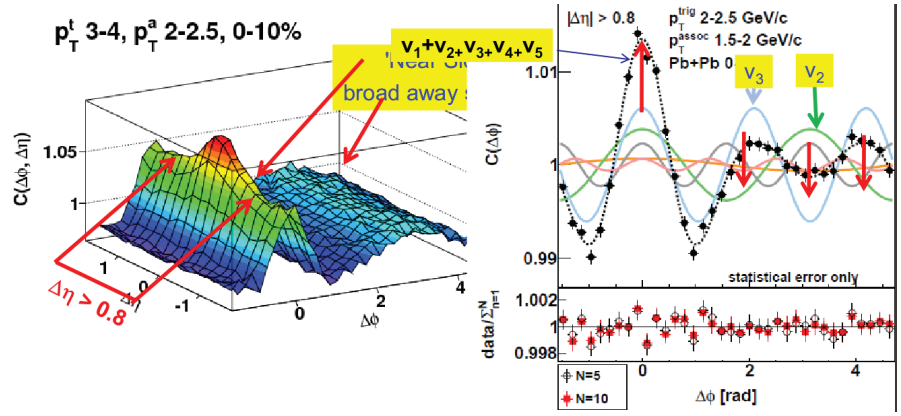

Figure 2.10: Higher order moments of the flow extracted from $d\eta/d\phi$ correlations in ALICE $\sqrt{s} = 2.76\,TeV$ heavy-ion collisions. Figure taken from [55].

From the point of view of statistical physics the fluctuations measure the susceptibilities of the system, meaning the response of the system to external forces.

Event-by-event fluctuation analysis can be applied to a number of different observables. They include: thermodynamic fluctuations, Bose-Einstein correlations, temperature fluctuations, multiplicity fluctuations, particle ratio and strangeness, conserved quantities, azimuthal anisotropy, transverse momentum and long range correlations.

Jets

In a hadron-hadron collision a high-p_T parton may be emitted from the interacting matter and undergo a cascade of consecutive decays of less energetic partons [50, 51]. These partons are observed as a cluster of hadrons in the detector. In proton-proton collisions we will always observe two or more back-to-back jets due to the energy-momentum conservation in the system. In heavy-ion collisions one or more of the original partons may be dispersed in the bulk matter due to multiple interactions with the medium. We can then observe standalone jets whose back-to-back partners have been swallowed in the medium, this "jet-quenching" is though to be a signal that can be used to probe any possible formation of QGP. High-p_T capabilities are needed for jet identification and reconstruction.

How to identify jets is not always clear, and depends on your definition and jet finder algorithm. A jet can be defined as a group of particles in a cone of fixed radius in the plane defined by the azimuth ϕ and pseudorapidity η. In heavy-ion collisions the large background must be taken into account. In order to reduce the contribution from uncorrelated particles a p_t cut is implemented. Typically $p_t^{cut} = 2\ GeV/c$ is used, this rejects 98% of the background.

Direct photons and dileptons

The production of photons in heavy-ion collisions is especially interesting [52]. Due to the fact that photons only interact weakly, they can pass through the hot and dense matter produced in the collision, and carry with them information about the collision at the time the photons where produced. The direct photons can be divided into four groups: The 'prompt' photons are produced early in the collision, during the initial nucleus-nucleus interactions. These photons carry information about the initial conditions of the collision. The second group consists of photons produced during the QGP phase. These photons will escape the plasma, and carry information about the pre-equilibrated QGP. The third group consists of photons produced by interactions during the hadronic phase of the expansion. Finally the last group consists of photons produced after freeze-out by resonance decays.

Direct photon can be distinguished into two p_t domains. High p_t photons ($p_t > 10\ GeV/c$) are prompt photons produced in hard scattering processes in the early plasma. They can be studied through photon-hadron or photon-photon correlations, or through photon tagged jets. Low p_t photons ($p_t < 10\ GeV/c$) include thermal photons in addition to prompt photons. The main problem in this domain is disentangling the various contributions.

Dileptons are produced in heavy-ion collisions throughout the entire evolution of the system in the same way as photons, and can be divided in to the same four groups as photons. They can

be used as a tool for measuring the temperature and dynamical properties of the system. Dilepton production is dominated by quark decays, but dileptons can also be produced from other sources such as mesons or Z^0.

Heavy quarks

One of the most famous predicted signatures of Quark Gluon Plasma is the suppression of J/ψ [53, 54]. The J/ψ particle consists of a $c\bar{c}$ pair, and are mostly produced during the initial moments of the collision from hard parton scattering. Due to the J/ψ-particle's need to pass through the hot and dense medium the charm-quarks will dissociate and combine with u, d or s quarks forming open charm mesons. The suppression of J/ψ is measured through the nuclear modification factor R_{AA} (Eq. 1.1), which is obtained by comparing heavy-ion data with scaled proton-proton data.

The experimental measurement of the J/ψ suppression at RHIC showed that current models that had described the suppression at the SPS were unable to predict the new results. In Fig. 2.11 the R_{AA} calculated from J/Ψ suppression is shown for both the ALICE and PHENIX RHIC experiments.

2.1.3 Detectors

The ALICE experiment is a highly complex system with a large number of subdetectors and subsystems [45, 46].

- Inner Tracking System (ITS)
  - Silicon Pixel Detector (SPD)
  - Silicon Drift Detector (SDD)
  - Silicon Strip Detector (SSD)
- Time-Projection Chamber (TPC)
- Transition-Radiation Detector (TRD)
- Time-Of-Flight (TOF)
- High-Momentum Particle Identification Detector (HMPID)
- PHOton Spectrometer (PHOS)
- Forward muon spectrometer
- Zero-Degree Calorimeter (ZDC)
- Photon Multiplicity Detector (PMD)
- Forward Multiplicity Detector (FMD)

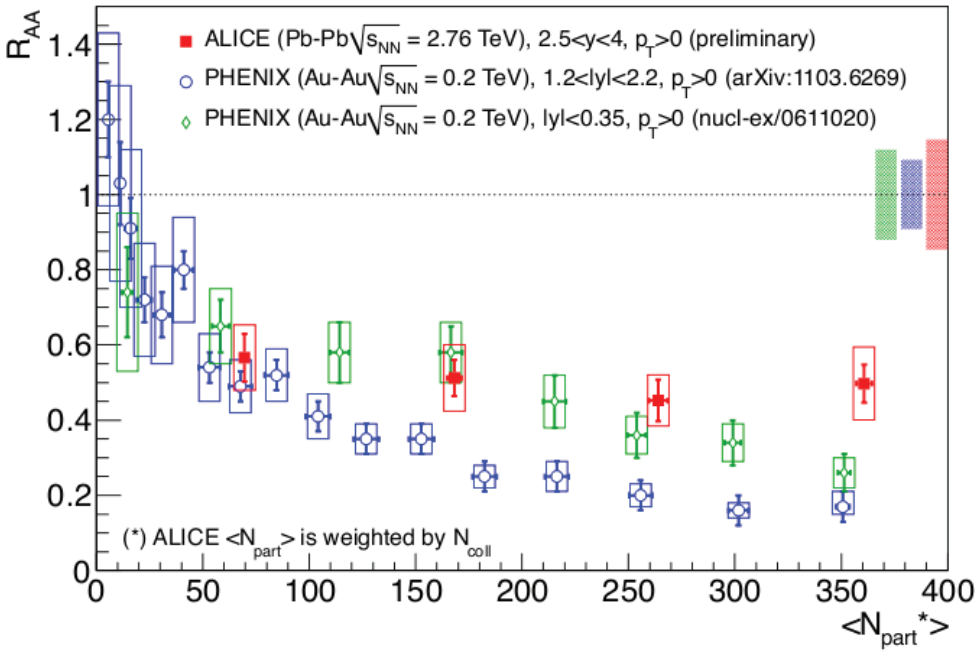

Figure 2.11: The J/Ψ R_{AA} calculated for both the ALICE and PHENIX experiments. Figure taken from [56]

- V0 detector
- T0 detector
- Cosmic-Ray trigger detector
- Trigger system
- Data AcQuisition system (DAQ)
- High Level Trigger (HLT)

These detectors give a wealth of information about the collisions which can be combined to give complete picture about the evolution of the system. Tracking is performed by the Inner Tracking System which consist of six layers of silicon detectors and the Time-Projection Chamber. Particle identification can be performed by measuring the energy loss in the tracking detectors, transition radiation in the TRD, velocity versus momentum in the Time-Of-Flight detector, Cherenkov radiation from the High-Momentum Particle Identification Detector and photons with the PHOton Spectrometer.

In this work we will focus on the identification of pions and kaons using the Inner Tracking System, Time-Projection Chamber and the Time-Of-Flight detectors.

Inner Tracking System

The Inner Tracking System (ITS) is composed of 6 layers of silicon detectors. The two innermost detectors are Silicon Pixel Detectors (SPD) with a inner radius of $3.9\ cm$ and a outer radius of $7.6\ cm$ from the beam axis. The second layer are the Silicon Drift Detectors (SDD) with a radius from $15\ cm$ to $23.9\ cm$. The outer detectors are the Silicon Strip Detectors (SSD) with a radius from $38\ cm$ to $43\ cm$. The covered range of the SPD is $|\eta| < 2$ and for the SDD and SSD it's $|\eta| < 0.97$.

The ITS detector localises the primary vertex with a resolution of $\sim 100 \mu ms$. Together with the TPC it is the main tracking detector. Using the ITS improves the overall tracking resolution. Energy losses in ITS are used for combined particle identification and provides a decrease in contamination from electrons in the kaon spectra. The SPD signal is also used for the minimal bias trigger, allowing the rejection of non-interaction events.

Time Projection Chamber

The Time Projection Chamber is the main tracking detector in the ALICE central barrel. The TPC is cylindrical in shape with an inner radius of about $85\ cm$ and an outer radius of about $250\ cm$. The overall length in the beam direction is $510\ cm$ for a total volume of $88\ m^3$. This field cage is filled with a Ne/CO_2 gas with a $90\%/10\%$ ratio. This mixture is a "cold" gas which must be kept at a steady temperature with $\Delta T < 0.1K$. A strong uniform electric field it set up along the beam direction in the field cage.

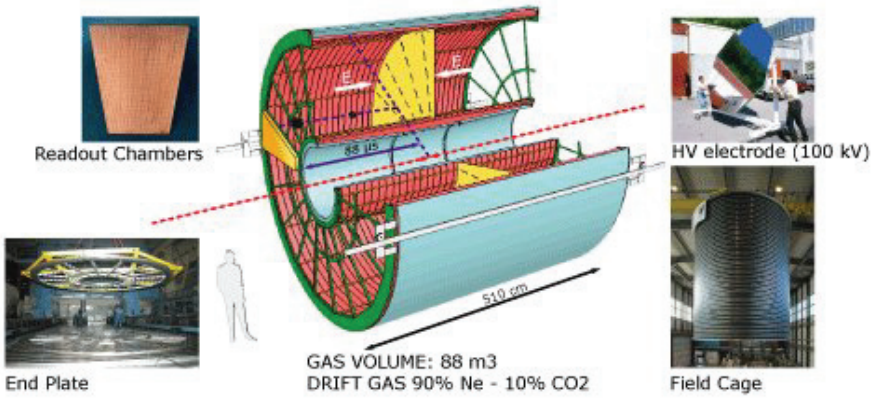

Figure 2.12: A schematic overview of the TPC. Figure taken from [25]

.

As charged particles enters the TPC they will ionise the gas along their path. Liberated electron will drift along the electric field and hit the readout chambers at the two end-caps of the TPC cylinder. Charges at the readout chambers will be amplified, digitised and sent to a specifically made chip known as the ALTRO (ALice Tpc ReadOut).

The TPC covers a phase space of pseudo-rapidity ranges $|\eta| < 0.9$ in p_t up to $100\ GeV/c$. It was designed for an assumed charged particle multiplicity of up to $dN_{ch}/d\eta = 8000$. The drift time in the field cage is about $88\mu s$. This means that the TPC is the slowest detector in ALICE, and is a detector optimised for heavy-ion collisions. In proton-proton collisions the main limitation is memory time due to the long drift time. The TPC is shown in Fig. 2.12.

Time Of Flight

The Time Of Flight detector is a specialised particle identification detector. It has a cylindrical shape with an internal radius of $370\ cm$ and an external radius of $399\ cm$. The detector covers polar angles between $45°$ and $135°$ over the full azimuth. The base unit of the TOF system is the Multigap Resistive Plate Chamber (MRPC). A single MRPC strip is $1220\ mm$ long and $130\ mm$ wide with an active area of $1200 \times 74\ mm^2$ subdivided into pads of $35 \times 25\ mm^2$.

The MRPC is a stack of resistive glass plates, with a high voltage applied to the external surfaces of the stack. Between the glass plates are gaps filled with the detector gas $C_2H_2F_4/i - C_4F_{10}/SF_6$, with a ratio $90\%/5\%/5\%$. As a particle passes through the stack it ionises the gas, and the liberated electron is amplified by the high electric field through an electron avalanche.

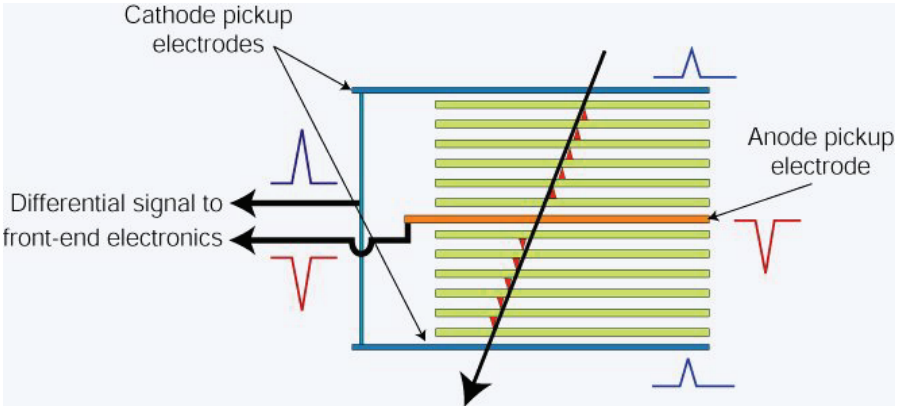

Figure 2.13: A schematic overview of a MRPC stack. Figure taken from [25].

The total signal is then the sum of the signal from all gaps. The efficiency of the signal depends on the number of gaps, and the time jitter of the signal depends on the individual gap widths. The MRPC stack is illustrated in Fig. 2.13

The TOF is designed for the general ALICE acceptance of $|\eta| < 0.9$ for particle identification in the intermediate momentum range (from 0.5 to 2.5 GeV/c). It allows to measure the flight time of the particle through the detector which along with the track gives the particle velocity β. The detector provides a time resolution of about 40 ps, but due to uncertainties of the start time of interaction (T0) the time of flight resolution is ~ 100 ps. A schematic view of the TOF detector is shown in Fig. 2.14.

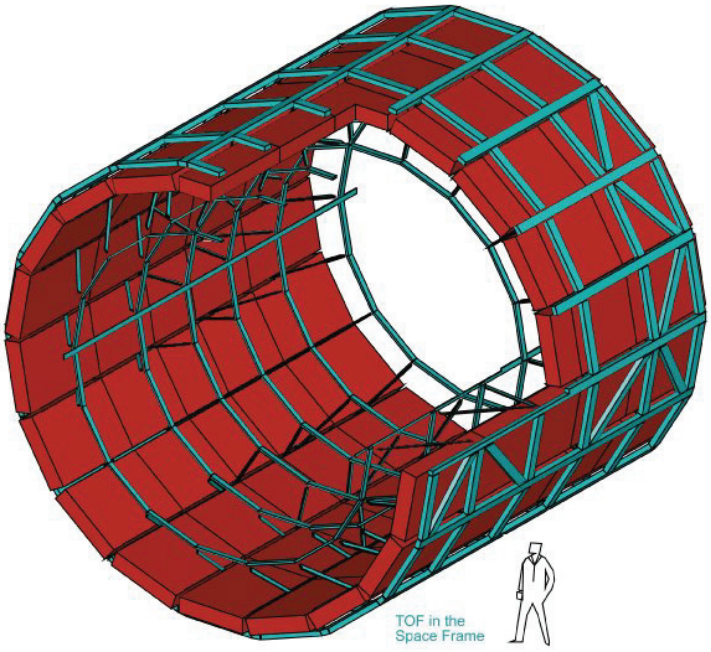

Figure 2.14: A schematic overview of the TOF. Figure taken from [25]
.

Chapter 3

Femtoscopy

Interactions between subatomic particles happen at such a small scale that it is impossible to observe with the naked eye. Consequently many methods have been developed to observe such interactions through the macroscopic effects they have. Such observations have formed the basis of modern nuclear physics, from Rutherford's gold foil experiment to contemporary particle colliders.

Detection of produced particles in the ALICE experiment is done through the electrical interactions the particles have with the detector materials. If we want to study the size of the emitting source we must go even one level deeper, by studying the effects the source had on the emitted particle spectra. One method to do this is by looking at momentum correlations between the particles. Currently such methods are referred to as femtoscopic, as they allow to study sizes at femtometer level, but historically they have been called HBT after a similar method used earlier in astrophysics.

R. Hanbury-Brown and R. Q. Twiss first suggested the measurement of the angular size of a star through the use of correlations in their 1954 paper [57]. They proposed a method to measure the angular size of a star by studying correlations of the intensity of incoming electromagnetic waves in two photomultiplier tubes as a function of the distance between the tubes. This is known as intensity interferometry or sometimes HBT correlations. The idea that photons could be correlated was thought to be controversial and Hanbury-Brown and Twiss themselves conducted an experiment to test the validity [58]. Both Hanbury-Brown and Twiss were radio engineers and explained their findings in classical terms, but it is also possible to explain them with quantum mechanics.

The first test of this technique was made in [59], where they attempted to measure the angular size of Sirius. The experimental set up consisted of two mirrors which focused the light, guided on to the star with an optical sight. The signals from the two mirrors were then amplified and mixed to give a correlated signal. The correlations were measured as a function of the distance between the mirrors, and the angular size of Sirius was calculated to be 0.0063" with an estimated error of 10%. A modern HBT measurement at Sydney Observatory ([60]) gives the angular size as 0.00604", which is tantalisingly close to the original Hanbury-Brown and Twiss measurement.

Momentum correlations between particles in nuclear physics were first studied by Goldhaber, Goldhaber, Lee and Pais [61]. They observed pions emitted from $p\bar{p}$-annihilations in a bubble

chamber, and found that the angular distributions were narrower for same charge than for opposite charge pairs. This was in stark contrast to the statistical model where no such distinctions were made. The authors explained this through the influence of Bose-Einstein correlations for identical pions. They also introduced the Gaussian correlation function dependent on the radius of the interaction volume

It is possible to use momentum correlations between emitted particles to extract information about the space-time extent of the emitting source. In both the astrophysics and particle physics case one can obtain information about one part of the phase space by studying correlations in another part of the phase-space. The main difference is that for astronomy the correlations happen in the detector, while for particle physics the correlations happen in the emitting source.

The correlation function is defined as:

$$CF(p_1, p_2) = \frac{P_2(p_1, p_2)}{P_1(p_1)P_1(p_2)} \tag{3.1}$$

where p_1 and p_2 are the momenta of the two particles, P_2 is the two-particle momentum distribution and P_1 is the one-particle momentum distribution. If the correlation function is equal to unity we have $P_2(p_1, p_2) = P_1(p_1)P_1(p_2)$ and the two particles are emitted independently. For a correlation function not equal to unity the two-particle momentum distribution will not be factorised and the emitted particles are correlated in momentum.

Here the particles 1 and 2 can be bosons or fermions, identical or non-identical and the correlation effects will have different origin in each case. In this text we will take a closer look at identical and non-identical meson particle pairs.

3.1 Identical particle correlations

We can consider two identical particles with momentum p_1 and p_2 that are emitted from two different regions A and B of the source, with radius R_A and R_B, and are detected in the detector. Since the particles are identical we can not distinguish between the cases where the particle with momentum p_1 is emitted from A and the particle with momentum p_2 from B or where the particle with momentum p_1 is emitted from B and the particle with momentum p_2 from A. An illustration of this is seen in Fig. 3.1.

The wave-function of the pair must then take into account both possibilities. The wave function of a single free particle with momentum p and position x is:

$$\psi(p, x) = \exp(-ipx) \tag{3.2}$$

The symmetrised two-particle wave-function is then:

$$\Psi(q, r) = \frac{1}{\sqrt{2}} \left[\exp(-ip_1x_A - ip_2x_B) + \exp(-ip_2x_A - ip_1x_B)\right] \tag{3.3}$$

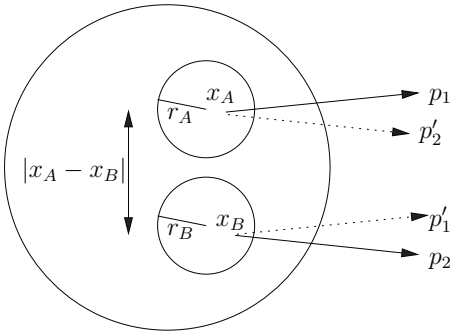

Figure 3.1: Identical particle emission from two regions in a source. Particle 1 is either emitted from region A as depicted with momentum p_1 or from region B as depicted with momentum p_1'. Particle 2 is then emitted from the other region.

The correlation function is constructed from the single particle and two particle inclusive spectra:

$$\begin{aligned} P_1(p_i) &= E_i \frac{dN_i}{d^3p_i} \\ P_2(p_1, p_2) &= E_1 E_2 \frac{dN_{12}}{d^3p_1 d^3p_2} \end{aligned} \tag{3.4}$$

giving:

$$CF(p_1, p_2) = \frac{dN_{12}/(d^3p_1 d^3p_2)}{(dN_1/d^3p_1)(dN_2/d^3p_2)} \tag{3.5}$$

Here N_i is the multiplicity and E_i is the energy of particle i with momentum p_i. N_{12} is the total multiplicity of particle 1 and 2. It is possible to describe the emission of particles using the source emission function $S(x, p)$:

$$\begin{aligned} E_i \frac{dN_i}{d^3p_i} &= \int d^4x_i S_1(x_i, p_i) \\ E_1 E_2 \frac{dN_{12}}{d^3p_1 d^3p_2} &= \int d^4x_1 d^4x_2 S_1(x_1, p_1) S_1(x_2, p_2) \left|\Psi(q^*, r^*)\right|^2 \end{aligned} \tag{3.6}$$

The source function is understood as a generalised density function of the source, or as a probability density function. A necessary assumption here is independent particle emission from the source, i.e. the two-particle emission function can be factorised. This gives the correlation function [65]:

$$CF(p_1, p_2) = \frac{\int d^4x_1 d^4x_2 S_1(x_1, p_1) S_1(x_2, p_2) \left|\Psi(q^*, r^*)\right|^2}{\int d^4x_1 S_1(x_1, p_1) \int d^4x_2 S_1(x_2, p_2)} \tag{3.7}$$

The correlation function can also be defined by the Koonin-Pratt equation [62, 63]:

$$C(q, K) = \int S_2(r^*, K) |\Psi(q^*, r^*)|^2 d^4r^* \tag{3.8}$$

where S_2 is the two-particle emission source function:

$$S_2(r^*, K) = \frac{\int d^4x_1 d^4x_2 S_1(x_1, p_1^*) S_1(x_2, p_2^*) \delta(r^* - x_1^* + x_2^*)}{\int d^4x_1 d^4x_2 S_1(x_1, p_1^*) S_1(x_2, p_2^*)} \tag{3.9}$$

Here $r^* = x_A^* - x_B^*$ is the space-time separation of the pair, $q^* = p_1^* - p_2^*$ is the pair momentum difference and $K = p_1 + p_2$ is the total pair momentum, respectively. We see that the correlation function can be described as an integral of the source function with the two-particle correlation function over the space-time separation of the pair.

The general idea of femtoscopic analysis is to probe the source function through the correlation function. As seen in Eq.(3.8) we can consider the two-particle wave function Ψ as a kernel that transforms from coordinate-space basis to the relative momentum basis. So if the particle momenta are correlated with their emission points (space-momentum correlations), the correlation radii R_i will depend on the total momentum of the pair.

In heavy-ion collisions, space-momentum correlations arise due to the collective expansion of the source. Pions that are produced from resonance decays will usually originate from a larger space-time region and have low momentum. These particles may also exhibit space-momentum correlations, therefore the correlation radii measures the size of the regions emitting particles of a given momenta. This is important to stress, the correlation function does not describe the size of the whole source, only the so-called "region of homogeneity" [64]. The homogeneity length is the size of the region that contributes to the pion spectrum at a particular three-momentum p.

The term $|\Psi|^2$ is used as a weight in the numerator of the wave-function. If we assume the two-particle wave-function is described only by the quantum statistical effect (e.g. no Coulomb forces) we get:

$$\begin{aligned} |\Psi(q,r)|^2 &= \frac{1}{2} |\exp(-ip_1x_A - ip_2x_b) + \exp(-ip_2x_A - ip_1x_B)|^2 \\ &= \frac{1}{2} \left(\exp(i(p_1 - p_2)(x_A - x_B)) + \exp(-i(p_1 - p_2)(x_A - x_B)) + 2\right) \\ &= 1 + \cos(qr) \end{aligned} \tag{3.10}$$

where $q = p_1 - p_2$ is the relative pair momenta and $r = x_A - x_B$ is the pair separation.

From this result we can see that the Bose-Einstein correlation effect has the form of a cosine. This means that the correlations will be maximum if the particles have either almost the same momentum or are emitted from almost the same space-time point. The correlation effect arises when the wave-functions of particles with small relative momenta overlap and start to interfere.

There are several assumptions that have been made to get the above results [65]. The first assumption is that we have neglected higher order symmetrisation in the system. If there are more than two identical particles in the system higher order symmetrisation will affect the spectra. This is only important when the phase space density approaches unity.

The second assumption is the already mentioned requirement that the emission process is initially uncorrelated. This allows us to write the two-particle emission probability as a function of one particle source functions.

The third assumption is the so called smoothness approximation. This means that the regions of coherent emission must be small compared to the size of the system $r_A, r_B << |x_A - x_B|$. The momentum dependence of the source emission function must be sufficiently smooth:

$$S(x_1, p_1)S(x_2, p_2) = S(x_1, K - \frac{1}{2}q)S(x_2, K + \frac{1}{2}q) \approx S(x_1, K)S(x_2, K) \tag{3.11}$$

The final assumption is the equal time approximation. For systems with Coulomb or strong interactions we must neglect non-zero time component of the evolution matrix, in order to identify it with the pair rest frame.

3.1.1 Parametrisation of the correlation function

From Eq.(3.8) and Eq.(3.10) we see that the shape of the source will manifest itself in the shape of the correlation function. We assume that the source can be described as a static 3-dimensional Gaussian:

$$S(r) = N \exp\left(-\frac{r_x^2}{4R_x^2} - \frac{r_y^2}{4R_y^2} - \frac{r_y^2}{4R_y^2}\right) \tag{3.12}$$

This means the correlation function will also be a Gaussian. With a Cartesian parametrisation we get:

$$CF(q) = 1 + \lambda \exp(-R_x^2 q_x^2 - R_y^2 q_y^2 - R_z^2 q_z^2) \tag{3.13}$$

Here $q = p_1 - p_2$ is the difference in pion momenta that allows us to look at the correlations as a function of a single momentum parameter, and the λ parameter determines the strength of the correlations. R_i is the spatial size of the source for directions $i = x, y, z$.

The correlation function in Eq.(3.13) is integrated over the total pair momentum K. Usually the dependence on K is checked by dividing the correlation function in bins of the transverse pair momentum $K_T = |p_{T,1} + p_{T,2}|/2$. We then assume that each separate K_T bin is approximated by a static source.

For convenience we introduce the so called *"out-side-long"* coordinate system. The *out*-axis is along the pair-direction for each separate pair. The *long*-axis is along the beam direction and the *side*-axis is perpendicular to both *out* and *long*. Fig. 3.2 shows a representation of the decomposition.

Notice that this coordinate system is not global, it is individual for each pair. We can decompose the three-momentum vector $\mathbf{q}$ into the *"out-side-long"* directions to get the correlation function in the form:

$$CF(q) = 1 + \lambda \exp(-R_{out}^2 q_{out}^2 - R_{side}^2 q_{side}^2 - R_{long}^2 q_{long}^2) \tag{3.14}$$

This can be simplified by looking at the invariant correlation function. We look at the correlations as a function of $q_{inv} = |\vec{q}|$. The correlation function then becomes:

$$CF(q_{inv}) = 1 + \lambda \exp(-R_{inv}^2 q_{inv}^2) \tag{3.15}$$

Both the one-dimensional and the three-dimensional forms of the correlation function is employed for the analysis of experimental data.

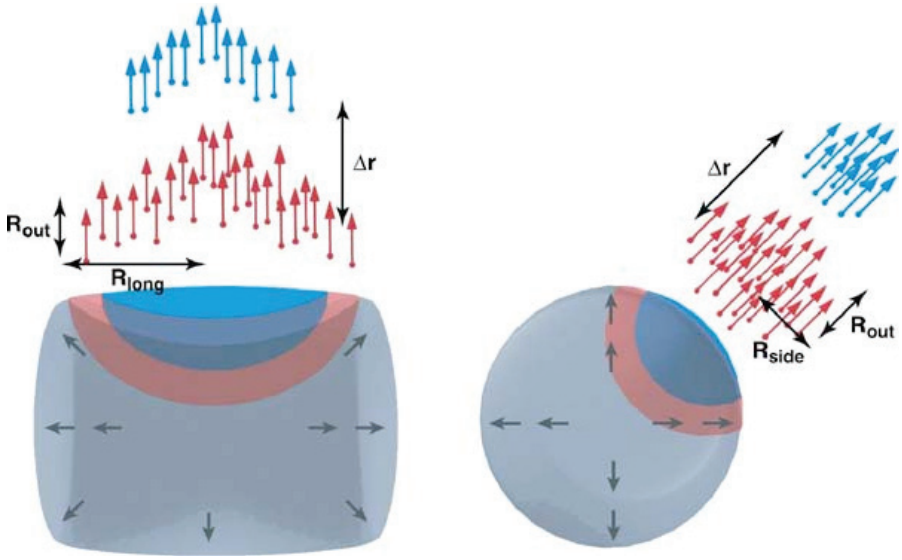

Figure 3.2: A representation of the out-side-long direction compared to the source. Figure taken from [65]

3.1.2 Azimuthally dependent correlations

In Eq.(3.14) azimuthal symmetry has been assumed. If we disregard this assumption the correlation function can be written as:

$$CF(q) = 1 + \lambda \exp\left(\sum_{ij} -q_i q_j R_{ij}^2\right) \tag{3.16}$$

Here $i, j = o, s, l$ corresponding to "out", "side" and "long" directions respectively. $R_{oo} = R_{out}$, $R_{ss} = R_{side}$ and $R_{ll} = R_{long}$ are the old radii. R_{os},R_{ol} and R_{sl} are the off diagonal components that carry information about the anisotropy of the collision. If we assume azimuthal symmetry the off diagonal components vanish.

It is possible however to create a correlation function dependent on the azimuthal angle ϕ. We can calculate the Fourier components $R_{s,n}^2 = \langle R_s^2(\phi)\cos(n\phi)\rangle$ and use them to estimate the eccentricity of the source [66, 67, 68]:

$$\epsilon = 2\frac{R_{s,2}^2}{R_{s,0}^2} \tag{3.17}$$

Azimuthally dependent HBT has been studied at STAR [69] and is underway in ALICE [70]. It will not be studied in more detail in this work.

3.1.3 Spherical harmonics correlation function

It is also possible to use another parametrisation of the correlation function. The main advantage of this spherical harmonics approach is that the full 3D information is encoded in several 1-dimensional histograms [71, 72, 73]. The moments of the spherical harmonics decomposition are given by:

$$C_l^m(q_{inv}) \equiv \frac{1}{\sqrt{4\pi}} \int d\phi d(\cos\theta) C(q_{inv}, \theta, \phi) Y_l^m(\theta, \phi) \tag{3.18}$$

Here the correlations are given as a function of the Euler angles, which can be connected to the "out-side-long" space by the relations $q_{long} = q_{inv} \cos\theta$ and $q_{out} = q_{inv} \sin\theta \cos\phi$. Y_l^m represent the spherical harmonics. For identical particles from collisions with symmetrical beams odd l and odd m for even l component vanish. The first three non-vanishing moments are C_0^0, C_2^0 and C_2^2. They capture essentially all of the 3-dimensional structures. The C_0^0 moment is the angle-averaged component and corresponds to the $CF(q_{inv})$ correlation function. The C_2^0 component is weighted with $\cos^2\theta$, if it is non-zero it means the longitudinal and transverse sizes are different. The C_2^2 component is weighted with $\cos^2\phi$ and measures the difference between the "out" and "side" directions.

The use of spherical harmonics offers certain advantages compared to using Cartesian coordinates. In addition to capturing all the 3-dimensional information in several 1-dimensional histograms, spherical harmonics also avoid problems of coverage due to the kinematics of the pair. While the spherical harmonics approach has certain advantages it will not be employed in the main subject of this thesis, and we will not go into further details. In this thesis we have used the Cartesian representation of the correlation function in order to make one to one comparisons with experimental results and due to the complicated background treatment required of the πK correlation function in pp collisions.

3.1.4 Extracting the correlation function from experiment

In experiment the correlation function can be defined as $CF(q) = \dfrac{N(q)}{D(q)}$. The numerator represents the two-particle momentum distribution $N(q) = P_2(q)$ and is measured directly. The denominator is equal to the product of two one-particle momentum distributions and is obtained by the so called mixing procedure. Particles from different events are used to form pairs which are used to create an uncorrelated two-particle momentum distribution, we use this distribution as our denominator $D(q)$. Unfortunately this method introduces non-femtoscopic correlations at high q originating from the lack of energy-momentum conservation in the mixed events. These correlations must be taken into account in the fitting procedure.

Particles in experiment will also interact through the Coulomb and strong nuclear forces. These interactions will introduce correlations which also have to be taken into account in the fitting. For charged identical bosons the Coulomb interaction dominates and fitting can be done with the following formula [65]:

$$CF(q) = (1-\lambda) + \lambda K(q_{inv}) \left(1 + \exp\left(-R_{out}^2 q_{out}^2 - R_{side}^2 q_{side}^2 - R_{long}^2 q_{long}^2\right)\right) \tag{3.19}$$

Here $K(q_{inv})$ is a function taking into account the Coulomb effect.

In proton-proton collisions or in peripheral heavy-ion collisions the produced multiplicity is small and conservation laws can lead to a specific rise of the tail of CFs at large q_{inv}. To take into account this effect or any other non-femtoscopic correlations the "baseline function" $B(q_{inv})$ can be introduced in 1D or 3D equations. Particularly in the case of proton-proton collisions the following shape of the CF can be used:

$$CF(q_{inv}) = \left[(1-\lambda) + \lambda K(q_{inv})(1+\exp(-R_{inv}^2 q_{inv}^2))\right] B(q_{inv}) \tag{3.20}$$

The function $B(q_{inv})$ describes the non-femtoscopic background and must be obtained from either experiment or a model. The baseline function will typically be obtained from a fit to a correlation function from a model simulation without any quantum statistical effect. The model CF will then describe only the non-femtoscopic effects of the system. After the baseline function $B(q_{inv})$ is found through a fit the fitting parameters are fixed and kept as constants during the fit of the experimental data.

Because the choice of baseline function can have a strong impact on the final results it is important to chose a source for the baseline which is as reliable as possible. Unfortunately it is very difficult to extract the baseline directly from experiment, which is why a model is usually used. It is important to keep in mind, however, that the following results are good as long as the model is reliable.

3.1.5 Extracting the correlation function from microscopic models

In microscopic models we have the full momentum information of all particles. However the quantum-statistical effect which is the source of our correlations is not present in current models. In order to study correlations from a model we use the correlation function $CF(q) = \dfrac{N(q,\omega)}{N(q,1)}$. Here $N(q,\omega)$ is the two-particle momentum distribution taken from the model weighted by a factor ω. The weight $\omega = 1 + \cos(qr)$ is taken from Eq. 3.10 and introduces the correlations by accounting for the quantum statistical effect. $N(q,1)$ is the unweighted two-particle momentum distribution, meaning is it uncorrelated and can be used as the background. This we will call the "pure" correlation function.

It is also possible to simulate the experimental procedure by creating the denominator by using pairs made up of particles from different events. In this case the correlation function becomes $CF(q) = \dfrac{N(q,\omega)}{B(q)}$ where $B(q)$ is the two-particle momentum distribution of particles from different events. This will introduce non-femtoscopic correlation into the correlation function, since there is no energy-momentum conservation for pairs from different events. This will be called the "mixed" correlation function.

In most microscopic models there are no Coulomb or strong final state interactions. This means that if you want to take these effects into account it must be done in the weighting procedure, but for two-pion correlations we will consider only the pure Bose-Einstein effect. Eq. 3.20 can still be used for the fitting, but with $K(q_{inv}) = 1$. The function $B(q_{inv})$ can be put to one

for the "pure" correlation function or it can be taken in a form of a polynomial describing the background for the "mixed" correlation function.

Unlike for experiments it is possible for model data to calculate the mixed correlation function with $\omega = 1$, in which case the correlations present are all non-femtoscopic in origin. The baseline can be fit to these non-femtoscopic correlations and then used in the femtoscopic fit. The reason for doing this is to reproduce the experimental analysis method as closely as possible. While in experiment a model is used to create the baseline, for a model prediction one has complete information about the shape of the baseline.

3.2 Nonidentical particle correlations

Up to now we have only discussed correlations between identical particles. However it is also possible to consider correlations between non-identical particles. For identical particle pairs Final State Interactions (FSI) were considered as an effect that had to be corrected for. For non-identical particles on the other hand there is no quantum statistical effect, and Coulomb and strong FSI is the source of the correlations. The Coulomb effect dominates for charged pairs, which means that whether the pairs have the same or different charge sign is important. Particles will have negative correlations for pairs with same sign charges, and positive for pairs with opposite sign. Furthermore the strength of the correlation depends on the length of the interaction time of the two particles.

The main advantage of studying non-identical particle pairs, as opposed to identical pairs, is that it allows one to probe the asymmetry of space-time emission between the two particles in the pair. This can be achieved by using the so called "double-ratio" formalism.

3.2.1 Formalism

Symbols and conventions used in non-identical particle correlation analysis are introduced in this section and will be used consistently throughout this work.

The laboratory frame is the rest frame of the emitting source, known as the Centre of Mass System (CMS). In this reference frame particle i is described by its four-momentum p_i and space-time position x_i:

$$\begin{aligned} p_i &= (E_i, \vec{p}_i) \\ x_i &= (t_i, \vec{r}_i) \end{aligned} \tag{3.21}$$

Here r_i can be decomposed in x, y, z, where z is along the beam direction and x, y is along the transverse plane.

When looking at a pair we use the centre of mass rest frame of the pair, known as the Pair Rest Frame (PRF). All values in PRF are market with an asterisk $*$. Since we are looking at non-identical particles it is important to know which particle is the first in the pair. By convention we chose the particle with the smallest mass to be first, or if they have the same mass the particle with positive charge.

The space-time difference of the pair is described by $\vec{r}$ and Δt:

$$\begin{aligned} \vec{r} &= \vec{r}_1 - \vec{r}_2 \\ \Delta t &= t_1 - t_2 \end{aligned} \tag{3.22}$$

The four-momentum of the two particles in the pair can be used to create two quantities describing the momentum of the pair, namely the total pair momentum K and half the relative pair momentum k^*:

$$\begin{aligned} K &= p_1 + p_2 \\ k^* &= \frac{p_1 - p_2}{2} \end{aligned} \tag{3.23}$$

The reason k^* is marked with an asterisk is that it is also the momentum of the first particle in PRF:

$$k^* = p_1^* = -p_2^* \tag{3.24}$$

Again we introduce the "out-side-long" parametrisation. "Out" is along the pair-momentum K, "long" is along the beam direction z and "side" is perpendicular to both. We can decompose r^* and k^* into "out-side-long" directions. First the pair must be boosted into the Longitudinal Co-Moving System (LCMS):

$$\begin{aligned} k^*_{long} &= p^{LCMS}_{1,z} = -p^{LCMS}_{2,z} \\ r^*_{long} &= r_{1,z} - r_{2,z} \end{aligned} \tag{3.25}$$

We then boost the pair into PRF along the "out"-direction:

$$\begin{aligned} k^*_{out} &= p^*_{1,out} = -p^*_{2,out} \\ k^*_{side} &= p^*_{1,side} = -p^*_{2,side} \end{aligned} \tag{3.26}$$

$$\begin{aligned} r^*_{out} &= r^*_{1,out} - r^*_{2,out} \\ r^*_{out} &= r^*_{1,side} - r^*_{2,side} \end{aligned} \tag{3.27}$$

The relations between pair separation in CMS and PRF then become:

$$\begin{aligned} r^*_{out} &= \gamma_T(r_{out} - \beta_T \Delta t_{LCMS}) \\ r^*_{side} &= r_{side} \\ r^*_{long} &= \gamma_z(r_{long} - \beta_z \Delta t) \\ t^* &= \gamma_T(\Delta t_{LCMS} - \beta_T r_{out}) \\ \Delta t_{LCMS} &= \gamma_z(\Delta t - \beta_z r_{long}) \end{aligned} \tag{3.28}$$

where $\gamma_T = \sqrt{1-\beta_T^2}$, $\gamma_z = \sqrt{1-\beta_z^2}$ and $\beta_T = \frac{|p_T|}{\sqrt{E^2 - p_z^2}}$, $\beta_z = \frac{|p_z|}{E}$.

3.2.2 Asymmetry

We will study the asymmetry of a charged particle pair. Assuming that Coulomb forces dominate we get:

$$\begin{aligned} CF(k^*) &= A_c(\eta)\left[1 + 2\left\langle r^*(1+\cos\theta^*)\right\rangle\right] \\ A_c(\eta) &= 2\pi\eta\left[\exp(2\pi\eta) - 1\right]^{-1} \end{aligned} \tag{3.29}$$

Here $A_c(\eta)$ is the Coulomb (or Gamow) factor, $\eta = 1/(k^*a)$, $a = 1/(\mu z_1 z_2 e^2)$ is the Bohr radius. θ^* is the angle between the relative pair momentum k^* and the pair separation r^*. For same-sign pairs both the Coulomb factor and the correlation function is less than unity and the Bohr radius is positive. The term $1+\cos\theta^*$ is always positive. We then get maximum strength of correlations when $\cos\theta^* < 0$. This means for $90^\circ < \theta^* < 270^\circ$, the vectors k^* and r^* are anti-aligned. Conversely the correlations become weaker when k^* and r^* are aligned, $\cos\theta^* > 0$. If we look at opposite sign pairs the Coulomb factor and the correlation function are greater than unity and the Bohr radius is negative. We still get the strongest correlations for $\cos\theta^* < 0$.

This can be explained if one realises that k^* and r^* anti-alignment means that the particles in the pair are emitted moving towards each other, and will then have a longer interaction time than if k^* and r^* are aligned and the particles move away from each other.

The angle θ^* is not directly accessible for the experimental measurement. It is however possible to use the momentum of the two particles to calculate the total pair momentum K and the relative pair momentum k^*. The angle between K and k^* will be called Ψ. We can connect Ψ to θ^* through ϕ which is the angle between r^* and K:

$$\Psi = \theta^* + \phi \tag{3.30}$$

A representation of the momentum vectors and their angles can be found in Fig. 3.3.

We can divide our pairs into two groups. The first group has K and k^* aligned $(\cos\Psi > 0)$, the second group has K and k^* anti-aligned $(\cos\Psi < 0)$. Pairs from each group can be used to create two correlation functions: CF^+ corresponding to group one, and CF^- corresponding to group two. If these two correlation functions are different it would mean that one of the groups has $\langle\cos\theta^*\rangle < 0$ which means that the other group has $\langle\cos\theta^*\rangle > 0$. Thus we have a correlation between $\cos\Psi$ and $\cos\theta^*$. We obtain from Eq.(3.30):

$$\langle\cos\Psi\rangle = \langle\cos(\theta^* + \phi)\rangle = \langle\cos\theta^*\cos\phi - \sin\theta^*\sin\phi\rangle \tag{3.31}$$

We are interested in the signs of $\cos\Psi$, $\cos\theta^*$ and $\cos\phi$. If we have an angle α that is on average $-90 < \alpha < 90$ then we have $\langle\cos\alpha\rangle > 0$ and $\langle\sin\alpha\rangle = 0$. This corresponds to the angle between two vectors that are on average aligned. For two vectors that are on average anti-aligned we have $\langle\cos\alpha\rangle < 0$ and $\langle\sin\alpha\rangle = 0$. If we assume the signs of $\langle\cos\Psi\rangle$ and $\langle\cos\phi\rangle$ are correlated we get:

$$sign\,\langle\cos\Psi\rangle = sign\,\langle\cos\theta^*\rangle\; sign\,\langle\cos\phi\rangle \tag{3.32}$$

An easy way to see if there exists asymmetry in the system is to plot the "double-ratio": CF^+/CF^-. If the double-ratio is above unity it means we have $\langle\cos\theta^*\rangle < 0$ when $\langle\cos\Psi\rangle > 0$ and $\langle\cos\theta^*\rangle > 0$ when $\langle\cos\Psi\rangle < 0$. From Eq.(3.32) we can see that in both cases $\langle\cos\phi\rangle < 0$.

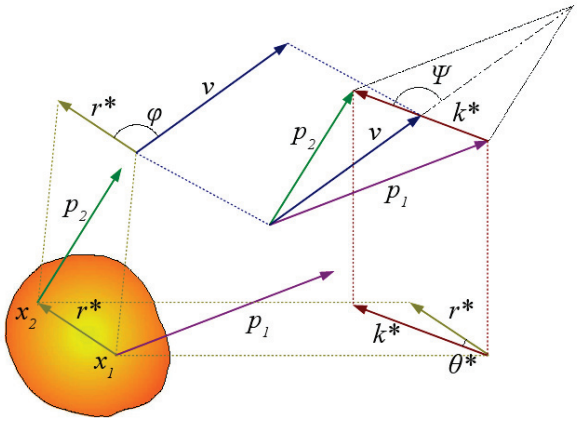

Figure 3.3: Momentum vectors of the pair, with the angles Ψ, θ^* and ϕ. Figure taken from [74]

This means that on average K and r^* are anti-aligned. If the double-ratio is below unity the opposite is true, we have $\langle \cos\phi \rangle > 0$ and K and r^* are on average aligned.

It is possible to extract even more information out of the double-ratio if we consider the case where $q \to 0$ [75]:

$$\frac{CF_i^+}{CF_i^-} \approx 1 + 2\left\langle r_i^* \right\rangle / a, \quad q \to 0 \tag{3.33}$$

Here i corresponds to the kinematical direction chosen when dividing into CF^+ and CF^-. So far we have considered dividing by the sign of $\cos\Psi$, which is equivalent to $k^*_{out} > 0$ for CF^+ and $k^*_{out} < 0$ for CF^-. It is possible however to chose either $i = out$, $i = side$ or $i = long$. This will give us information about the asymmetry in "out", "side" and "long" directions respectively. However since the pair-momentum K has no "side"-component by definition the side-axis for CF^+ and CF^- must be chosen arbitrarily, and by azimuthal asymmetry the side direction should have $CF^+_{side}/CF^-_{side} = 1$. This can be a useful experimental cross-check.

The "out"-direction double ratio is the most interesting because it allows us to probe the emission asymmetry along the pair-momentum. The existence of such an asymmetry tells us that one particle type is emitted on average either earlier or closer to the source in the fireball. By fitting the double ratio it is possible to extract quantitative information about this asymmetry, which gives us dynamical information about the system.

3.3 Femtoscopy results in the ALICE experiment

The ALICE collaboration have reported the results of femtoscopic analysis of meson and baryon pairs measured in $PbPb$ collisions at $\sqrt{s} = 2.76\ TeV$, and in pp collisions at $\sqrt{s} = 0.9\ TeV$, $\sqrt{s} = 2.76\ TeV$ and $\sqrt{s} = 7\ TeV$. The main features of the femtoscopic measurements in heavy-ion collisions where:

- The values of the correlation radii were found to be almost independent of the beam energy.
- The increase of the size of the femtoscopic radii increasing multiplicity in events.
- The decrease of the correlation radii with increasing pair transverse momentum k_T.

This can be understood as a manifestation of a strong collective flow. The LHC data extends the energy range of heavy-ion collisions significantly, and the energy dependence of the femtoscopic radii is found to scale with $\langle dN_{ch}/d\eta \rangle^{1/3}$. The ALICE "region of homogeneity" is almost twice the size of the same region for central RHIC collisions, and is found to scale linearly with $\langle dN_{ch}/d\eta \rangle$.

The three-dimensional $\pi\pi$ femtoscopic radii in $\sqrt{s} = 2.76\ TeV$ central $PbPb$ collisions are shown in Fig. 3.4. They are significantly larger than the radii measured in $\sqrt{s} = 200\ GeV$ central $AuAu$ in STAR [76]. Similar to the STAR data the ALICE radii show a clear dependence on k_T, with decreasing radii with increasing k_T. This is characteristic for an expanding source due to the smaller homogeneity lengths at larger k_T.

By comparing results for $\langle k_T \rangle = 0.3\ GeV/c$ with the results from other experiments one can get a beam energy dependence of the radii, presented in Fig. 3.5. The LHC data extends the energy range significantly, and the radii is found to scale with $\langle dN_{ch}/d\eta \rangle^{1/3}$.

The size of the homogeneity region can be represented as a volume $V = R_{out}R_{side}R_{long}$. The size of the ALICE "region of homogeneity" (Fig. 3.6) is almost twice as big as for central RHIC collisions. The size of the volume scales with $\langle dN_{ch}/d\eta \rangle$.

The centrality dependence of the femtoscopic radii are shown in Fig. 3.7. All three radii, for all k_T grow with decreasing centrality (i.e. increasing multiplicity). This is as expected since a system with larger initial size should also have a larger size at freeze-out. The k_T dependence of the radii is also found to hold for all centralities.

Femtoscopic studies in previous experiments have revealed a scaling in transverse mass m_T. The source sizes versus m_T for different particle types (π,K,p) fall on the same line. This m_T-scaling is expected to be an additional confirmation of a hydrodynamic expansion of the source. In Fig. 3.8 the correlation radii of several different pair types are presented as a function of transverse mass m_T. Correlations of both proton, kaon and pion pairs are shown to exhibit a m_T dependence.

Correlations have also been calculated for pp collisions, and it is interesting to see if it is possible to achieve the same scaling as for $PbPb$ collisions. It was found that while radii from pp collisions of different energies scale (Fig. 3.9), they do not scale with radii from $PbPb$ collisions. The top energies of pp collisions have multiplicities comparable to lower energy heavy-ion collisions, but still have a smaller radii.

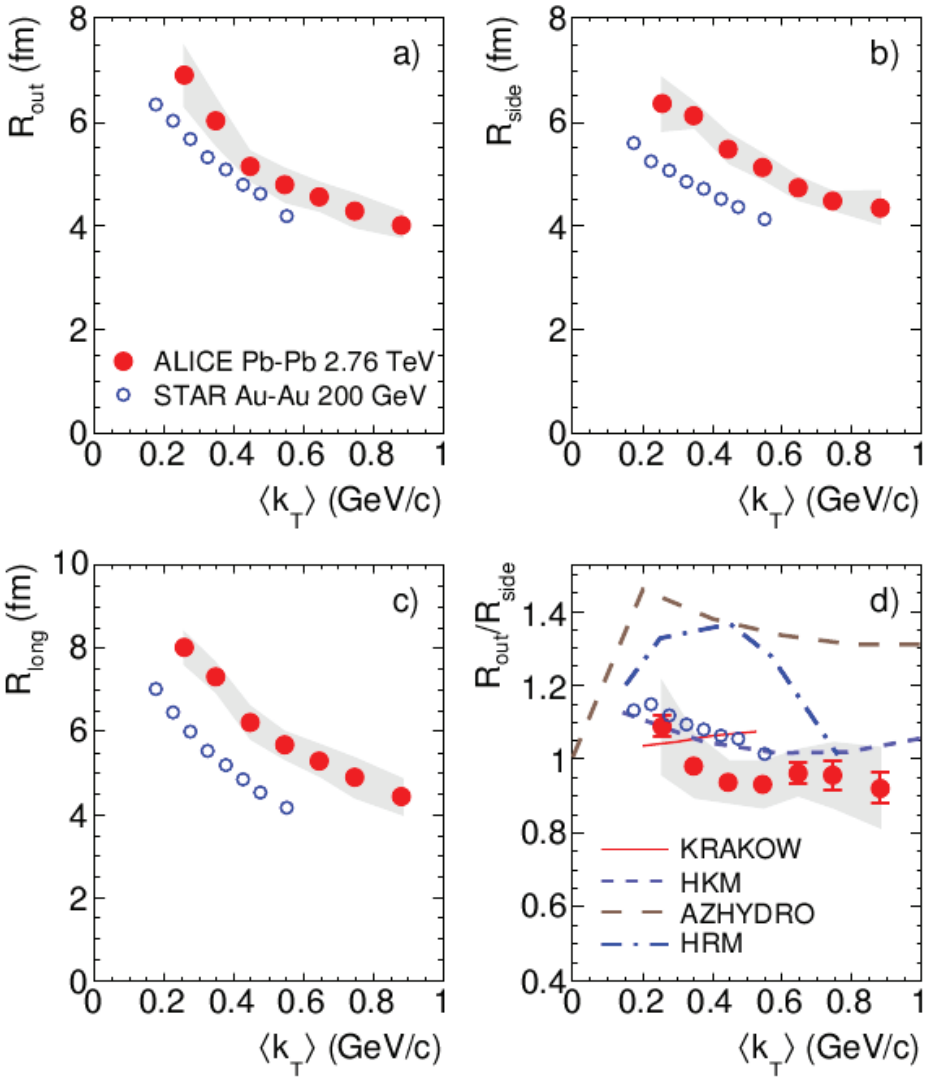

Figure 3.4: $\pi\pi$ femtoscopic radii for $\sqrt{s} = 2.76\ TeV\ PbPb$ collisions in ALICE as a function of k_T, compared with data from STAR. Figure taken from [77]

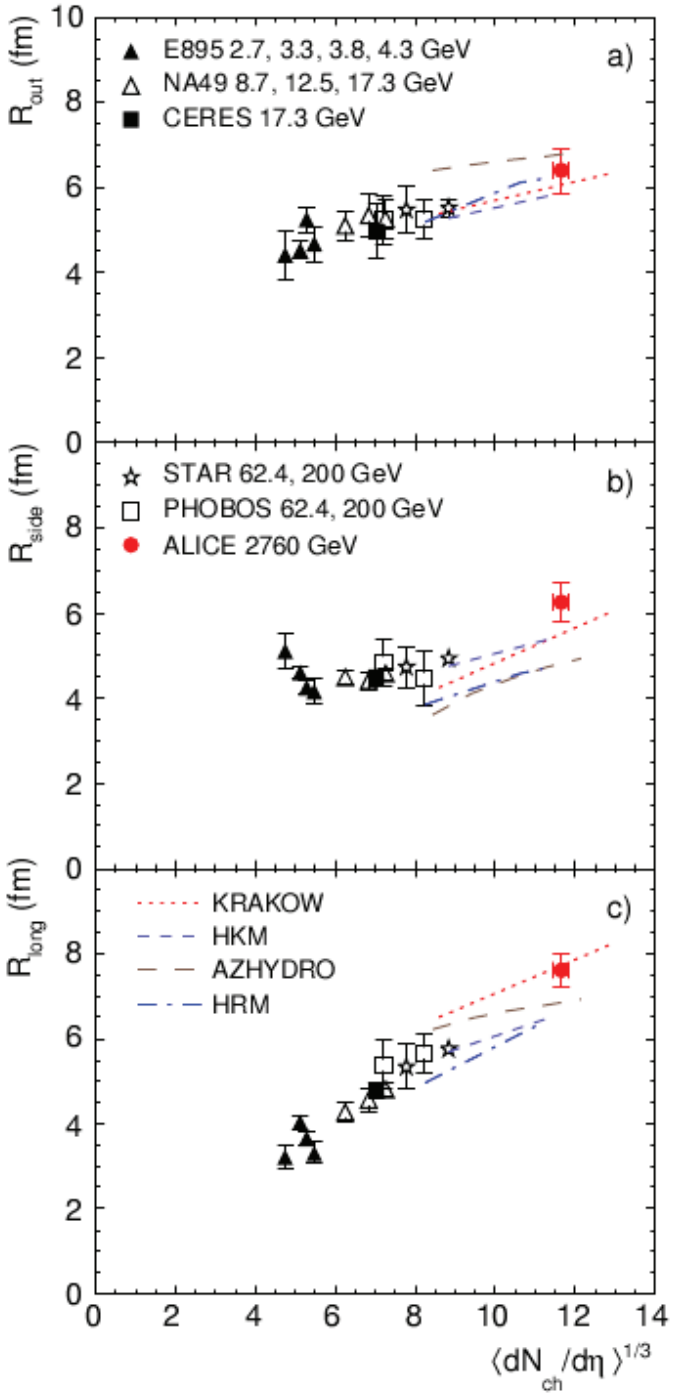

Figure 3.5: Beam energy dependence of the $\pi\pi$ radii at $k_T = 0.3\ GeV/c$. Figure taken from [77]

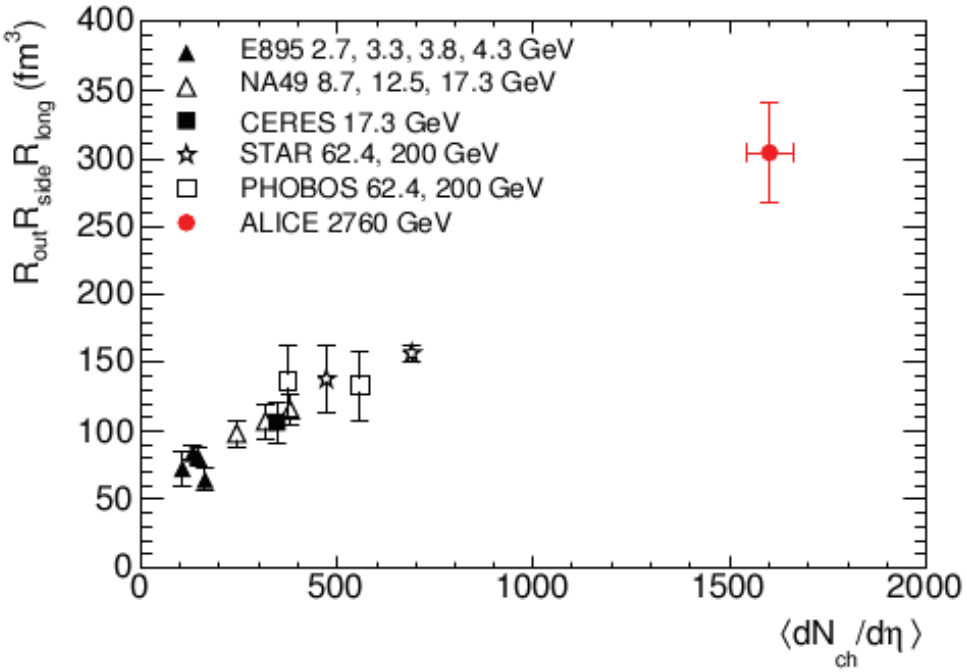

Figure 3.6: Size of the emission volume for $\pi\pi$ correlations in ALICE $PbPb$ $\sqrt{s} = 2.76\ GeV$ collisions at $k_T = 0.3\ GeV/c$, compared with data obtained from lower energy heavy-ion experiments. Figure taken from [77]

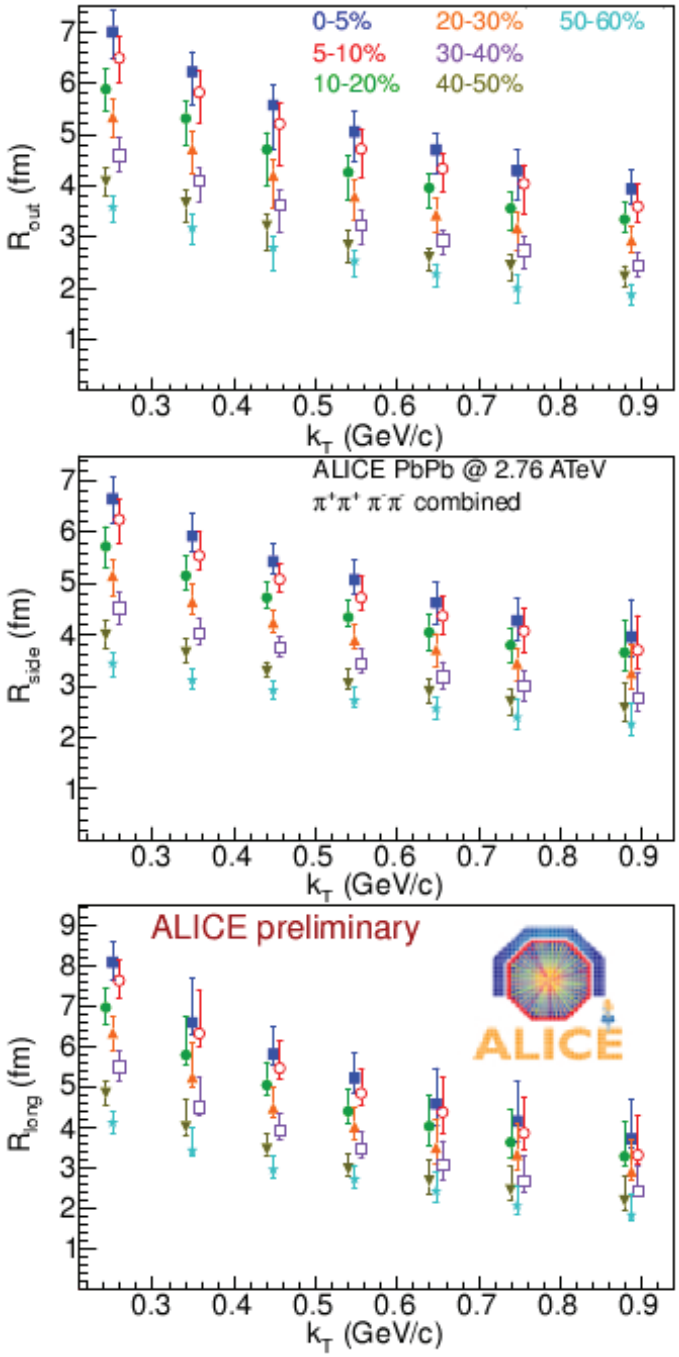

Figure 3.7: Centrality dependence of the $\pi\pi$ radii for ALICE $PbPb$ $\sqrt{s} = 2.76\ TeV$ collisions in all k_T bins. Figure taken from [78]

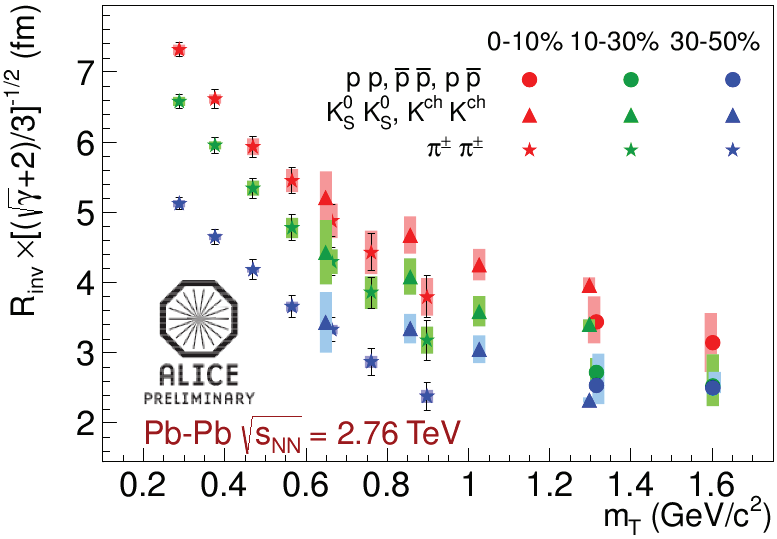

Figure 3.8: Approximate m_T scaling of different femtoscopic correlations in ALICE $PbPb$ $\sqrt{s} = 2.76\ GeV$ collisions. Figure taken from [79]

The system created in ultra-relativistic pp collisions at LHC energies might be similar to the system created in non-central heavy-ion collisions because of the large energy deposited on the overlapping region and therefore may also manifest a collective behaviour. The highly compressed strongly interacting system is expected to undergo longitudinal and transverse expansion, which may be observed through a decrease of the correlation radii with $\langle k_T \rangle$ and by the $\langle m_T \rangle$-scaling of the radii, as is the case in $PbPb$ collisions.

The ALICE collaboration have already studied two-pion correlation radii in pp collisions at $\sqrt{s} = 900\ GeV$ [80] and $\sqrt{s} = 7\ TeV$ [81], and K_0K_0 correlation radii in pp collisions at $\sqrt{s} = 7\ TeV$ [82, 83].

Two-pion Bose-Einstein correlations in pp collisions at $\sqrt{s} = 900\ GeV$ and $\sqrt{s} = 7\ TeV$ have been successfully described within the EPOS+hydro model [84, 85]. It was shown that the hydrodynamic expansion substantially modifies the source evolution compared to the "classical" EPOS scenario with independent decay of flux-tube strings, allowing one to describe the transverse momentum dependence of the correlation radii at high multiplicities. Our study with the QGSM model (Chapter 5) shows that at small multiplicities the pion correlation radii can be described by the "classical" string scenario. This observation coincides with EPOS observations.

Our experimental study of PiK correlations (Chapter 6) is performed as an additional study of the m_T dependence shown in Fig. 3.10, using non-identical correlations.

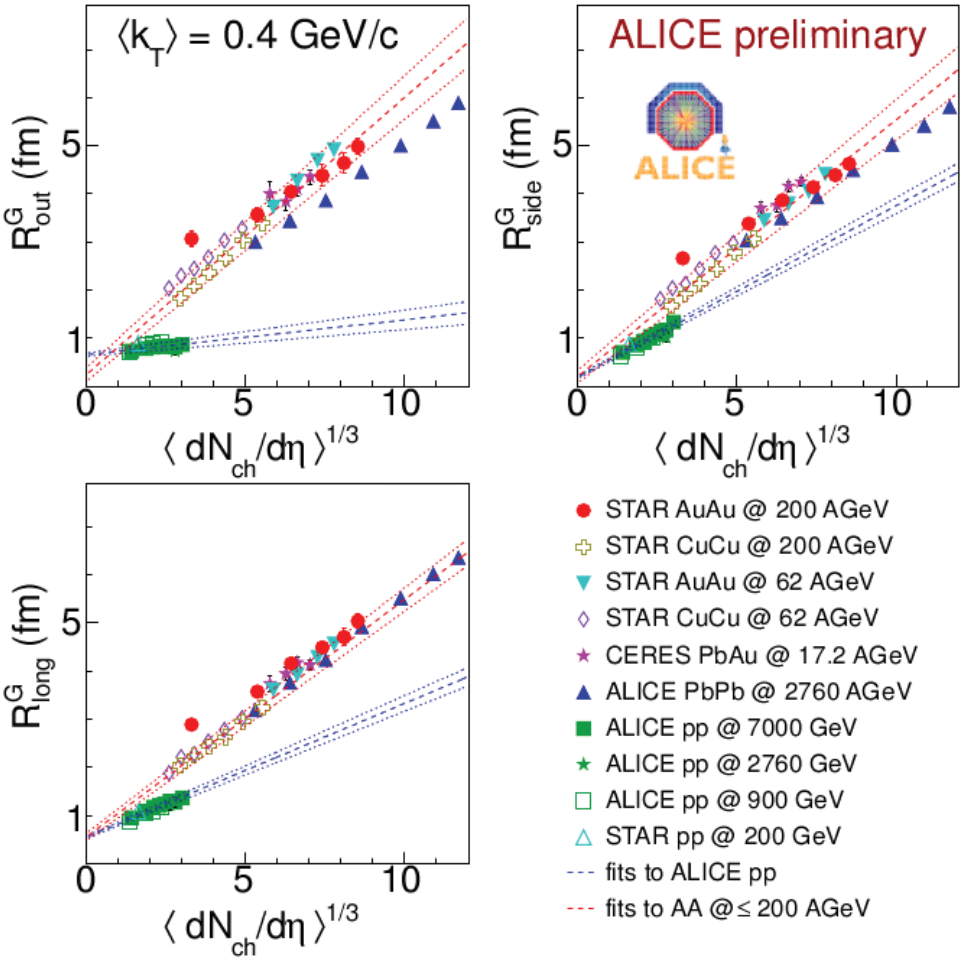

Figure 3.9: Comparison of femtoscopic radii, as a function of measured charged particle multiplicity, for many collision systems and collision energies. Lines show linear fits done separately to heavy-ion data and proton-proton data. Figure taken from [78]

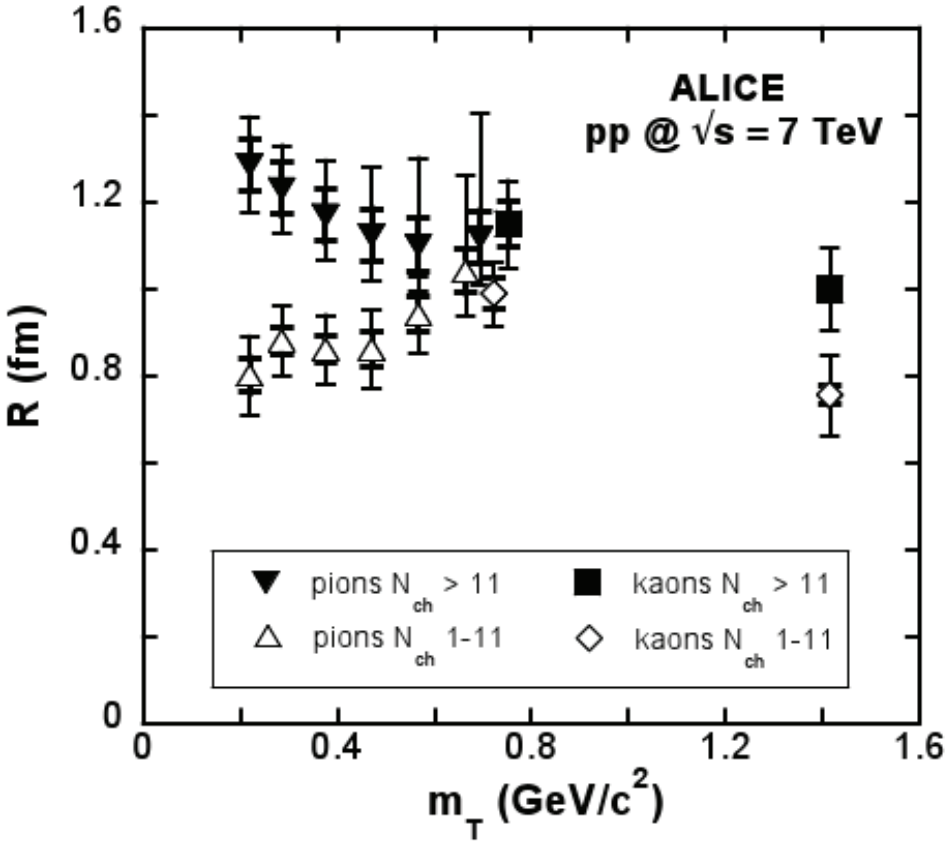

Figure 3.10: m_t dependence of the $\pi\pi$ and K_0K_0 correlation radii in ALICE pp $\sqrt{s} = 7\ TeV$ collisions. Figure taken from [86]

Chapter 4

Models

Theoretical models that simulate particle collisions are very useful tools that complement experiments and allow us to get a deeper understanding of the underlying physics. Models can be used in a predictive fashion and successful model predictions of data can be a powerful indication that the physics assumptions of the model are correct. But it is just as important to perform postdictions of experimental data. In such a case it is possible to tune the model parameters to explain the data.

Theoretical models can be roughly divided into two groups. Macroscopic models deal with collective phenomena and usually need some other model to transfer the final state of the simulation into particle spectra. The second group is microscopic models which deal with the evolution of individual particles as well as their interactions. This chapter will give a short introduction to hydrodynamic type models, the main form of macroscopic models. More attention will be given to string models, a form of microscopic models, and specifically the Quark Gluon String Model (QGSM) and the Ultra relativistic Quantum Molecular Dynamics model (UrQMD).

4.1 Hydrodynamic models

As discussed in chapter 2 a relativistic heavy-ion collision goes through many stages. After the initial collision a hot and dense matter of quarks and gluons is formed, and will rapidly equilibrate as it expands. With the system in local thermal equilibrium pressure gradients will lead to a dynamical evolution of the fireball. The system can be described through its macroscopic variables, e.g. temperature, pressure, volume, etc, and is governed by the equations of hydrodynamics. Energy-momentum, as well as other variables are conserved locally.

The energy-momentum of the fluid is described through its energy-momentum tensor:

$$T^{\mu\nu}(x) = (\epsilon(x) + P(x))u^{\mu}(x)u^{\nu}(x) - g^{\mu\nu}P(x) \tag{4.1}$$

where $\epsilon(x)$ is the energy density, $P(x)$ is the pressure and $u^{\mu}(x)$ is the four-velocity of the field at space-time point x. Conservation of energy-momentum is required:

$$\partial_{\mu}T^{\mu\nu} = 0 \tag{4.2}$$

and the four-velocity of the field must be normalised:

$$u_\mu u^\mu = 1 \tag{4.3}$$

The indices μ, ν go from 0 to 3, and following Einstein's summation convention indices appearing twice are summed over. This provides us with five equations, four from Eq. 4.2 and one from Eq. 4.3, while we have six variables: u_μ, ϵ and P. The last equation that is called the equation of state, links the pressure to the energy density of the system:

$$P = {c_s}^2 \epsilon \tag{4.4}$$

where c_s is the speed of sound in the medium. The hydrodynamic theory of particle production in ultra-relativistic collisions was put forward by Landau in 1953 [87]. For the sake of simplicity Landau chose the equation of state for an ideal gas of ultrarelativistic particles, implying that $c_s^2 = 1/3$. This has later been proven to be quite close to reality. In contrast to the model of Landau that assumed momentary stopping of the Lorentz contracted nuclei in the overlapping volume, the Bjorken model [88] considers the case where two nuclei pass through each other without stopping. This allows for a very elegant solution of the evolution of energy density in the volume:

$$\frac{d\epsilon}{d\tau} = -\frac{\epsilon + P}{\tau} \tag{4.5}$$

Here $\tau = \sqrt{t^2 - z^2}$ is the proper time of a fluid element.

There are some limitations to this approach. The initial pre-equilibrium stage of the early evolution is not included, but the hydrodynamic modelling can be used to find the necessary equilibration time of the system. Also the model can only provide the energy-momentum distribution at freeze-out. In order to get particle yields some other method, such as the Cooper-Frye prescription [89], must be employed. Once the particle yields are obtained it is possible to use a microscopic model as an afterburner during the cascade step of the simulation, for recent developments see [90] and references therein.

The macroscopic approach to the evolution of the system has been very successful in predicting and describing many experimental observables, over a large energy range. The results from RHIC of the QGP as a perfect liquid has further increased the importance of hydrodynamic models as a method for studying heavy-ion collisions [12, 14]. In [90] the hybrid hydrokinetic model hHKM is used along with the Cooper-Frye prescription and particle cascade with the UrQMD microscopic model. The femtoscopic radii calculated with this approach are presented in Fig. 4.1 and v_2 is presented in Fig. 4.2.

4.2 Microscopic models

In microscopic models the full evolution of all particles created is described. Such a model can be based on fundamental QCD or it can be an effective model. The main advantage of doing calculations with a microscopic model is that you have the complete information about the collision, and in addition to calculating experimental observables it is also possible to study the direct causes of the behaviour of the observable.

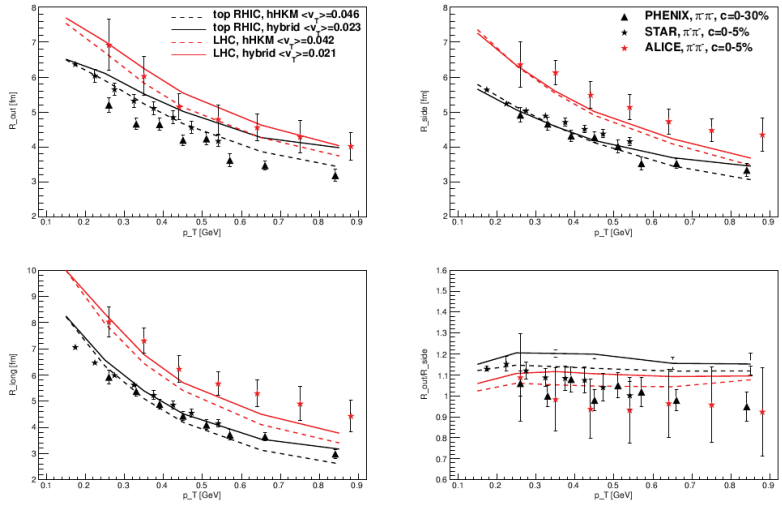

Figure 4.1: Femtoscopic radii of π^- pairs for central events in the hHKM model at RHIC and LHC energies, compared with data from the STAR, PHENIX and ALICE experiments. Figure taken from [90]

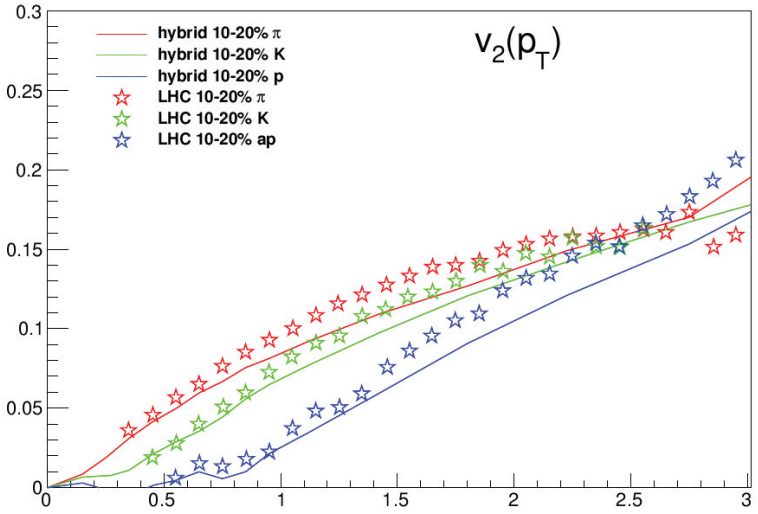

Figure 4.2: Elliptic flow calculated at $\sqrt{s} = 2.76\ TeV$ in the hHKM model compared with data from the ALICE experiment. Figure taken from [90]

4.2.1 String models

String models are a form of effective microscopic models where particle production is done through the excitation and breaking of colour flux-tube strings. The string picture was first introduced in the Lund model [91] which we will describe in more detail below. The essence of the string picture is that the fireball is described as interactions between quarks and colour flux-tube strings.

The Lund model is a quark-parton model. It is semi-classical in nature, but is however quantum mechanically constrained. Such a constraint is Heisenberg's uncertainty principle:

$$\Delta p \Delta x \geq 1 \tag{4.6}$$

This means we can not get both momentum p and position x with a high precision. We can however employ the rapidity y for large energies:

$$\Delta y = \Delta p / E \tag{4.7}$$

which gives

$$\Delta y \Delta x \geq 1/E \tag{4.8}$$

From this equation it is obvious that for large enough energies we can describe both rapidity and position of a particle to a large precision.

Yo-yo particles

Let us look at a system of two particles in their Centre of Mass System (CMS). If the particles are electrically charged the field lines will spread out through space. If the particles have a colour charge however the colour field lines will not spread out, but remain in a thin tube-like region, a colour flux tube. This is because of the gluon-gluon interaction. If we try to separate the particles we know from asymptotic freedom in QCD that the energy in the flux tube will increase, and eventually the tube will break by creating new $q\bar{q}$-pairs from the vacuum.

We will consider the bound state of a massless quark and an anti-quark in 1+1 dimensions. Since they are massless the quarks always move with the speed of light. The Hamiltonian for the pair-system is:

$$H = T + V = |p_1| + |p_2| + \kappa |x_1 - x_2| \tag{4.9}$$

Here the kinetic part T is given by the momenta of the two particles p_1, p_2, and the potential energy V is given by the positions x_1, x_2 and the string tension parameter κ. The Hamiltonian equation of motion $\dfrac{dp}{dt} = -\dfrac{dH}{dx}$ gives us:

$$\frac{dp_i}{dt} = \pm\kappa \tag{4.10}$$

The system is in a so-called "yo-yo mode". Both quarks are moving away from each other with the speed of light until they reach a maximum relative distance L. At this point $p_1 = p_2 = 0$ and $L = |x_1 - x_2|$. The quarks will simultaneously change direction and move towards each other

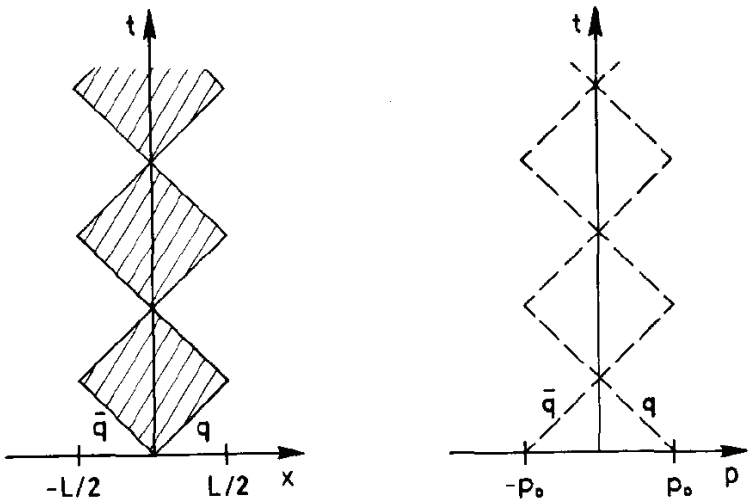

Figure 4.3: The time evolution of the position and momentum of the quarks in the "yo-yo"-system in the centre of mass frame. Figure taken from [91]

until they pass and reach the maximum relative distance L again. The evolution of the yo-yo system is shown in Fig. 4.3.

In this system with two massless quarks the mass of the bound system is carried by the colour flux tube. The mass of the system is given by the string tension and the maximum relative distance $M = \kappa L$. Since the particles move at the speed of light the period for the "yo-yo" motion is $T = 2L = 2M/\kappa$. The area A spanned by the motion of the quarks is proportional to M^2:

$$A = \frac{M^2}{\kappa^2} \tag{4.11}$$

Up to now we have considered the quarks in the CMS frame, but we can also look at the "yo-yo" particles from another frame, e.g. the lab frame, by a Lorentz boost β. In the CMS frame we have $x_i = \pm t$ and $E_i = \pm p_i$, we Lorentz boost and get:

$$\begin{aligned} t' &= \gamma(t - \beta x_i) = \gamma(1 \mp \beta)t \\ p'_i &= \gamma(p_i - \beta E_i) = \gamma(1 \mp \beta)p_i \end{aligned} \tag{4.12}$$

which show that the equation of motion is Lorentz invariant:

$$\frac{dp'}{dt'} = \frac{dp}{dt} = \pm\kappa \tag{4.13}$$

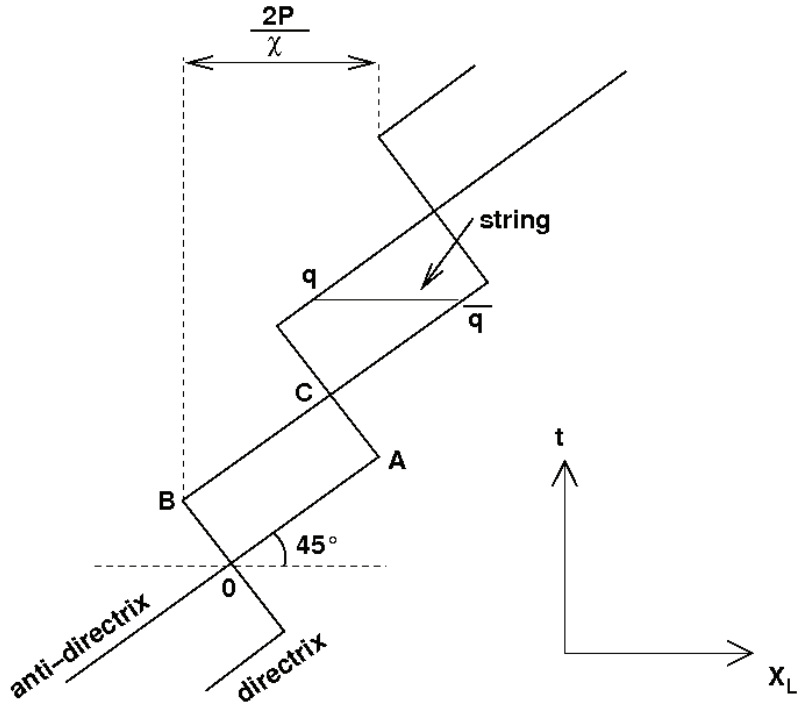

Figure 4.4: Time evolution of the position of the quarks in the "yo-yo"-system in the lab frame. Figure taken from [8]

In the new frame the maximum distance L' is Lorentz contracted and the period T' is time dilated:

$$\begin{aligned} L' &= \gamma(1-\beta)L = L\exp(-y) \\ T' &= \gamma T = T\cosh y \end{aligned} \tag{4.14}$$

where y is the rapidity difference between the two frames.

The first crossing point in the new frame happens at $t = T'/2, x = T'/2 - L'$. This gives us the velocity v' of the system in the new frame:

$$v' = \frac{T'/2 - L'}{T'/2} = \frac{1}{2}\frac{T - 2(1-\beta)L}{T} = \frac{L-(1-\beta)L}{L} = \beta \tag{4.15}$$

The "yo-yo"-system moves with a constant velocity β with an initial position of $x(t=0) = 0$. Not surprising since we gave the system a boost of β. Note that while the system (i.e. the particle) moves with a speed β, the individual quarks still move with the speed of light. An illustration of the "yo-yo"-system in lab frame is given in Fig. 4.4.

All momentum in the system is carried by the endpoint quarks, this is possible because the only system where both quarks have zero momentum simultaneously is the CM frame.

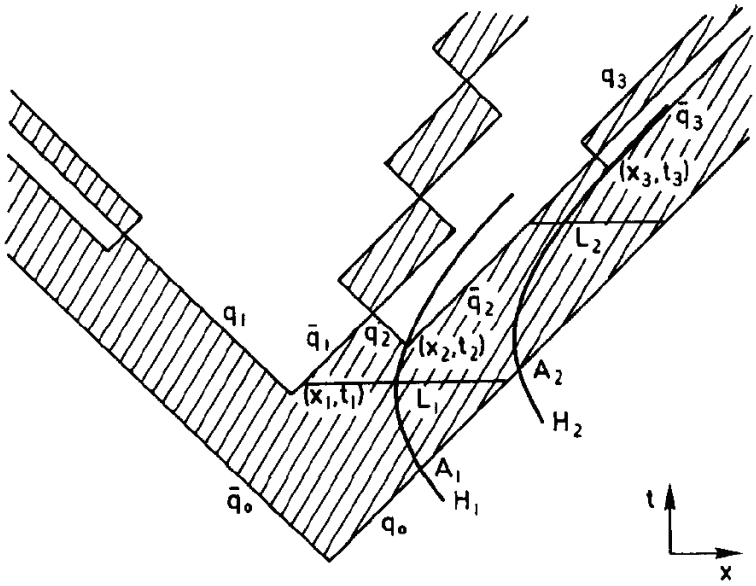

Figure 4.5: Particle production from string fragmentation in the "yo-yo"-model. Figure taken from [91]

Particle production

We will now look at particle production from the breaking of the string between two quarks moving in opposite direction.

Again we look at two quarks q_0 and $\bar{q}_0$ in their CMS, moving in opposite directions. At time t_1 and point x_1 the string breaks and produces a new quark pair $q_1\bar{q}_1$ moving in opposite directions. At time t_2 and point x_2 a second quark pair $q_2\bar{q}_2$ is produced moving in opposite directions. The quarks $\bar{q}_1 q_2$ will pass each other and form a "yo-yo" system. More $q\bar{q}$ pairs are produced as the original string breaks further, creating $q_i\bar{q}_j$ "yo-yo" subsystems. This is seen in Fig. 4.5

The hadron formed from $\bar{q}_1 q_2$ needs to have a proper mass m. The energy is $E = \kappa(x_2 - x_1)$ and the momentum is $\kappa(t_2 - t_1)$. The mass is then described by:

$$(x_2 - x_1)^2 - (t_2 - t_1)^2 = m^2/\kappa^2 \tag{4.16}$$

This is a hyperbola parametrised by:

$$(x_2 - x_1, t_2 - t_1) = \frac{m}{\kappa}(\cosh y, \sinh y) \tag{4.17}$$

Here we recognise $L = m/\kappa$ as the maximum relative distance between the particles and $L^2 =$

m^2/κ^2 as the area spanned by the quarks in the CMS of $\bar{q}_1 q_2$. y is the rapidity of the hadron in the lab frame.

Due to the fact that the hadron is a composite object, the formation time is not well defined in this model. One possible definition is the first time the quarks in the hadron pass, "yo-yo" formation time. A second possibility is the time where the last quark in the hadron is formed, "constituent" formation time. The choice of formation time is arbitrary, but must be used consistently. Constituent formation time is chosen as it has been found to be in accordance with experimental data [92].

The pair production points are casually disconnected. In quantum mechanical terms a produced particle is initially virtual before it becomes "on-shell" and becomes able to interact.

Yo-yo with heavy quarks

It is also possible to consider the case where the quarks in the "yo-yo" system are not massless. In this case the quark motion follows hyperbola instead of the light-cone:

$$(x - x_1)^2 - (t - t_1)^2 = \mu^2/\kappa^2 \tag{4.18}$$

where μ is the mass of the quark. The asymptotes of the hyperbola will correspond to the motion of massless quarks. Two quarks with hyperbola centres (x_1, t_1) and (x_2, t_2) can then form a hadron with mass m that satisfy the same conditions as for massless quarks:

$$(x_2 - x_1, t_2 - t_1) = \frac{m}{\kappa}(\cosh y, \sinh y) \tag{4.19}$$

One major difference from massless quarks is that energy-momentum conservation means that a $q\bar{q}$ pair can not be created at a single space-time point. The quarks have to be produced with some spatial separation. Even so the majority of the mass of the particle is still carried by the string, so a yo-yo with heavy quarks is a complication without much gain.

4.2.2 The Quark Gluon String Model

The description of soft hadronic processes cannot be done within pertubative QCD. Therefore, the quark-gluon string model [93] employs the so-called $1/N$ series expansion [94, 95] of the amplitude for processes in QCD, where N is either number of colours N_c [94] or number of flavors N_f [95]. In this approach the amplitude of a hadronic process is represented as a sum over diagrams of various topologies, so the method is often called *topological expansion*. It appears that at high energies and small momentum transfer the arising diagrams are similar [96, 97] to processes describing the exchange of Regge singularities in the t-channel. For instance, planar diagrams correspond to the exchange of Reggeons, and cylinder diagrams correspond to reactions without quantum number exchange in the t-channel, i.e., taking place via the Pomeron exchange, where Pomeron is a composite state of the reggeised gluons. Processes with many-Pomeron or many-Reggeon exchanges are also possible. To find the amplitude of multiparticle production one has to cut the diagrams in the s-channel, and the physical picture of quark-gluon strings arises. Namely, new particles are produced through the formation and break-up of quark-gluon

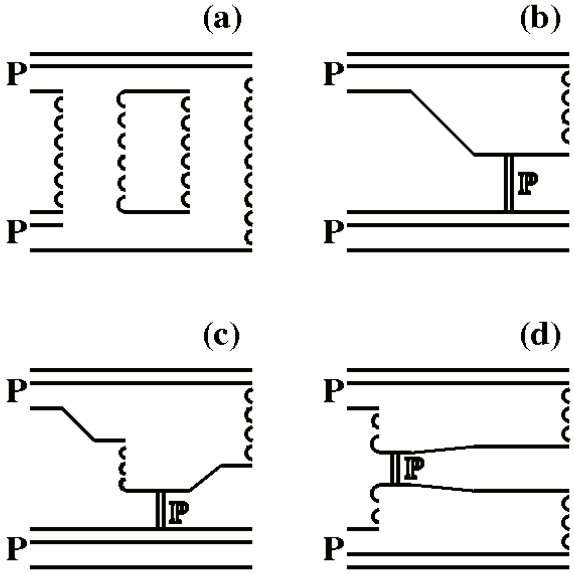

Figure 4.6: Diagrams of particle production processes included in the modelling of pp interactions at ultrarelativistic energies. See text for details.

strings or exited objects consisting of quarks, diquarks and their anti-states connected by a gluon string.

Figure 4.6 shows the subprocesses with particle creation taken into account in the current Monte Carlo version of the QGSM [98] for pp collisions at ultrarelativistic energies. The inelastic cross section consists of three terms

$$\sigma_{inel}^{pp}(s) = \sigma_P(s) + \sigma_{SD}(s) + \sigma_{DD}(s) \; , \tag{4.20}$$

where $\sigma_P(s)$ is the cross section for the multi-chain processes described by the cylinder diagram and diagrams with multi-Pomeron scattering [Fig. 4.6(a)], $\sigma_{SD}(s)$ by the single diffractive processes with small [Fig. 4.6(b)] and large [Fig. 4.6(c)] mass excitation, corresponding to the triple-Reggeon and triple-Pomeron limit, respectively, and $\sigma_{DD}(s)$ by the double diffractive diagram [Fig. 4.6(d)]. Other diagrams that are relevant at low and intermediate energies, such as

undeveloped cylinder diagram or diagram with quark rearrangement [98], play a minor role here because their cross sections rapidly drop with rising s. The statistical weight of each subprocess is expressed in terms of the interaction cross section for the given subprocess $\sigma_i(s)$

$$\omega_i = \sigma_i(s)/\sigma_{inel}(s) \; . \tag{4.21}$$

Then, the hadron inelastic interaction cross section $\sigma_{inel}(s) = \sigma_{tot}(s) - \sigma_{el}(s)$ is split into the cross section for single diffractive interactions $\sigma_{SD}(s)$ and the cross section for non-diffractive reactions $\sigma_{ND}(s)$, as it is usually done in analysis of experimental data. By means of the Abramovskii-Gribov-Kancheli (AGK) cutting rules [99] the inelastic non-diffractive interaction cross section $\sigma_{ND}(s)$ can be expressed via the sum of the cross sections for the production of $n = 1, 2, \ldots$ pairs of quark-gluon strings, or cut Pomerons, and the cross section of double diffractive process

$$\sigma_{ND}(s) = \sum_{n=1}^{\infty} \sigma_n(s) + \sigma_{DD}(s) \; . \tag{4.22}$$

The main interest in using this model in this work comes from its impressive predictive power. QGSM has been used to calculate transverse momentum and pseudorapidity distributions of $\bar{p}p$ and pp collisions for centre of mass energies $\sqrt{s} = 200\ GeV$, $546\ GeV$, $900\ GeV$, $1800\ GeV$, $2360\ GeV$ and $7\ TeV$. These calculations have been compared with experimental data from the UA1, CDF, E375, ALICE and CMS collaborations. At such high energies the annihilation cross section is almost zero and the main characteristics of particle production in pp and $\bar{p}p$ interactions are essentially similar. Figs. 4.7 and 4.8 shows the transverse momentum and pseudorapidity distributions respectively. One can see that QGSM offers a good description of experimental data across almost two orders of magnitude of energies.

4.2.3 The Ultrarelativistic Quantum Molecular Dynamics model

The Ultra-Relativistic Quantum Molecular Dynamics model (UrQMD) [100, 101] is a microscopic model designed for hadron-hadron, hadron-nucleus and nucleus-nucleus collisions. The model is based on a phase-space description of the colliding system. Both hadronic and partonic interactions happen through string formation and fragmentation. It contains 55 baryon and 32 meson states with corresponding antiparticles and isospin-projected states.

The energy range of the model is from a hundred MeV to hundreds of GeV. At low energies, up to beam energies of $10\ GeV$/nucleon, the particle production is dominated by resonance decays of mesons and baryons. At higher energies string excitation and fragmentation dominates.

The model contains many unknown parameters which have to be fixed by experimental data or model assumptions. The elementary cross-sections are fitted to the available proton-proton, proton-neutron and pion-proton data.

In contrast to QGSM, which is based on a colour exchange mechanism, UrQMD employs the classical Lund picture of longitudinal excitation of the strings (Fig. 4.9). Particle production also happens through string fragmentation. The colour string is assumed to be uniformly stretched and produced hadrons will then be uniformly distributed in rapidity between the endpoints of the string. Produced hadrons are propagated using the Hamiltonian equations of motion.

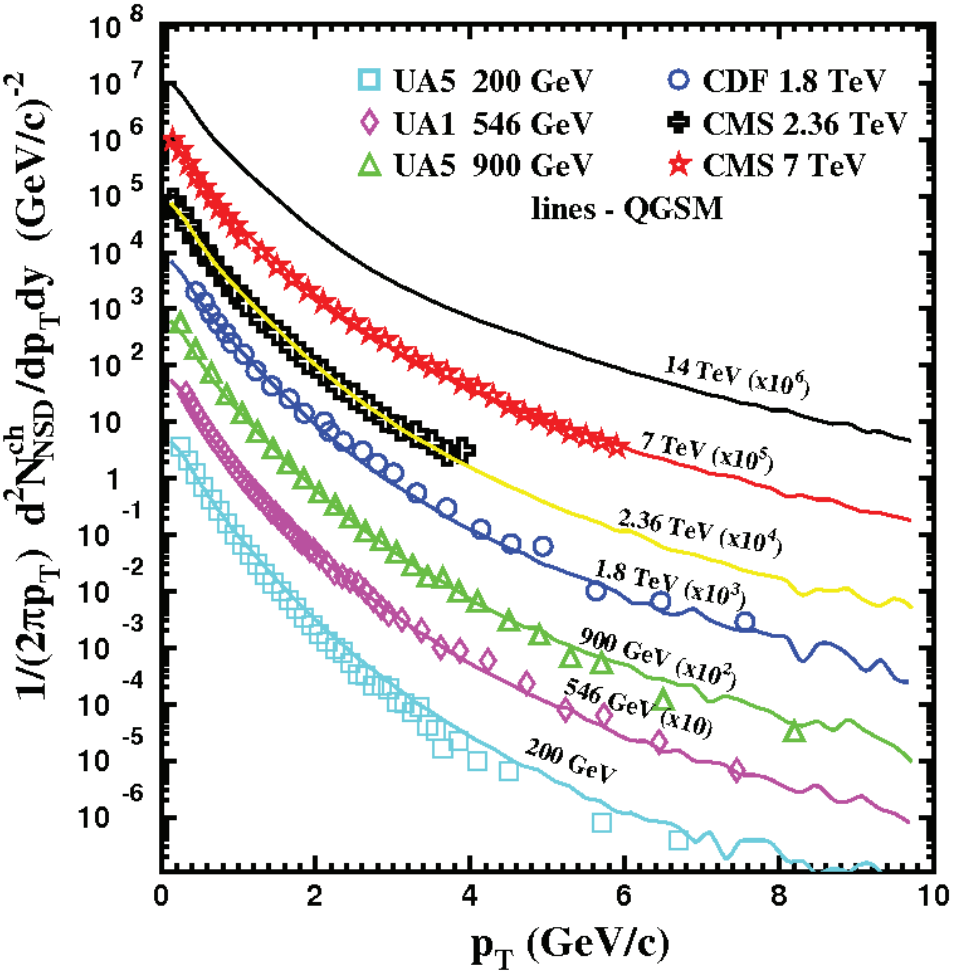

Figure 4.7: Transverse momentum distributions of the invariant cross section of charged particles in Non-Single Diffractive (NSD) pp collisions obtained in QGSM at $|y| \leq 2.5$ for all energies in question. Experimental data are taken from [102, 103, 104, 105].

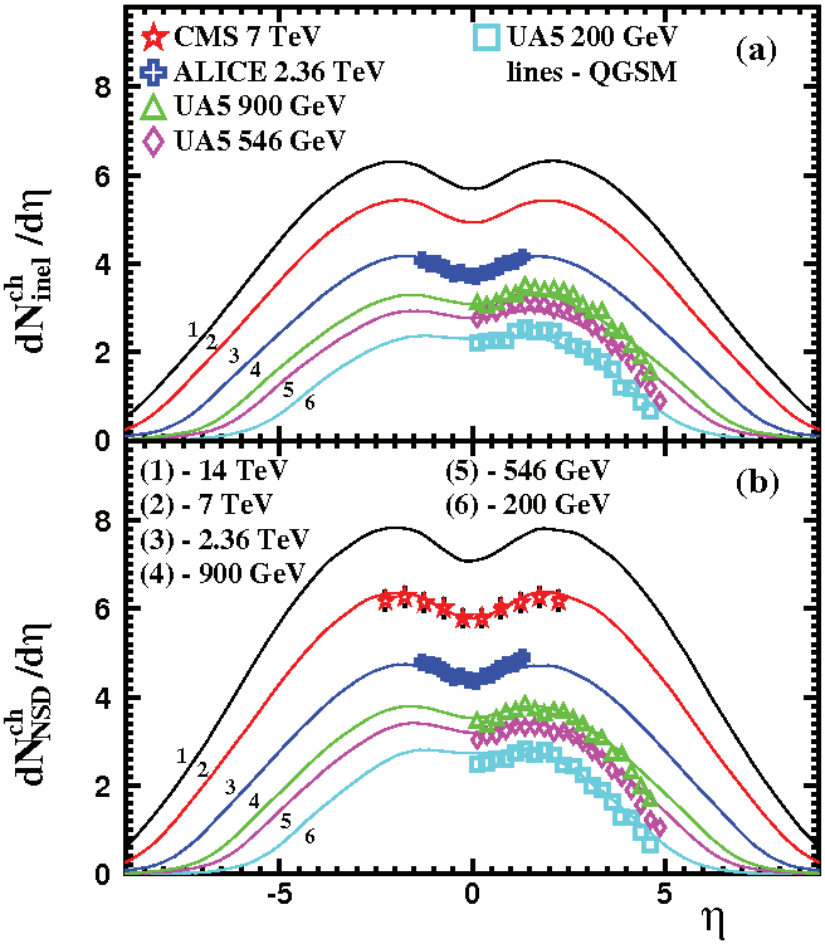

Figure 4.8: The charged particle pseudorapidity spectra for (a) inelastic and (b) non-single diffractive events calculated in QGSM for pp collisions at $\sqrt{s} = 200$ GeV (6), 546 GeV (5), 900 GeV (4), 2.36 TeV (3), 7 TeV (2) and 14 TeV (1). Data are taken from [102, 105, 106].

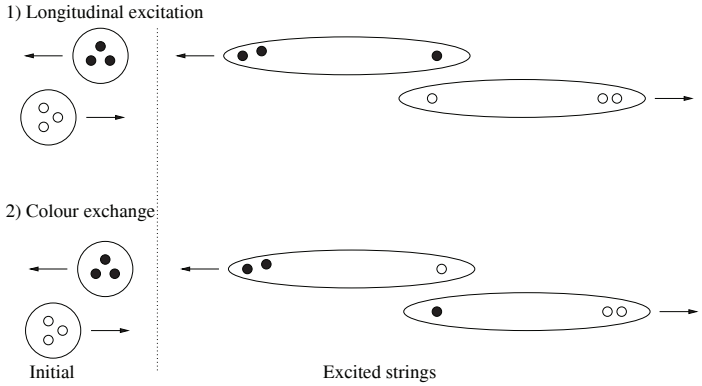

Figure 4.9: Schematic illustration of string excitation mechanisms. The first example is the longitudinal excitation employed in the Lund-based models. The second example is the colour exchange mechanism used by among others the QGSM model. In both cases the figure shows initially two protons moving towards each other, with the valence quarks of each proton depicted. The strings then become longitudinally excited, with an exchange of quarks between the hadrons in the second example.

The UrQMD model gives good agreement with experimental data, in particular it describes the transverse mass spectra of hadrons in different rapidity intervals.

Chapter 5

$\pi\pi$ correlations in QGSM pp collisions at RHIC and LHC energies

Theoretical studies of high-energy particle collisions through the use of effective models give important complementary results to experimental results. The use of such models prior to the experiments gives predictions of results and offers proof of how good our understanding is of the basic processes of a collision. After the experimental results have been published postdictions from models are used to better our understanding. By changing parameters and turning on or off processes in the model, the important contributions to the experimental results can be identified.

Two types of models, hydrodynamic and microscopic, have been described earlier in this thesis. For this work a microscopic model, the Quark Gluon String Model (QGSM), will be used. Simulations from the model at RHIC and low LHC energies will be used to calculate two-pion momentum correlations and then compared with the experimental results. Since we have the full information of what happens in the evolution of the system in the model, we can find the important contributions to both the size of the system, and the dependence of the radius with transverse momentum.

The complete information given to us by the model also offers the possibility to study particle spectra at freeze-out, and use this information in conjunction with the femtoscopic data in order to gain a more complete picture of the system.

5.1 Freeze-out study

The position and momentum of all particles at freeze-out in QGSM are readily available. This data can be taken and plotted to show the distributions of particles at freeze-out. The distributions are shown separately for four different particle species: π, K, p and $\Lambda + \Sigma^0$. These are two mesons and two baryons, one which is more populous for each type, and which exhibit a clear mass hierarchy. In this way differences and similarities between particle species can be seen.

We study separately the last interaction points of the particles produced in inelastic and in elastic collisions, as well as in resonance decays. Inelastic collisions are responsible for chemical equilibration of the system, while elastic collisions drive the system towards thermal equilibra-

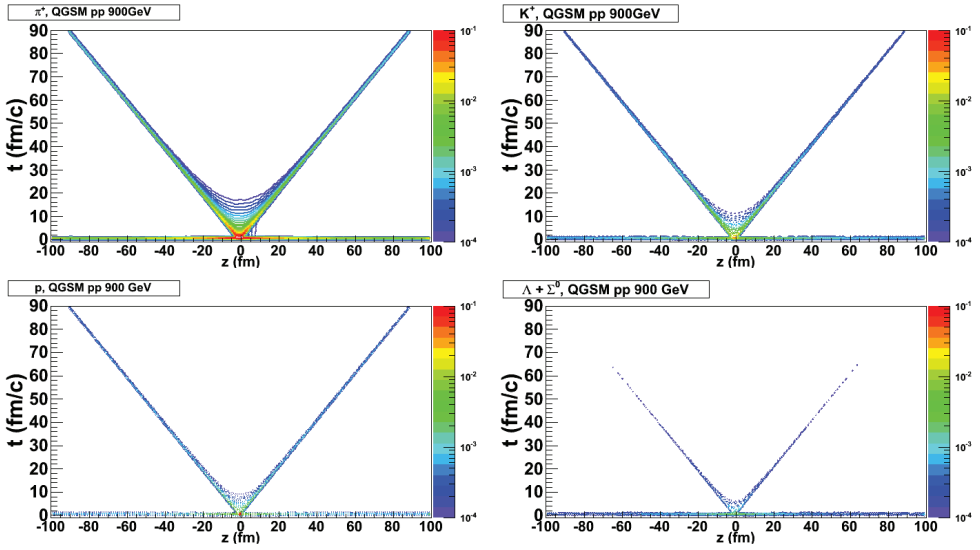

Figure 5.1: $\frac{d^2N}{dzdt}$ distributions from pp 900 GeV in QGSM

tion. Resonance decays characterise mostly the individual properties of the emitted particles.

The phase-space distribution of the particles on the mass shell is a function of seven independent variables: $(\vec{r}, \vec{p}, t)$. For the sake of simplicity some variables are integrated over and different space-time and phase-space three-dimensional distributions are studied separately. In the case of central collisions of symmetric nuclei, where two coordinates in the transverse plane (x, y) as well as (p_x, p_y) are equivalent, there are only ten different coordinate pairs: (t, z), (t, r_T), (t, p_z), (t, p_T), (z, r_T), (z, p_z), (z, p_T), (r_T, p_z), (r_T, p_T) and (p_z, p_T) [108].

The distributions that have been calculated are the longitudinal position versus time distribution $\frac{d^2N}{dzdt}$ (Fig. 5.1), the transverse mass versus time distribution $\frac{d^2N}{m_T dm_T dt}$ (Fig. 5.2), and the transverse radius versus time distribution $\frac{d^2N}{r_T dr_T dt}$ (Fig. 5.3). These 2-dimensional distributions give visual information about the evolution of the system, and will be discussed in more detail below.

In general all the freeze-out distributions show the mass hierarchy of the particles in question. Heavier particles freeze out earlier in the evolution as heavier string become less prevalent. From the decreasing freeze-out times we can see the relation of the masses: $m_\pi < m_K < m_p < m_{\Lambda,\Sigma^0}$.

The $\frac{d^2N}{dzdt}$ distributions are shown in Fig. 5.1. They show the freeze out time of the particles on the y-axis and the freeze-out position in the beam direction on the x-axis. At time zero the effects of the initial collision can be seen, with a large number of directly produced particles

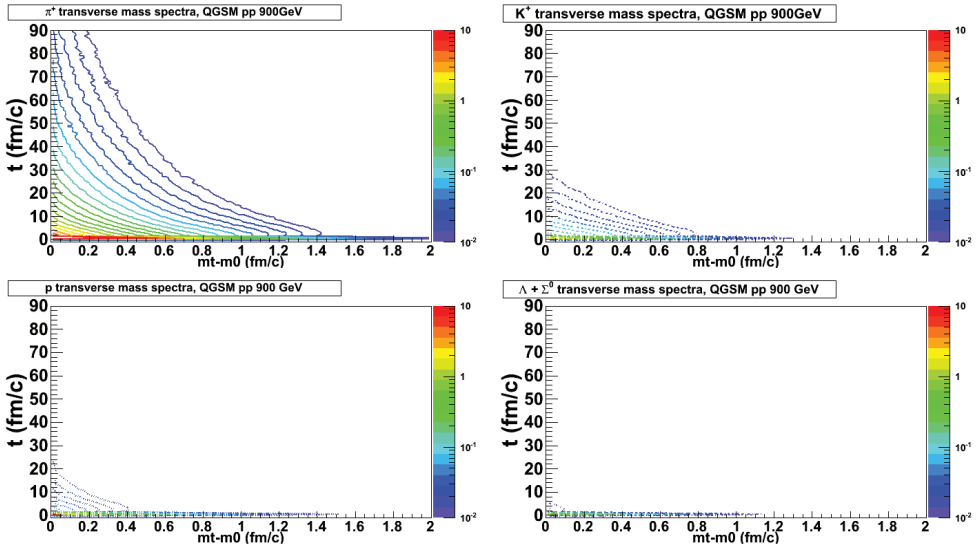

Figure 5.2: $\frac{d^2N}{m_T dm_t dt}$ distributions from pp 900 GeV in QGSM

freezing-out early. A greater density of particles can be seen closer to the centre of the collision. As time passes resonances are continuously produced as the two remnants of the collision are moving in opposite directions. The heavier particles have a sharper peak. Production of pions takes place up to $t \sim 18\ fm/c$ in the central zone of the collision, whereas for kaons, protons and lambdas these times reduce to 12, 10 and 7 fm/c respectively.

The $\frac{d^2N}{m_T dm_t dt}$ distributions are shown in Fig. 5.2. They show the freeze out time of the particles on the y-axis and the freeze-out transverse mass on the x-axis. Again the initial directly produced particles appear at time zero. They go up to $m_t - m_0 = 2\ GeV/c$ with the main body of particles at lower momentum. A second peak can be seen just a few fm/c after the initial collision, this peak comes from short lived resonances decaying. With increasing freeze-out time we have the continuous production of particles from resonance decay, with decreasing transverse mass.

The $\frac{d^2N}{r_t dr_t dt}$ distributions are shown in Fig. 5.3. They show the freeze out time of the particles on the y-axis and the transverse radial position of the particles in the x-axis. We see the directly produced particles at time zero, with greater concentration at smaller radius. Here the second peak from short lived resonances is more pronounced, with a maximum r_t at a later time. Looking at the particles produced from resonance decays we can see an interesting "Hubble-like" expansion of the system as the freeze-out time increases.

Finally, the space-momentum correlations in the model are important in relation to femto-

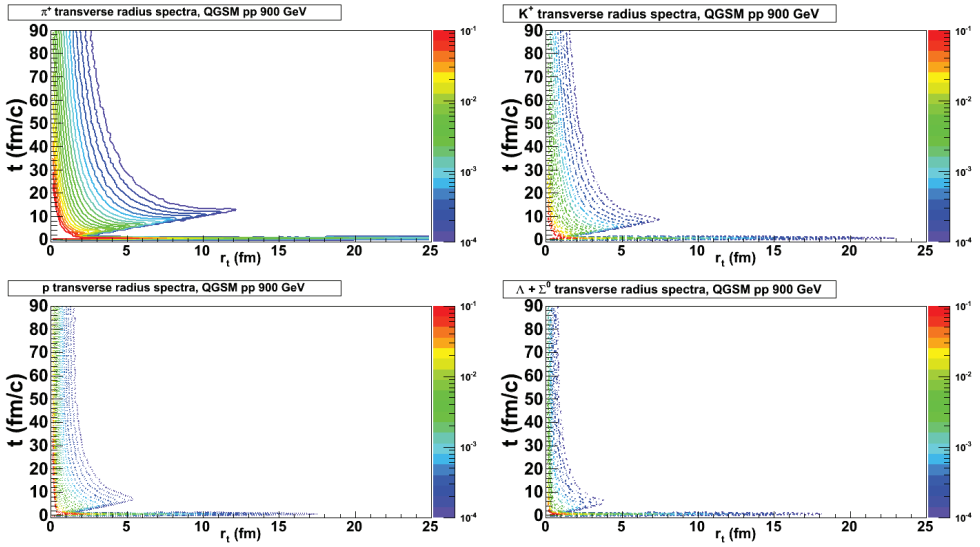

Figure 5.3: $\frac{d^2N}{r_t dr_t dt}$ distributions from pp 900 GeV in QGSM

scopic studies. The $p_x - x$ distribution illustrates this correlation and is presented in Fig. 5.4. Here the correlation in the sign of p_x and x is clearly demonstrated. These correlations look similar to the space-momentum correlations of hydrodynamic models, where they arise due to transverse collective flow. In the QGSM model these correlations arise naturally from the LUND hadronisation schema, as described in Eq. 5.1.

5.2 Momentum correlations

The main theoretical study of this thesis has been the usage of the QGSM model to calculate $\pi\pi$ femtoscopic correlations at $200\ GeV$ and $900\ GeV$ which is RHIC and LHC energies respectively. These model calculations have then been compared to published experimental data from STAR and ALICE [76, 80]. The results of this study has been published in [107], the publication is attached in appendix II. In this thesis we will present these results and make connections with the freeze-out pictures presented in section 5.1 in order to put the work into a greater perspective.

As presented in section 4.2 the string length $L = M_s/\kappa$ is dependent on the mass of the string M_s and the string tension κ. At this point it is important to make a choice of either constituent or yo-yo time, and in the present version of the QGSM model constituent formation time is chosen for reasons described in section 4.2. The formation time t^* and coordinate z^* of the i-th hadron

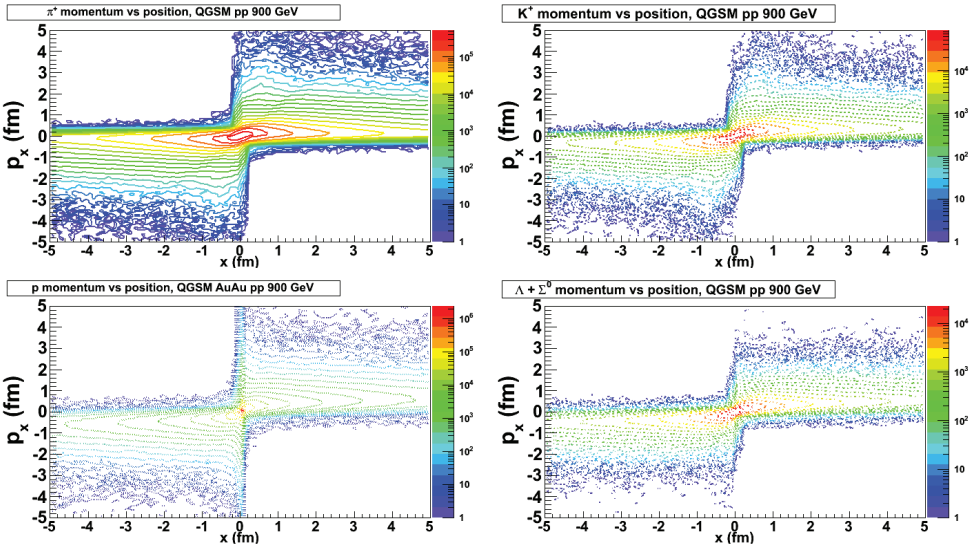

Figure 5.4: $p_x - x$ distributions from pp 900 GeV in QGSM

in the string centre of mass can be expressed as (for derivation see appendix A):

$$
\begin{aligned}
t_i^* &= \frac{1}{2\kappa}\left(M_s - 2\sum_{j=1}^{i} p_{zj}^*\right) \\
z_i^* &= \frac{1}{2\kappa}\left(M_s - 2\sum_{j=1}^{i} E_j^*\right).
\end{aligned}
\tag{5.1}
$$

Here p_{zj}^* and E_j^* is the longitudinal momentum and energy respectively of the j-th hadron produced by the decay of the string. We can then calculate the time t_i in the laboratory frame and boost the coordinates to this point.

$$
\begin{aligned}
a_i &= a_{0i} + t_i p_{ai}/E_i \\
a &= x, y, z
\end{aligned}
\tag{5.2}
$$

We can see from the equations that an increase in string tension will cause a reduction in formation time. As the formation time is essential for the sizes calculated from the femtoscopic method, we introduce a scaling of the string tension $\kappa = \alpha\kappa_0$ where $\kappa_0 = 0.88\ GeV/fm$. This is the only parameter that will be used to adjust the model.

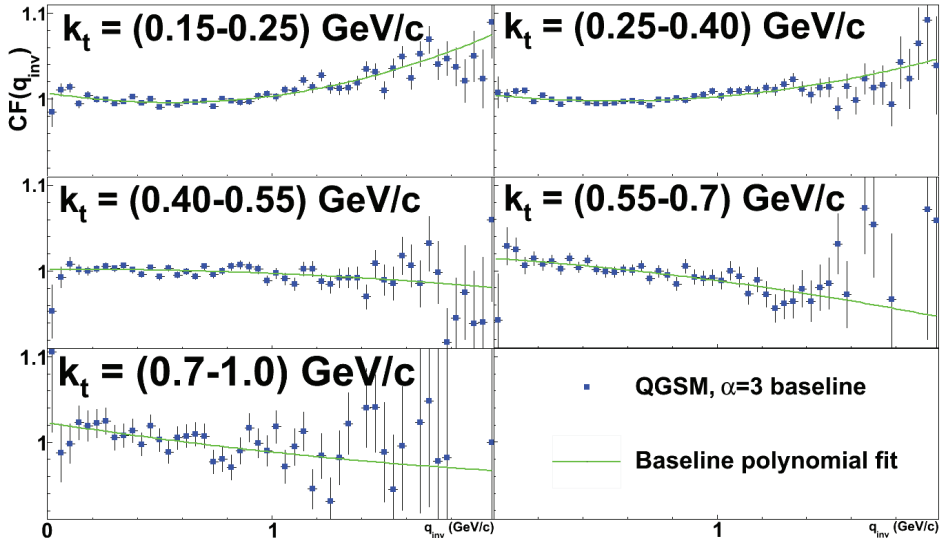

Figure 5.5: Calculated QGSM baseline for $900\ GeV$ pp collisions in five K_T bins with $\alpha = 3$

5.2.1 One-dimensional $\pi\pi$ correlations

The main theoretical background for identical particle correlations has been presented in section 3.1. In particular the methods described for extracting the correlation function from a microscopic model have been used. In order to replicate experimental procedure the mixed correlation functions were created by using particles from different events in the denominator. A test was made calculating the correlation functions with the weight ω set to unity to describe the background, and it was found that QGSM did not have any non-femtoscopic effects at low q_{inv} for the first two K_T-bins. Fits using a flat background were performed and the results were compared to the experimental findings at the STAR experiment at RHIC and the ALICE experiment at LHC.

The QGSM baseline was calculated by setting the weight $\omega = 1$ when creating the mixed CF, this turns off the quantum statistical effect and leaves only non-femtoscopic correlations. The baselines can be seen in Fig. 5.5. The baseline is flat at low q_{inv} for the two first K_T-bins and rising at high q_{inv}, this rise is due to the lack of energy-momentum conservation when we use particles from different events in our mixing procedure. For the higher K_T-bins a small dip can be observed at low q_{inv}, indicating a non-femtoscopic effect. At high q_{inv} the effects of low statistics can be seen, especially in the high K_T-bins. Differences in high q_{inv} bins may also arise from event-by-event fluctuations. The shape of the baseline is also determined by the choice of functional form, the second order polynomial chosen here will naturally dip or rise at high q_{inv} if given the opportunity by statistics or fluctuations.

The correlation functions are calculated for both 200 GeV and 900 GeV with flat baselines.

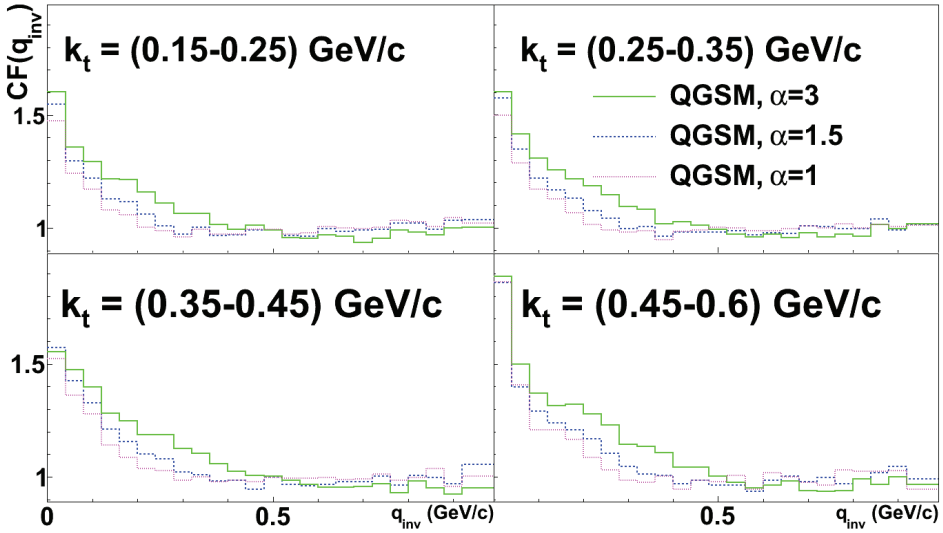

Figure 5.6: Calculated QGSM correlation functions for 200 GeV pp collisions in four K_T bins, for three different values of the scaling parameter α

Using the scaling parameter α we find the best fit to the experimental data for 200 GeV using $\alpha = 1.5$ and for 900 GeV using $\alpha = 3.0$. The effect of the scaling parameter on the correlation function can be seen in Fig. 5.6 (200 GeV) and Fig. 5.7 (900 GeV).

As expected a larger scaling parameter (shorter formation time) led to a wider correlation function (smaller source). The QGSM data with the chosen scaling parameters was then put through a fitting procedure using Eq. 3.19 as the fitting function, disregarding the Coulomb contribution ($K(q_{inv}) = 0$) and using a flat baseline ($B(q_{inv}) = 1$). This fitting procedure is a reproduction of the experimental fitting procedures used in STAR and ALICE, however as seen in the result of the fits in Figs. 5.8 and 5.9 the single Gaussian fit is unable to describe the low q_{inv} peak in the correlation function. In order to get a better description of the correlation function in the fit one may use the so called "double-Gaussian" fitting function [109]:

$$CF_{double}(q_{inv}) = \left[1 + \lambda_1 \exp(-R^2_{inv,1} q^2_{inv}) + \lambda_2 \exp(-R^2_{inv,2} q^2_{inv})\right] D(q_{inv}), \qquad (5.3)$$

where the parameters $R_{inv,(1,2)}$ and $\lambda_{(1,2)}$ describe the sizes and correlation strengths of two different sources 1 and 2. These two sources can represent direct particles and particles produced in resonance decays. As these two groups of particles are formed on average at very different times and at different source sizes it makes sense to separate their contributions in the correlation function. As seen in Figs. 5.8 and 5.9 the double Gaussian fit separates the correlation function into a wide Gaussian representing the small size of the source of the direct particles and a narrow Gaussian representing the large size halo of the particles produced from resonance decays, the

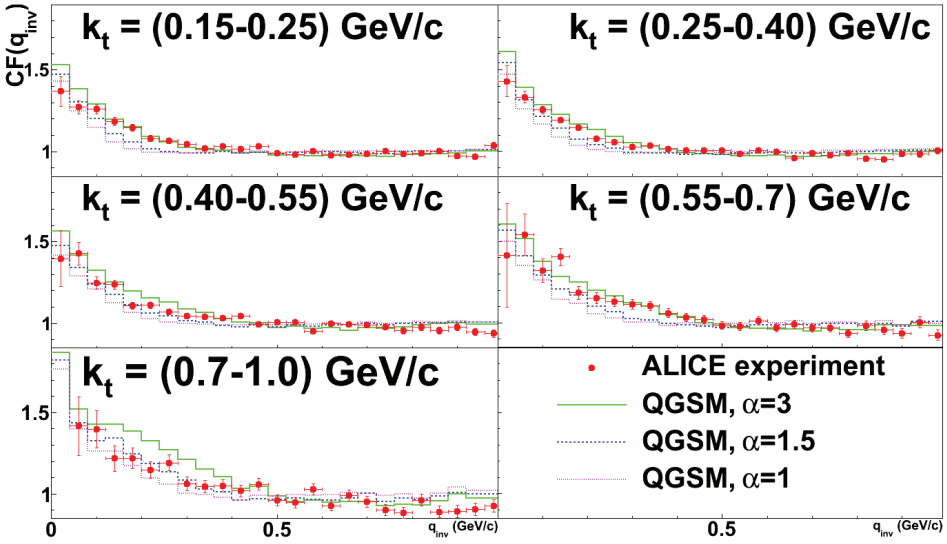

Figure 5.7: Calculated QGSM correlation functions for 900 GeV pp collisions in five K_T bins, for three different values of the scaling parameter α, compared with ALICE experimental data [80]

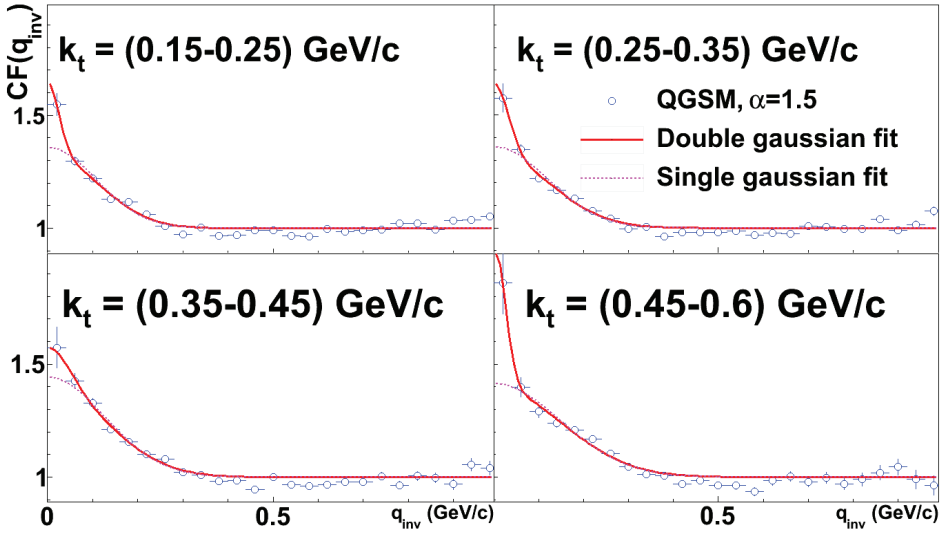

Figure 5.8: Single and double Gaussian fits of QGSM correlation functions for 200 GeV pp collisions in four K_T bins with $\alpha = 1.5$

two Gaussians represent two different regions of homogeneity.

The results of the fit for all K_T bins can then be plotted and compared with the experimental results in Fig 5.10. A clear drop in source size with rising K_T can be seen. This is in contrast to the reported ALICE results in [80], where the correlation radii is found to be independent of K_T if a PHOJET/PYTHIA baseline is chosen. The conclusion in the ALICE paper is based on the assumption that PHOJET and PYTHIA correctly describe the non-femtoscopic effects at low-q_{inv}. One possible source for these effects are the so-called mini-jets. As these non-femtoscopic correlations in PHOJET/PYTHIA become evident at larger K_T, they are the source of the K_T independence in the ALICE analysis. However the rather successful description of the ALICE points by QGSM suggests that there is no room for non-femtoscopic correlations at low q_{inv} up to $K_T < 0.7 GeV/c$.

To understand the origin of the K_T-dependence in experiment it might be helpful to study the origin of this dependence in QGSM. As seen in Fig. 5.4 there is a strong $p_x - x$ correlation inherent to the QGSM model. Since only particles with close momenta (low q_{inv}) contribute to the correlation effect, these pairs also come from nearby space regions of the source. The correlations measure not the size of the whole source, but the size of the regions which emit particles of a given momenta, the region of homogeneity. Particles with high K_T have large momenta and fly away from each other much quicker than particle pairs with small K_T, so in order to be correlated they have to be very close in coordinate space. This gives rise to the smaller sizes at higher K_T.

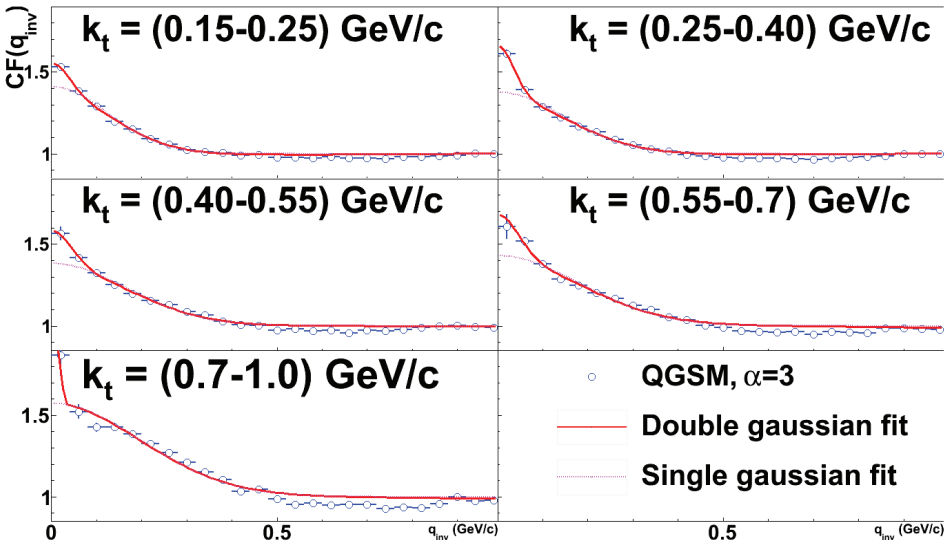

Figure 5.9: Single and double Gaussian fits of QGSM correlation functions for 900 GeV pp collisions in five K_T bins with $\alpha = 3.0$.

A second factor influencing the coordinate distributions is the ratio of direct pions to pions produced from resonance decay. The fraction of pions which are direct or from resonance decay changes with the collision energy and is presented in Table 5.1.

The three main resonance contributions in the model are $\rho^{0,+}$ which is short lived, ω and $K^{*,+}$ which are long lived. Decays from these two last resonances are the main origin of the low q_{inv} peak in the correlation function, and contributes to a larger correlation radii. As seen in Fig. 5.11 the long lived resonances have a decreased relative yield at higher K_T, a second effect in the model that contributes to a K_T-dependence.

Keeping in mind that the contributions from long lived resonances creates an exponential tail in the pion emission function which translates into the non-Gaussian peak in the correlation

	l^* (fm)	200 GeV	900 GeV
Direct π^+	-	46.9%	37.5%
π^+ from $\rho^{0,+} \to \pi^{-,0}\pi^+$	3.3	37.1%	40.7%
π^+ from $\omega \to \pi^0\pi^-\pi^+$	28.1	11.2%	15.9%
π^+ from $K^{*,+}(\bar{K^{*,0}}) \to K\pi^+$	8.0	4.2 %	5.5 %

Table 5.1: The fraction of pions from decay of main resonance species in QGSM and the path length l^* of these states.

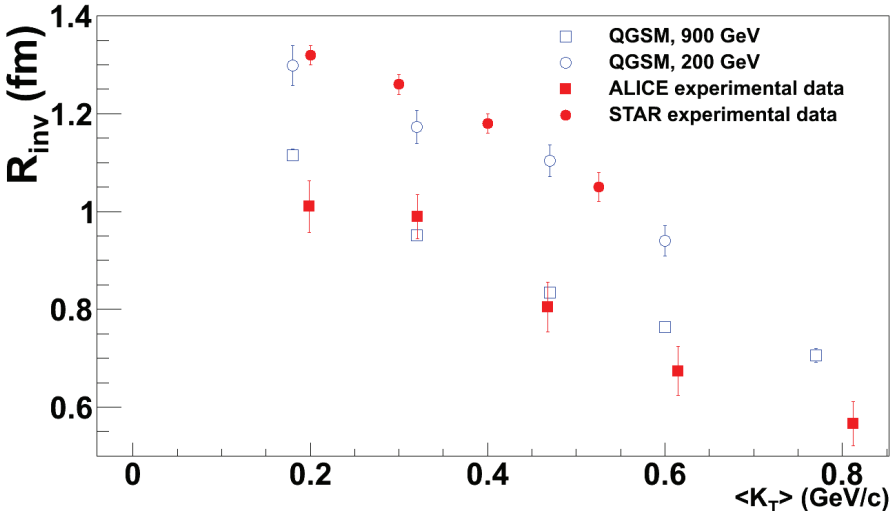

Figure 5.10: One-dimensional $\pi^+\pi^+$ correlation radii as functions of K_T in pp-collisions at $\sqrt{s} = 200\ GeV$ and $\sqrt{s} = 900\ GeV$, compared with STAR [76] and ALICE [80] experimental data. Both model results and experimental data are obtained from a fit using a flat baseline.

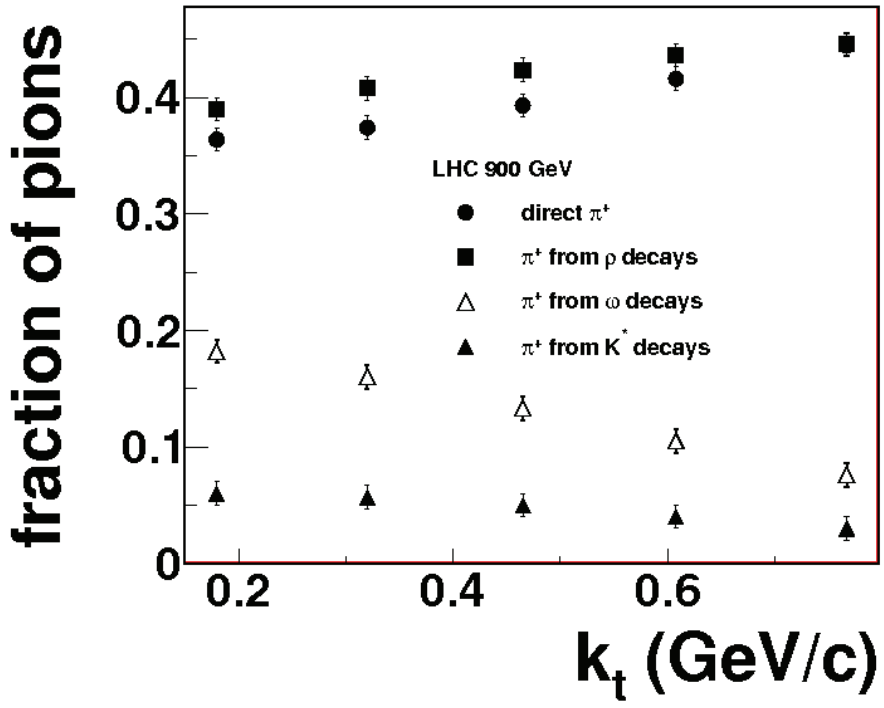

Figure 5.11: Contribution of direct pions and pions produced from resonances as a function of K_T, given in percentages.

Table 5.2: Parameters R_{inv} extracted from $\sqrt{s} = 900\ GeV$ pp collisions in QGSM by using different fitting strategies as described above: The selected transverse momentum intervals are $0.1 \leq K_T \leq 0.25\,\text{GeV}/c$ (KT1), $0.4 \leq K_T \leq 0.55\,\text{GeV}/c$ (KT3) and $0.7 \leq K_T \leq 1.0\,\text{GeV}/c$ (KT5).

Method	$R_{inv1(2)}$ (fm)		
	KT1	KT3	KT5
1	1.00	0.77	0.66
2	1.26	0.84	0.71
3	1.10	0.84	0.71
4	1.23	0.81	0.71
	5.04	3.26	13.97
5	1.05	0.81	0.71
	3.61	3.25	13.83

function, it is useful to study further the effects of different fitting methods. In total five different methods were employed to fit the same correlation function:

1. "ideal" CF is fitted to the single Gaussian with $B(q_{inv}) = 1$
2. "mixed" CF is fitted to the single Gaussian with $B(q_{inv}) = 1$
3. "mixed" CF is fitted to the single Gaussian with $B(q_{inv}) = a + bq_{inv} + cq_{inv}^2$
4. "mixed" CF is fitted to the double Gaussian with $B(q_{inv}) = 1$
5. "mixed" CF is fitted to the double Gaussian with $B(q_{inv}) = a + bq_{inv} + cq_{inv}^2$.

Here the single Gaussian refers to Eq. 3.20 and the double Gaussian refers to Eq. 5.3, in both cases with $K(q_{inv}) = 0$. The results of these fits are presented in Table 5.2. The "ideal" CF fit gives a smaller correlation radius for all three K_T bins compared to the "mixed" correlation function. The effect of using a polynomial baseline is mainly a small drop in the correlation radius in the smallest K_T-bin. For both double Gaussian methods the separation can be seen between one Gaussian for the direct pions and pions from short lived resonances on one hand and another Gaussian for the pions produced from long lived resonances. It can also be seen however that the Gaussian representing the direct pions gives a correlation radius corresponding to the single Gaussian fit using the same baseline. The single Gaussian fit mainly represents the direct pions and pions coming from short lived resonances, with only a small contribution from pions produced from long lived resonances.

It is interesting to compare the results of the fits of the correlation functions with the freeze-out pictures shown in Section 5.1. In Figs. 5.1, 5.2 and 5.3 the important role of long-lived resonances can be seen. These resonances freeze-out much later in the expansion, and therefore at larger distance from the centre. It is the effects of these long-lived resonances which can be seen in the low q_{inv} peak of the correlation function, and manifests as a large second radius in the two Gaussian fitting approach.

5.2.2 3-dimensional $\pi\pi$ correlations

Three-dimensional correlation functions have also been constructed for both $\sqrt{s} = 200\ GeV$ and $\sqrt{s} = 900\ GeV$. The full 3D correlation function is constructed using the same form $CF(q) = \dfrac{N(q,\omega)}{N(q,1)}$, but with both numerator and denominator as three-dimensional histograms in the "out-side-long" directions. We then use the fitting function in the form of Eq. 3.14, again disregarding the Coulomb contribution $K(q_{inv}) = 0$. The same QGSM data is used with the same values of the scaling parameter for $\sqrt{s} = 200\ GeV$ ($\alpha = 1.5$) and $\sqrt{s} = 900\ GeV$ ($\alpha = 3.0$). The presented figures of the 3D correlation functions in Figs. 5.12 and 5.13 are the slices in each direction (i.e. in the "out" direction $q_{side} \approx 0$ and $q_{long} \approx 0$).

It should be noted that the gaps that can be seen in the correlation function, especially in the "out" direction, are present due to kinematical restrictions of the Cartesian coordinate system employed. The difficulty of a full 3D fit should also be stressed, the full correlation function is a three-dimensional histogram which is fitted with a 3D fitting function. Any deviation of the correlation function from the theoretical Gaussian becomes more pronounced, and more difficult to compensate for.

The results of these fits can be seen in Figs. 5.14 and 5.15. The model gives a fair description of the experimental data, and especially manages to reproduce the K_T dependence of R_{long} at $\sqrt{s} = 900\ GeV$. The model overpredicts the R_{out} value at low K_T, and comes closer to the experimental value at higher K_T. This is the opposite behaviour of what you might expect from looking at just Figs. 5.12 and 5.13. The model reproduces the flat behaviour of R_{side} over k_T, but slightly overpredicts the value. The R_{long} dependence of the model rises incorrectly at high K_T for $\sqrt{s} = 200\,GeV$, but gives a very good description of the experimental data at $\sqrt{s} = 900\,GeV$. The λ value of the model rises a bit too sharply for STAR energies, and rises even sharper at LHC energies, but the absence of ALICE λ values makes a comparison inconclusive.

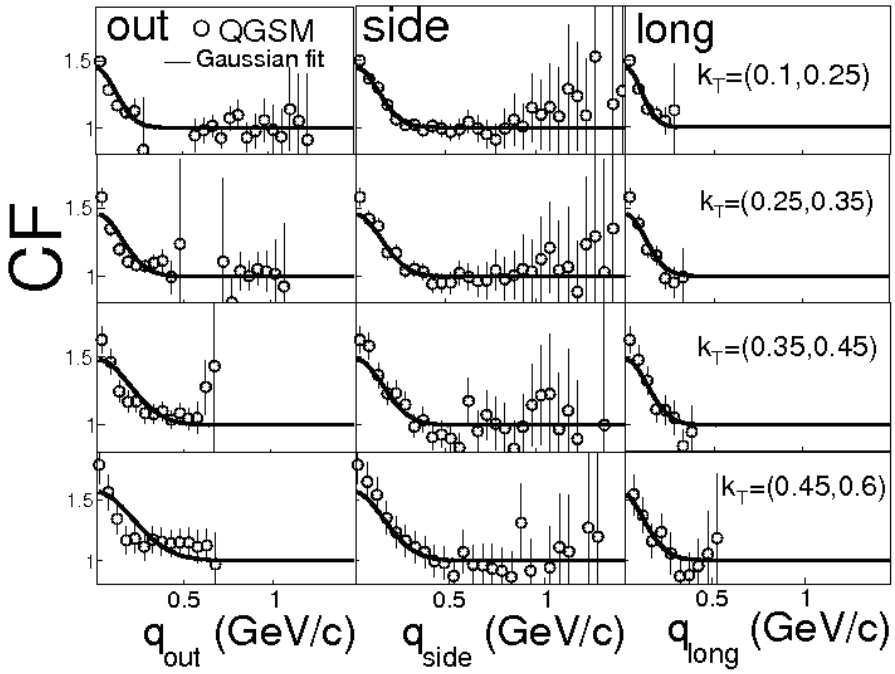

Figure 5.12: Fit of the 3D correlation function projected onto the "out-side-long" directions for $\sqrt{s} = 200\ GeV$ pp collisions in the QGSM model

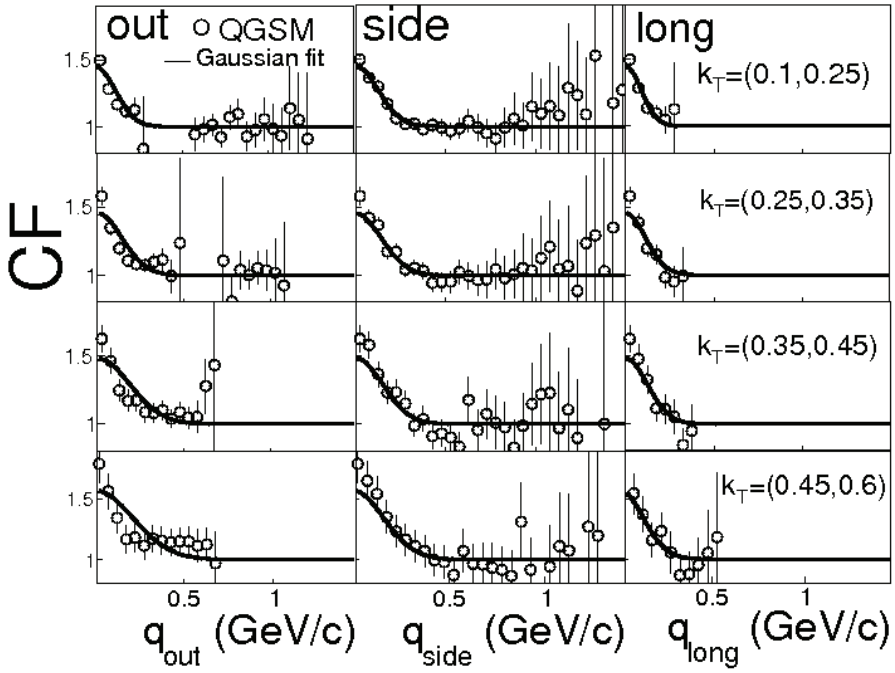

Figure 5.13: Fit of the 3D correlation function projected onto the "out-side-long" directions for $\sqrt{s} = 900\ GeV$ pp collisions in the QGSM model

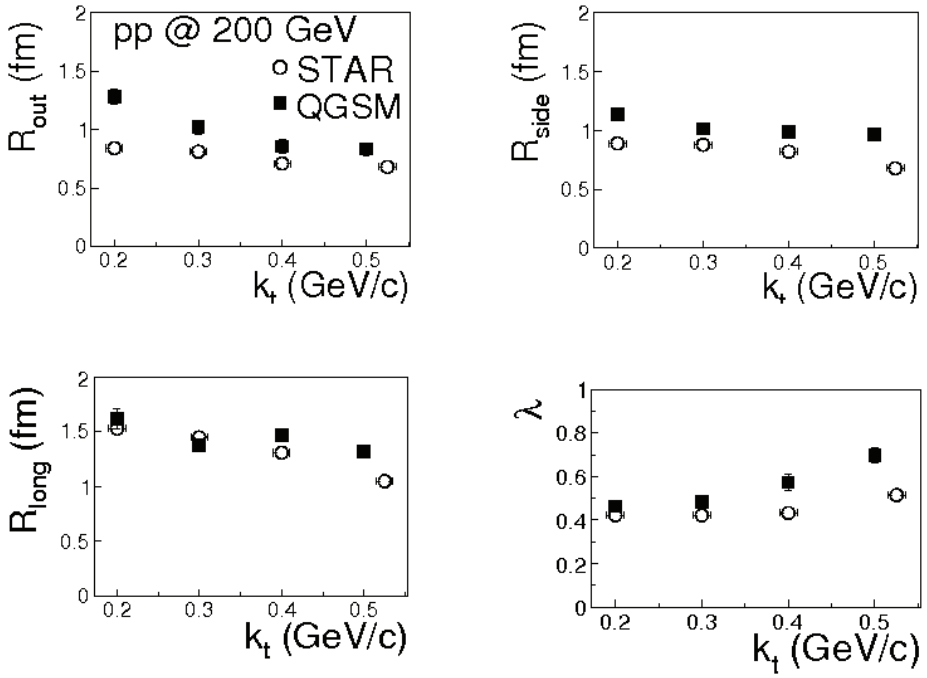

Figure 5.14: 3D correlation radii for $\sqrt{s} = 200\ GeV$ pp collisions in the QGSM model compared with STAR experimental data [76].

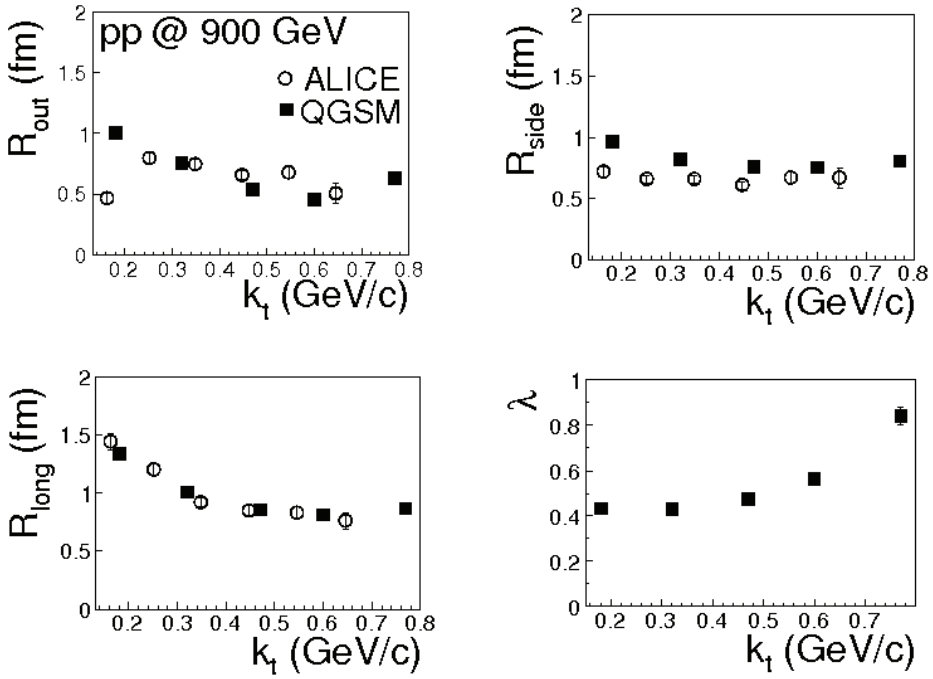

Figure 5.15: 3D correlation radii for $\sqrt{s} = 900\ GeV$ pp collisions in the QGSM model compared with ALICE experimental data [80]

Chapter 6

πK correlations in ALICE proton-proton collisions

Studies of πK correlations have been performed earlier in heavy-ion collisions [110], but due to lack of high statistics and good kaon identification it has never been possible to do it before in proton-proton collisions. However for proton-proton collisions at LHC energies high multiplicities were expected and have been observed [15]. In addition the PID capabilities of the ALICE detector makes it ideal for the study of non-identical particle correlations. A study of πK correlations in ALICE pp collisions is therefore not just interesting in terms of physics results, but it will also require the development of new analysis methods.

In this thesis we will focus on two areas of the analysis. First, because particle identification is very important, two methods for pion and kaon identification using the TPC and TOF will be introduced. Secondly, the fitting procedure of the calculated correlation functions will be looked at in detail, with several different methods tested. Finally conclusions will be drawn regarding the feasibility of using the different fitting methods tested.

6.1 Event selection

Analysis have been performed on pp collision data at $7\ TeV$ taken by the ALICE experiment in 2010. Only minimum bias events have been selected. Approximately $95M$ events were analysed from runs in LHC10b and LHC10c.

The reconstruction vertex have been demanded to be within $10\ cm$ of the centre of TPC along the beam direction. The data were analysed in 3 uncorrected charged particle multiplicity bins: (2-11), (12-22) and (23-140). The following single track selection conditions were used:

- Pseudorapidity cut: $|\eta| < 1.0$.
- Transverse momentum cut: $0.15 < p_T < 1.2\ GeV/c$.
- Accept only well reconstructed tracks: at least 70 out of maximum 159 points in the TPC.

- The distance of particle trajectory to the primary vertex should be less than $0.2\ cm$ in the transverse plane and less than $0.25\ cm$ in the beam direction.
- PID cuts for pions or kaons.

The following two-track selection cuts were used:

- Pairs that share more than 5% of clusters in the TPC are rejected.
- Pairs with $M_{ee} < 0.01\ GeV$ and $\Delta\theta_{ee} < 0.01\ rad$ are removed (anti γ-conversion cut).

6.2 Particle identification

Good particle identification is very important for the calculation of non-identical particle correlations. While pions are produced so abundantly that one can accept a lower efficiency, for kaons efficiency is very important and for both species a high purity is essential.

The ALICE detector provides a number of possibilities for particle identification. In this thesis we will employ data from the TPC and TOF detectors. The output from the TPC is the dE/dx vs momentum plot (Fig. 6.1). The particle most probable energy loss per unit of path length (dE/dx) is linked to its velocity β through the Bethe-Bloch formula:

$$-\frac{dE}{dx} = \frac{4\pi N_e^4}{m_e c^2}\frac{1}{\beta^2} z^2 \left(\ln \frac{2m_e c^2}{I}\beta^2\gamma^2 - \beta^2 - \frac{\delta(\beta)}{2} \right) \tag{6.1}$$

where N_e is the number density of electrons in the travelled material, z is the charge of the particle, $m_e c^2$ is the rest energy of an electron, β is the velocity of the particle and $\gamma = \frac{1}{\sqrt{1-\beta^2}}$. I is the mean excitation energy of the detector material, and $\delta(\beta)$ is the relativistic medium polarisation.

The Bethe-Bloch formula can be rewritten as:

$$\left\langle \frac{dE}{dx} \right\rangle = \frac{C_1}{\beta^2}\left(\ln(C_2\beta^2\gamma^2) - \beta^2 + C_3 \right) \tag{6.2}$$

where C_1, C_2 and C_3 are detector specific constants. Plotting $\langle dE/dx \rangle$ versus momentum gives us information about the mass of the particle, and therefore also its identity [46]. For low momenta particles it is possible to identify particles with the TPC alone, but at higher momenta the $\langle dE/dx \rangle$ versus p distributions for different particles overlap and we need additional information, from e.g. the TOF.

The main information from the TOF is the velocity vs momentum plot given in Fig. 6.2. As seen in the figure, we have separate particle lines for pions, kaons and protons. Here the overlap occurs mostly for particles with β close to unity. In order to identify a particle one then has to get both TPC and TOF information and use some method to decide whether it is close enough to the particle lines in both diagrams. Two methods have been tried: the simple contour method and the so-called "number of sigma" method. The first method has the advantages of being independent

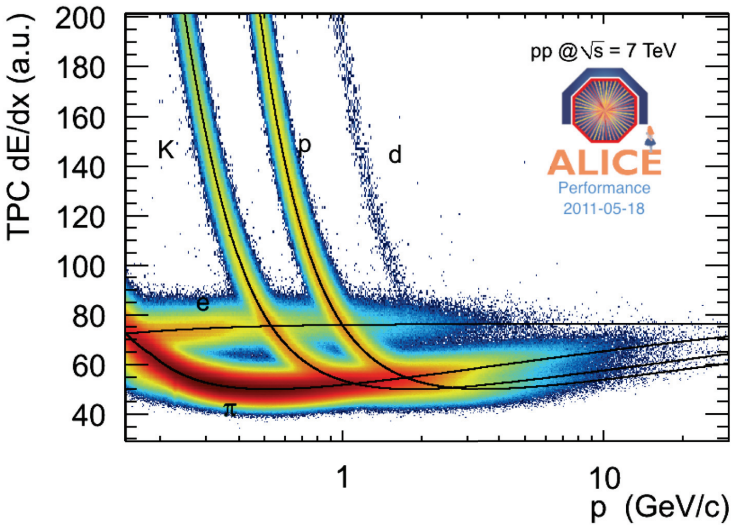

Figure 6.1: Example of a $\frac{dE}{dx}$ vs momentum plot from the TPC detector.

of the accuracy of the Bethe-Bloch formula determination and has a simple visual verification. It can be used in combination with the n-sigma method which uses information about the number of standard deviations of the Bethe-Bloch $\left\langle \frac{dE}{dx} \right\rangle$ for TPC or Δt for TOF from the calculated values for the given type of particle.

6.2.1 Contour method

The contour method starts with the simple idea that it is possible to outline the different particle lines in the TPC and TOF plots by hand. If one parametrises this outline it is possible to decide whether a particle is within the particle line by comparing with the parametrisation. The outline is created by first plotting the uncut output from the TPC and TOF detectors and recognising the particle lines by eye. The parametrisation is then created for different momentum/velocity ranges. This means that the limit between what is considered a pion or kaon or not is rather arbitrary, which is why this can be considered as a rough method.

In addition to using a parametrisation of the outline one must also decide the momentum ranges that are used for the two detectors. The results for passed pions and kaons in TPC and TOF with the contour method are shown in Fig. 6.3. The pion and kaon lines can be restored, but the roughness of the method means that we lose many particles. This can be seen in the sharp top edge of the pion plot in the TPC, as well as the different cuts used for different p_T ranges for kaon in the TPC.

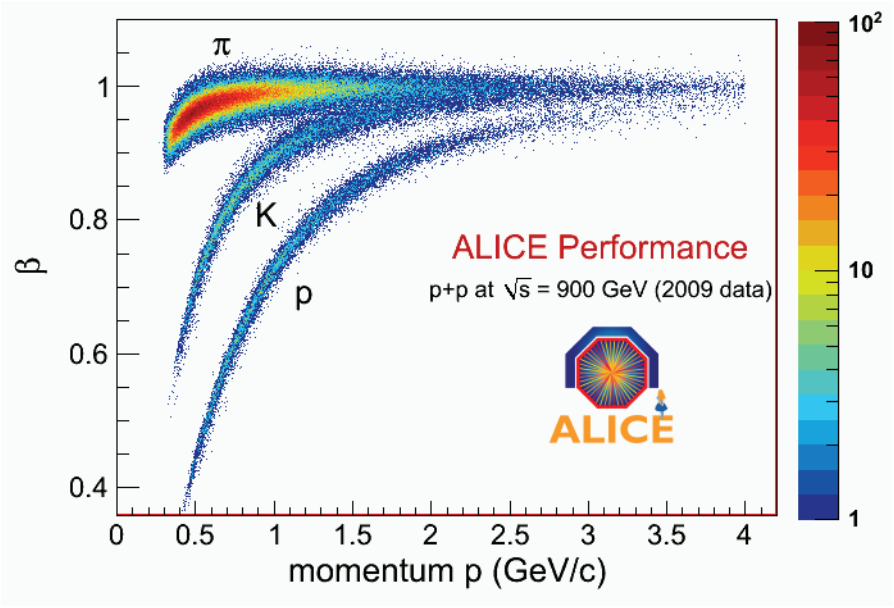

Figure 6.2: Example of a velocity vs momentum plot from the TOF detector.

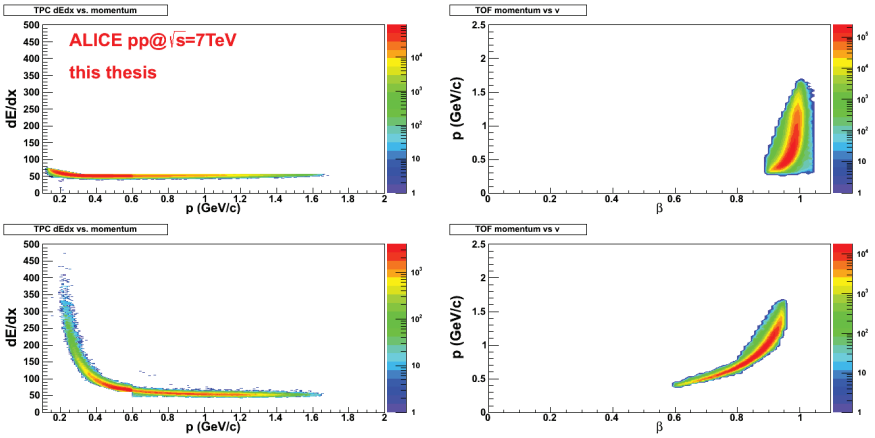

Figure 6.3: Pions (upper row) and kaons (lower roe) identified with the contour method using data from the TPC (left column) and from the TOF (right column).

cut	TOF PID not available		TOF PID is available	
Kaon N_σ	$p < 0.35\ GeV/c$	$\lvert N_{\sigma,TPC}\rvert < 2$	$p < 1.5\ GeV/c$	$\lvert N_{\sigma,TPC}\rvert < 5$ $\lvert N_{\sigma,TOF}\rvert < 3$
	$0.35 < p < 0.6\ GeV/c$	$\lvert N_{\sigma,TPC}\rvert < 2$	$p > 1.5\ GeV/c$	$\lvert N_{\sigma,TOF}\rvert < 2$
Pion N_σ	$p < 0.35\ GeV/c$	$\lvert N_{\sigma,TPC}\rvert < 5$	$p < 1.5\ GeV/c$	$\lvert N_{\sigma,TPC}\rvert < 5$ $\lvert N_{\sigma,TOF}\rvert < 3$
	$0.35 < p < 0.5\ GeV/c$	$\lvert N_{\sigma,TPC}\rvert < 3$	$p > 1.5\ GeV/c$	$\lvert N_{\sigma,TOF}\rvert < 2$
	$p > 0.5\ GeV/c$	$\lvert N_{\sigma,TPC}\rvert < 2$		

Table 6.1: Number of sigmas for TPC and TOF detectors for pions and kaons

6.2.2 Number of Sigma method

The particle most probable energy loss calculated with the Bethe-Bloch formula (Eq. 6.1) is parametrised for the TPC with Eq. 6.2. For the analysis presented in this thesis, pions and kaons were selected by requiring the deviation of the specific $\left\langle \frac{dE}{dx} \right\rangle$ to be within N_σ standard deviations from the pion/kaon Bethe-Bloch values calculated with Eq. 6.2. These N_σ values depend on the registration conditions, the existence or non-existence of a TOF signal, and momentum range. These conditions with N_σ values are listed in Table 6.1.

A time of flight measurement is the measurement of a time interval: $\Delta t = t_{TOF} - t_0$. The number of standard deviations are determined by:

$$N_{\sigma,TOF} = \frac{(t_{hit} - t_0) - t_{expected}(p, m, c)}{\sigma_{PID,TOF}} \tag{6.3}$$

where t_{hit} is the time measurement made by the TOF detector, and t_0 is the zero time for the event measured by the T0 detector, or estimated using the TOF detector itself. $t_{expected}$ is computed during momentum construction using the different masses hypothesis (π, K, p).

$$\begin{aligned} \sigma_{PID,TOF} &= \sqrt{\sigma^2_{TOF} + \sigma^2_{t_0} + \sigma^2_{tracking}} \\ \sigma^2_{TOF} &= \sigma^2_{MRPC} + \sigma^2_{electronics} + (other\ contributions) \end{aligned} \tag{6.4}$$

where $\sigma^2_{t_0}$ is equal to σ_{T0} when the T0 detector is available, or can be determined using TOF tracks. σ_{t_0} can vary greatly event by event. $\sigma_{tracking}$ is the resolution of tracking.

Pions and kaons selected with the number of sigma method are shown in Fig. 6.5. This method gives smoother pion and kaon lines compared with the contour method, and is also better rooted in the physics of the detector. The purity of the kaons is high, except for a small region in momentum of about 20% electron contamination, this is presented in Fig. 6.4.

The use of two different methods gives the opportunity to study the impact of the method on the correlation functions. If for example there is a bad calibration, the Bethe-Bloch lines might be shifted, and the simpler contour method would give a better result.

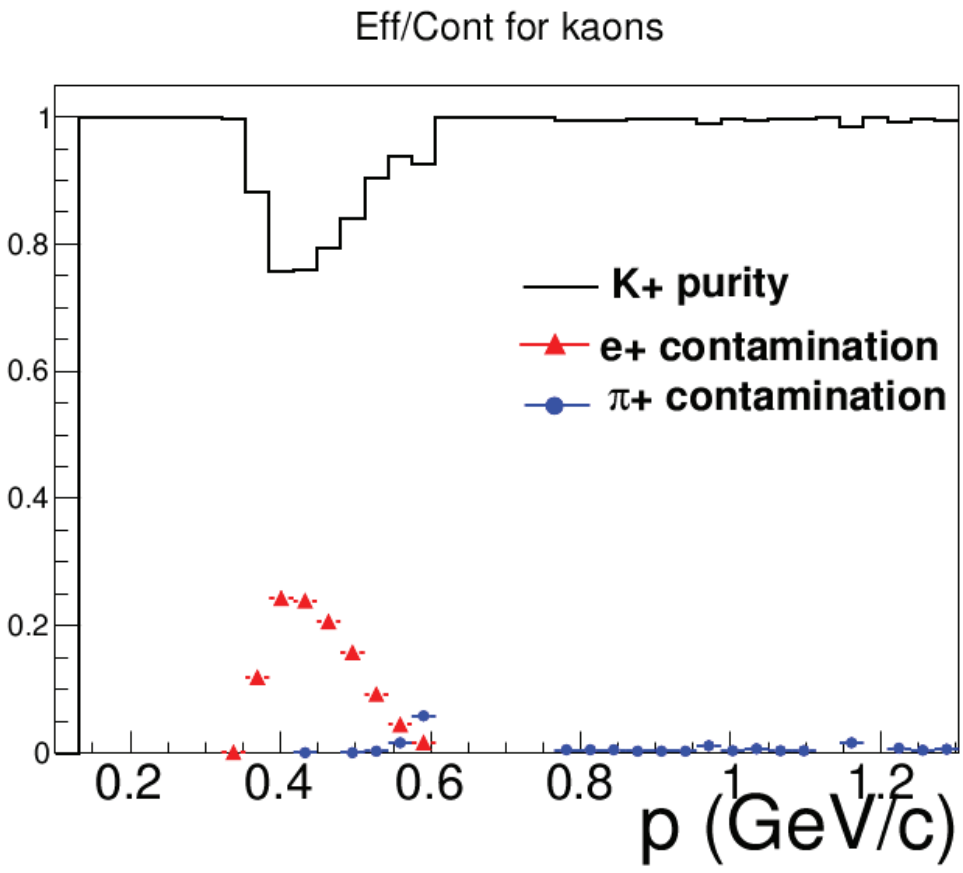

Figure 6.4: Purity of kaons with the number of sigma method as a function of momentum.

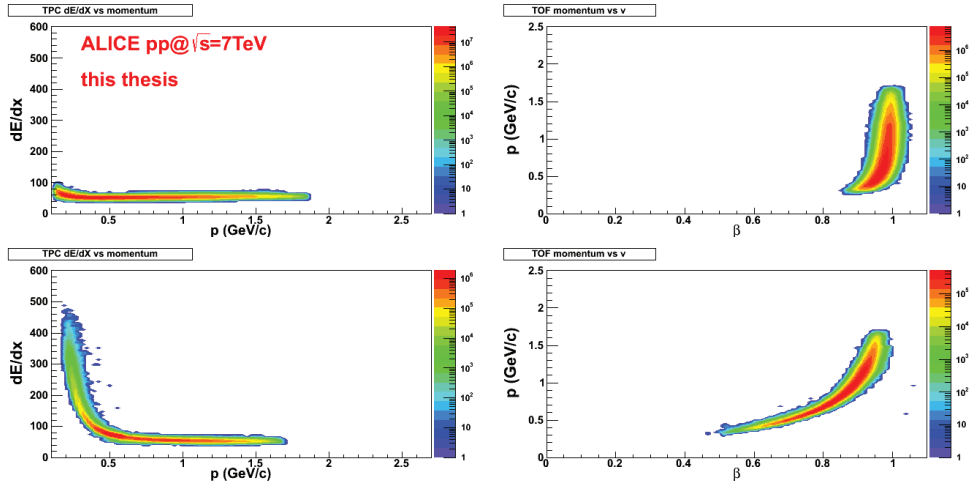

Figure 6.5: Pions (upper row) and kaons (lower row) identified with the number of sigma method using data from the TPC (left column) and from the TOF (right column).

6.3 Correlation functions

The experimental correlation function is a function of the relative pair momentum k^* (Eq. 3.23) and is constructed as $CF = \frac{N(k^*)}{D(k^*)}$, where $N(k^*)$ is the k^* distribution for particle pairs from same events and $D(k^*)$ is for particle pairs from mixed events.

The correlation functions will be created for all four πK pair types (π^+K^+, π^+K^-, π^-K^+, π^-K^-), and for three multiplicity bins ($M \leq 11$, $11 < M \leq 22$, $M > 22$).

6.3.1 Correlation functions from experiment

Using the Number of Sigma method for particle identification, correlation functions have been calculated from experimental data separately for the four possible pair combinations. The unnormalised "raw" correlation functions are presented in Fig. 6.6. A strong γ-cut was implemented on the PID. This cut was adjusted using Monte Carlo calculations, as explained in section 6.3.2.

Several features of the correlation functions are immediately obvious. A peak appears at about $k^* = 0.3\ GeV/c$. This peak originates from the decay of the K^* resonance into either π^+K^- or π^-K^+ pairs. The position of the peak corresponds to the mass of the resonance, and is well understood.

At low k^* another peak can be seen. This peak originates mainly from the femtoscopic correlation effect that we are interested in. The peak shows positive correlations for opposite sign pairs, and negative correlations for same sign pairs. This is as expected as the correlations stem

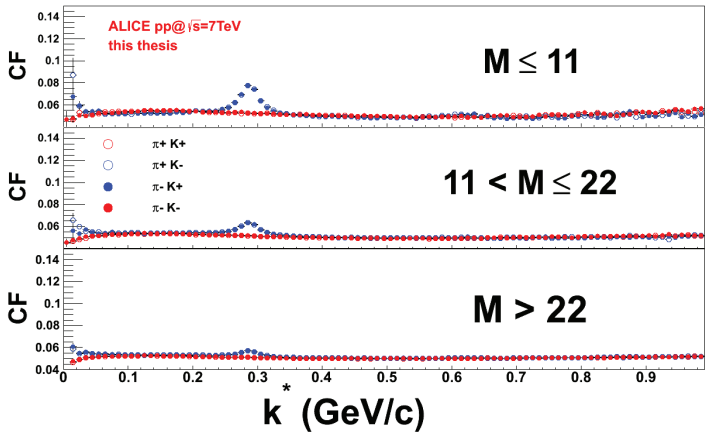

Figure 6.6: Raw πK correlation function obtained from the ALICE experiment in minimum bias pp collisions at $\sqrt{s} = 7\ TeV$ for three multiplicity bins.

mainly from Coulomb interactions. We can also see that apart from the low-k^* correlation peak and the resonance peak, the correlation functions are basically the same for all four pair types. This is especially true for the pair types with either same or opposite charges. The similarity of the correlation functions implies that the background is the same for all pair types. This background has a rather complex behaviour, which needs to be taken into account in the fitting process.

At high k^* a small multiplicity effect can be seen, as the lowest multiplicity bin has slightly larger variations and errors. Finally the normalisation of the correlation functions will be done as a part of the fitting procedure.

6.3.2 Correlation functions from PYTHIA

Correlation functions are created both from simulated PYTHIA [111] data and from experimental data. In PYTHIA there are no final state interactions (FSI), so any correlations appearing will be from other origins. About $50M$ PYTHIA6 Perugia-0 event have been used. In Fig. 6.7 we can see the calculated correlation functions from PYTHIA in three multiplicity bins.

Two interesting features can be seen from this figure. First, the K^* peak is evident at $k^* = 0.3\ GeV/c$ for all three multiplicities. Secondly, a peak can be seen close to $k^* = 0$. Since there are no FSI in PYTHIA the appearance of this peak is due to other correlations. This source origin can be understood if we include a cut removing photons decaying into e^+e^-. The cut is performed by removing particles with $M_{eff,e^+e^-} < 0.01$ and $\theta_{e^+e^-} < 0.01$. As seen in Fig. 6.8 the peak disappears when the cut is implemented.

The close to zero peak in Fig. 6.7 originates from either one or two misidentified electrons in the πK pairs. It is clear that a strong γ-cut is important in order to remove misidentified electrons

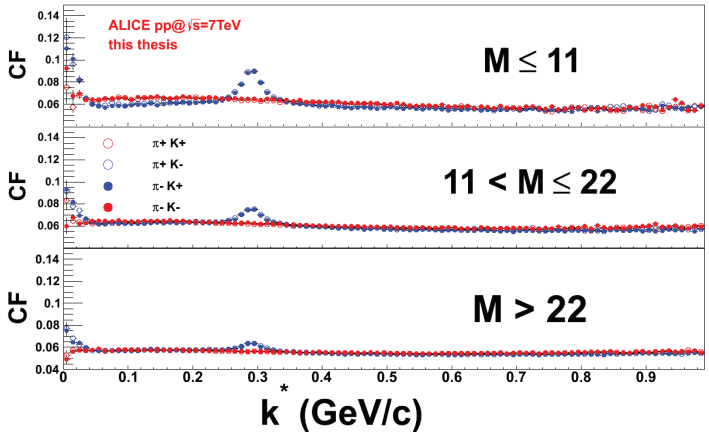

Figure 6.7: πK correlation function calculated from PYTHIA6 Perugia-0 in minimum bias pp collisions at $\sqrt{s} = 7\ TeV$ for three multiplicity bins.

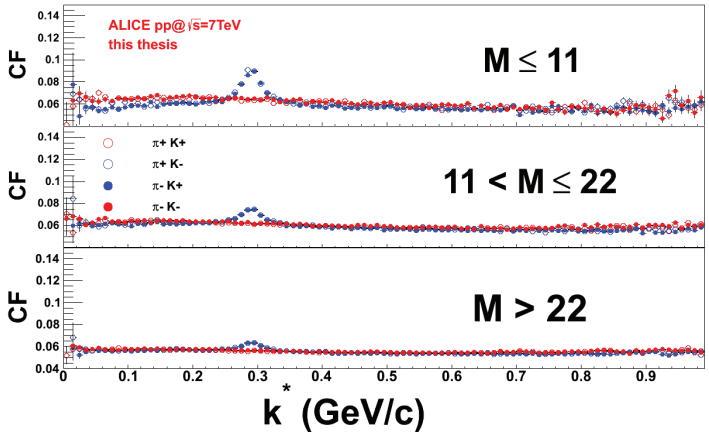

Figure 6.8: πK correlation function calculated from PYTHIA6 Perugia-0 in minimum bias pp collisions at $\sqrt{s} = 7\ TeV$ with a γ-cut for three multiplicity bins

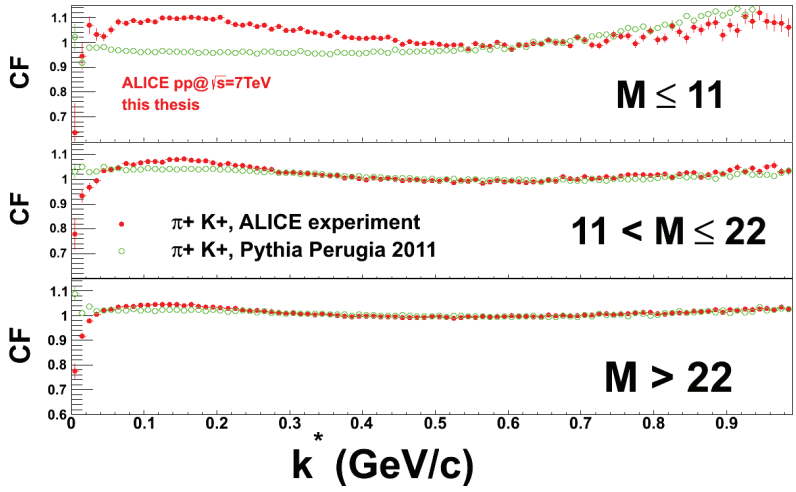

Figure 6.9: Comparison of correlation functions from PYTHIA Perugia 2011 with ALICE experimental data for minimum bias pp collisions at $\sqrt{s} = 7\ TeV$ for three multiplicity bins.

from out pairs, and this cut will be implemented in the analysis of the experimental data.

PYTHIA Perugia 2011 [112] is a newer version which have been successfully used to describe the correlations of both $\pi\pi$ and KK, therefore it is a good candidate for calculating πK correlations as well. About $400M$ pp $7\ TeV$ minimum bias events have been calculated with PYTHIA Perugia 2011. Since there are no FSI in PYTHIA any correlation functions calculated will show the non-femtoscopic background only. The correlation function is calculated using the mixing procedure described in section 3.1 for microscopic models, with a weight $\omega = 1$ for the numerator. The calculated PYTHIA Perugia 2011 correlation functions are then compared to the experimental data. The femtoscopic effect should only be dominant at low k^*, meaning that if PYTHIA gives a good description of the background the experimental and simulated correlation functions should coincide at high k^*. As seen in Fig. 6.9 this is not the case.

The model description is best at the highest multiplicity bin, with a large discrepancy at the lowest bin. The difference is biggest in the $k^* = (0.1, 0.2)$ region, where the interplay between the background and the femtoscopy effect is strongest. There are also some problems at the smallest k^* bins, probably due to low statistics. An interesting behaviour of the baseline in the model is that it is flat at low q_{inv}, indicating that we should seek of a representation of the baseline that is also flat at low q_{inv}

6.4 Fitting strategy

In order to extract the femtoscopic sizes of the system a fit of the correlation function is necessary. However, first one must decide on a strategy for the fitting process. In particular it is important to properly describe the non-femtoscopic background. We can write our fitting function as:

$$f(k^*) = N \cdot F(k^*) \cdot B(k^*) \tag{6.5}$$

Here N is a normalisation constant, $F(k^*)$ is a function describing the femtoscopic effect at low k^* and $B(k^*)$ is a function describing the non-femtoscopic background. Our main interest at this point is background extraction, so the femtoscopic effect will be described by a very approximate function, this will exclude the Coulomb effect from consideration. The Coulomb forces can be described using the Gamow-factor $A(\eta)$ given in Eq. 3.29. However in order to introduce a dependence on the radius the expression slightly changed:

$$F(k^*) = 1 + \lambda \frac{2\pi}{R \cdot k^* a} \left[\exp\left(\frac{2\pi}{R \cdot k^* a} \right) - 1 \right]^{-1} \tag{6.6}$$

where λ represents the strength of the correlation and R is the radius. We will focus first on the background function B. In previous ALICE femtoscopic publications the background has been described by using PYTHIA. Seeing as there are no femtoscopic effects in PYTHIA, any deviations from unity in the calculated PYTHIA correlation functions were taken as non-femtoscopic. The background function was chosen in the form of a polynomial and fitted to the PYTHIA correlation function. The fitting parameters of the polynomial were then fixed, and the same polynomial was used as the background when fitting to experimental data. This method was used mainly because of the problems of extracting a pure experimental background. However, this method introduces a model dependence into the results. Therefore it is preferable to extract the background directly from experiment if possible.

Such a possibility exists for πK correlations. As previously observed in Fig. 6.6 all four pair types seem to have the same non-femtoscopic background. This gives us a hint that it might be possible to use a simultaneous fitting procedure. In such a procedure the correlation functions of all four pair types would be fit simultaneously, with the same fitting parameters for the background, but with different parameters for the femtoscopic effect. Since the femtoscopic effect is positive for opposite sign pairs and negative for same-sign pairs this should hopefully ensure that the background and the signal are disentangled. Once the background has been determined the correlation function can be divided on the fixed polynomial in order to obtain the pure femtoscopic effect.

In addition the fit also needs to take into account the resonance peaks for opposite-sign pairs. The equation that needs to be fitted then looks like:

$$Num(k^*) = N \cdot Den(k^*) \cdot F(k^*) \cdot B(k^*) + B_{BW}(M_{inv}) \tag{6.7}$$

Here $Num(k^*)$ is the numerator of the correlation function, $Den(k^*)$ is the denominator of the correlation function and $B_{BW}(M_{inv})$ is a Breit-Wigner function that describes the resonance

peak for opposite-sign pairs and equals to zero for same-sign pairs. The invariant mass of the pair M_{inv} is calculated as:

$$M_{inv} = \frac{1}{\sqrt{2}}\Big[4(k^*)^2 + (m_\pi + m_K)^2 + (m_\pi - m_K)^2 + \sqrt{(4(k^*)^2 + (m_\pi + m_K)^2 + (m_\pi - m_K)^2)^2 - 4(m_\pi + m_K)^2(m_\pi - m_K)^2}\Big]^{1/2} \tag{6.8}$$

The choice of background function can have great impact on the fit. A natural choice is to use a polynomial, however due to physical restraints we want the background to have a zero derivative at $k^* = 0$: $\left(\frac{dB(k^*)}{dk^*}\right)_{k^*=0} = 0$. This can be achieved by putting the linear term equal to zero. We then have the background in the following form:

$$B(k^*) = 1 + \sum_{i=2}^{i=n} (k^*)^i c_i \tag{6.9}$$

Here n is the order of the polynomial chosen, and c_i is the constants used as fitting parameters. Other possible choices include using only even order terms in the series or the square root of the polynomial, but since there are no physical reasons to prefer one before the other the simplest type of polynomial is chosen.

6.4.1 Fitting same-sign and opposite-sign separately

The fitting method is first tested by fitting the two same-sign pairs and the two opposite-sign pairs separately. The correlation functions used in this test are for $k^*_{out} > 0$, CF^+_{out}. Eq. 6.7 is used for the fitting in both cases, with $B_{BW}(M_{inv})$ equal to zero for same-sign and as a Breit Wigner function for opposite-sign pairs. A simultaneous fit for π^+K^+ and π^-K^- is performed with polynomial background of order 4 to 7. As seen in Figs. 6.10, 6.11, 6.12 and 6.13 the fit is reasonably good already for $n = 4$ and becomes better with increasing n. However if we divide the correlation function on the obtained background (Figs. 6.14, 6.15, 6.16 and 6.17) we can see that the results depend heavily on the choice of order of polynomial.

A comparison of the fits with different order polynomial background is displayed in Fig 6.18. It should be noticed that the different fits give slightly different normalisations for the correlation function. A higher order polynomial background gives a flatter background at low k^*, but if the order of the polynomial gets too high it goes over unity, which will affect the fitting parameters for the femtoscopic effect. A comparison of the background corrected correlation functions is presented in Fig. 6.19. Fits with higher order polynomials give narrower correlation functions.

The results of the fits are listed in Table 6.2, where the obtained femtoscopic radius R is shown along with the error and the goodness of the fit χ^2 over degrees of freedom DoF. The table shows that we have a generally too small R with a large error. As the order of the polynomial is increased the size of the radius increases, while the error and goodness of fit get better. Again the choice of polynomial dominates the result of the fit, and even with large order polynomials the results do not converge.

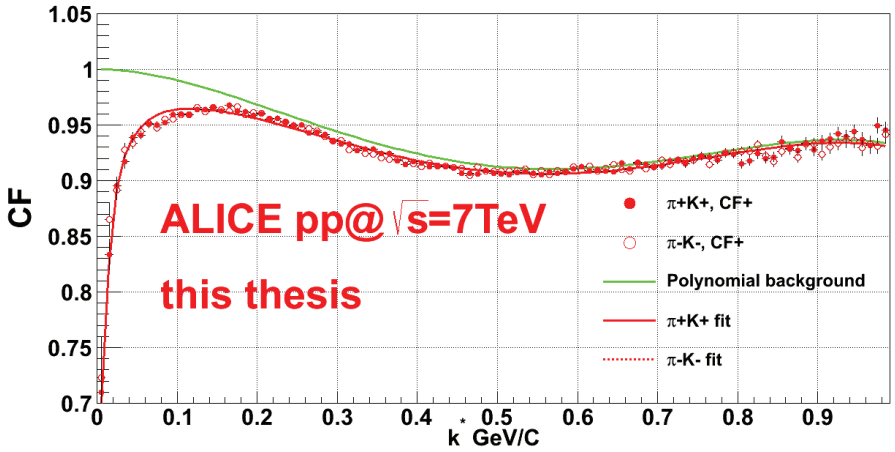

Figure 6.10: Same-sign πK fit with 4th order polynomial background

A general problem when doing these fits is to keep separate the contributions of the femtoscopic effect and the background. The basic idea of the fit is that the Gamow-like factor will fit the femtoscopic effect, while the polynomial will fit the background. Unfortunately as the order of the background polynomial increases, it gets more and more degrees of freedom and it will interfere more and more with the femtoscopic effects. This effect will show up in the χ^2 as a better fit and can therefore only be seen by visually studying the obtained fitting function along with the experimental data. In this case the visual study of the CFs seems to indicate that one can not use a background polynomial of order higher than 6.

As a second test a simultaneous fit is performed for π^+K^- and π^-K^+ pairs. In this case the Breit Wigner function is included in the fit, with M_{inv} calculated from Eq. 6.8 for each k^* bin. In Fig. 6.20 we can see the values of the numerator and denominator of the CF as well as the fit

Order of polynomial background	R, fm	Error, fm	χ^2/DoF
4	0.38	1.28	26.00/192
5	0.33	1.10	25.97/191
6	9.51	5.91	15.04/190
7	0.77	0.56	11.76/189
8	0.82	0.61	10.97/188
9	0.013	0.01	9.78/187
10	9.08	5.91	10.04/186

Table 6.2: Results of same-sign πK fits with different order polynomial backgrounds.

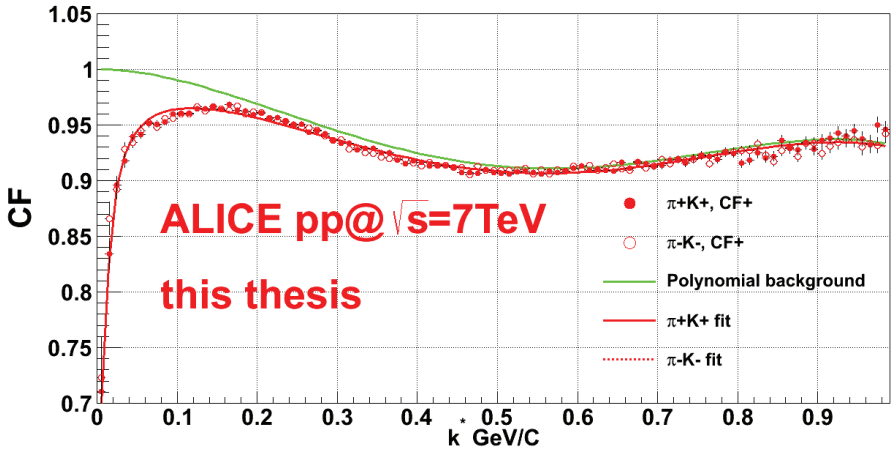

Figure 6.11: Same-sign πK fit with 5th order polynomial background

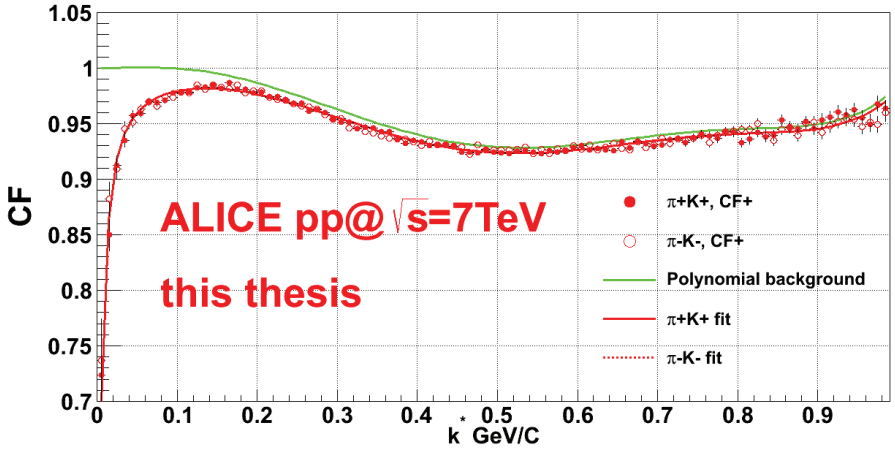

Figure 6.12: Same-sign πK fit with 6th order polynomial background

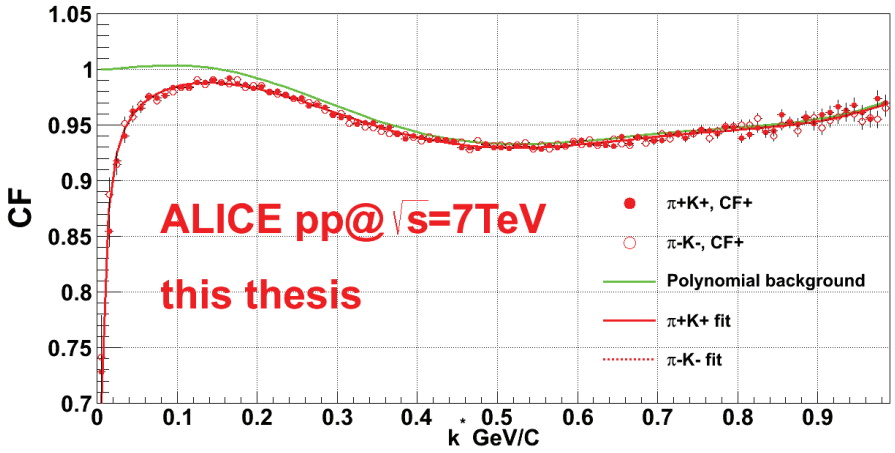

Figure 6.13: Same-sign πK fit with 7th order polynomial background

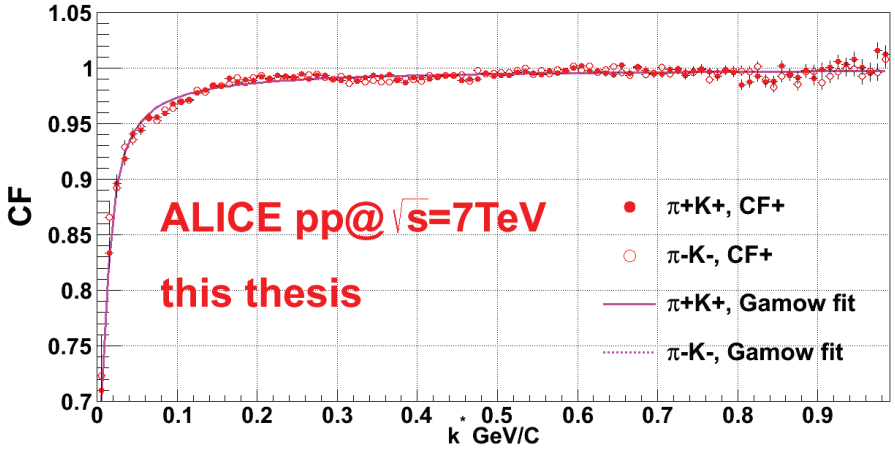

Figure 6.14: Same-sign πK fit with the 4th order polynomial background removed

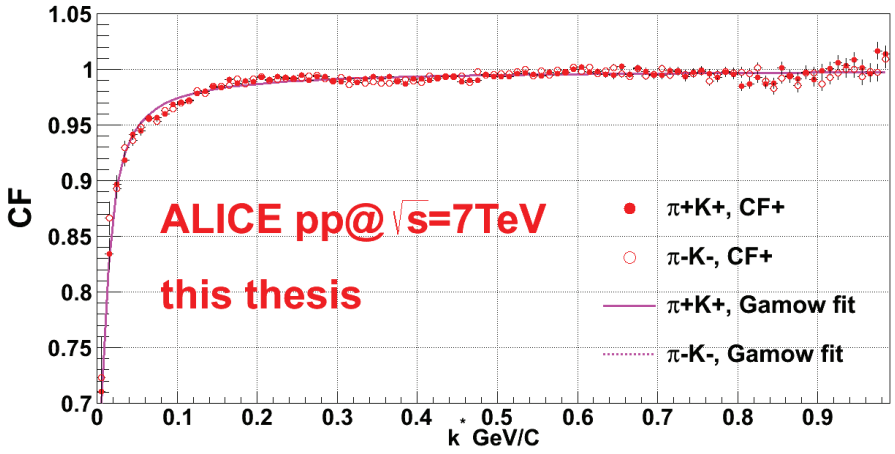

Figure 6.15: Same-sign πK fit with the 5th order polynomial background removed

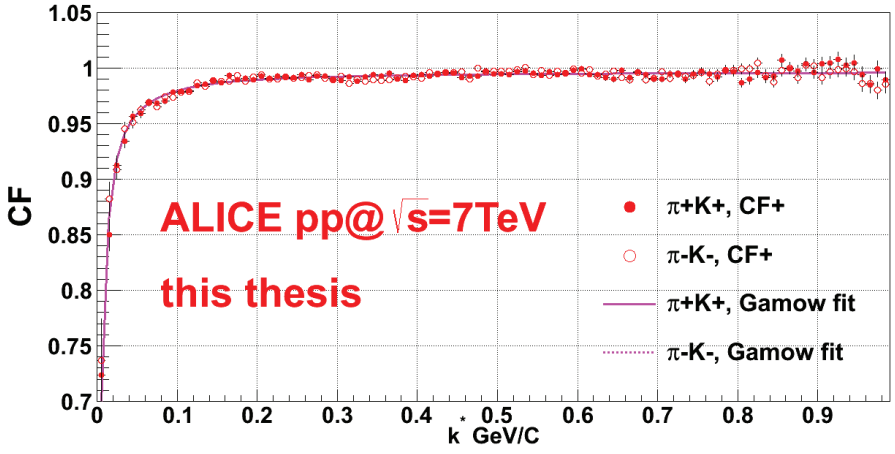

Figure 6.16: Same-sign πK fit with the 6th order polynomial background removed

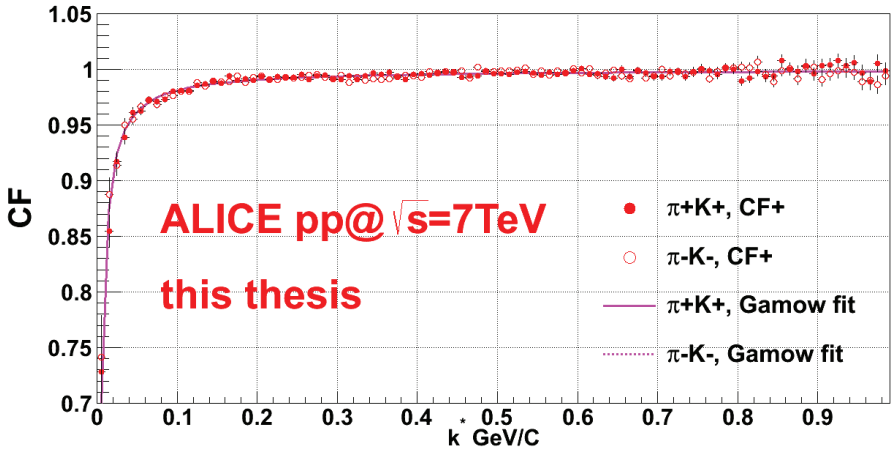

Figure 6.17: Same-sign πK fit with the 7th order polynomial background removed

to the numerator according to Eq. 6.7.

We can now calculate our Breit-Wigner corrected correlation function by the following equation:

$$CF_{BWcorrected}(k^*) = \frac{Num(k^*) - B_{BW}(M_{inv})}{N * Den(k^*)} \tag{6.10}$$

The original and the Breit-Wigner corrected correlation functions are presented in Fig. 6.21. The red point show the original correlation function with the correlation peak. The blue points show the correlation function with the fitted Breit-Wigner from Fig. 6.20 and the polynomial background removed. The green line shows the polynomial describing the background with the femto effect included.

It is again possible to divide the BW corrected CF on the background to get the pure effect CF, however again this depends heavily on the choice of the order of polynomial.

6.4.2 Simultaneous fit of all four pair types

When fitting pairs with only same-sign or opposite-sign it is not easy to disentangle the background from the effect, and as a result we get a dependence on the order of the polynomial used for the background. But since same-sign and opposite-sign pairs have a femtoscopic effect in opposite directions, it should be possible to more clearly separate the effect from the background if one fits all four pair types simultaneously. Again the fit is done with Eq. 6.7, with a Breit-Wigner function for the opposite-sign pairs. The results of the fit using a 7th order polynomial for the background are presented in Fig. 6.22

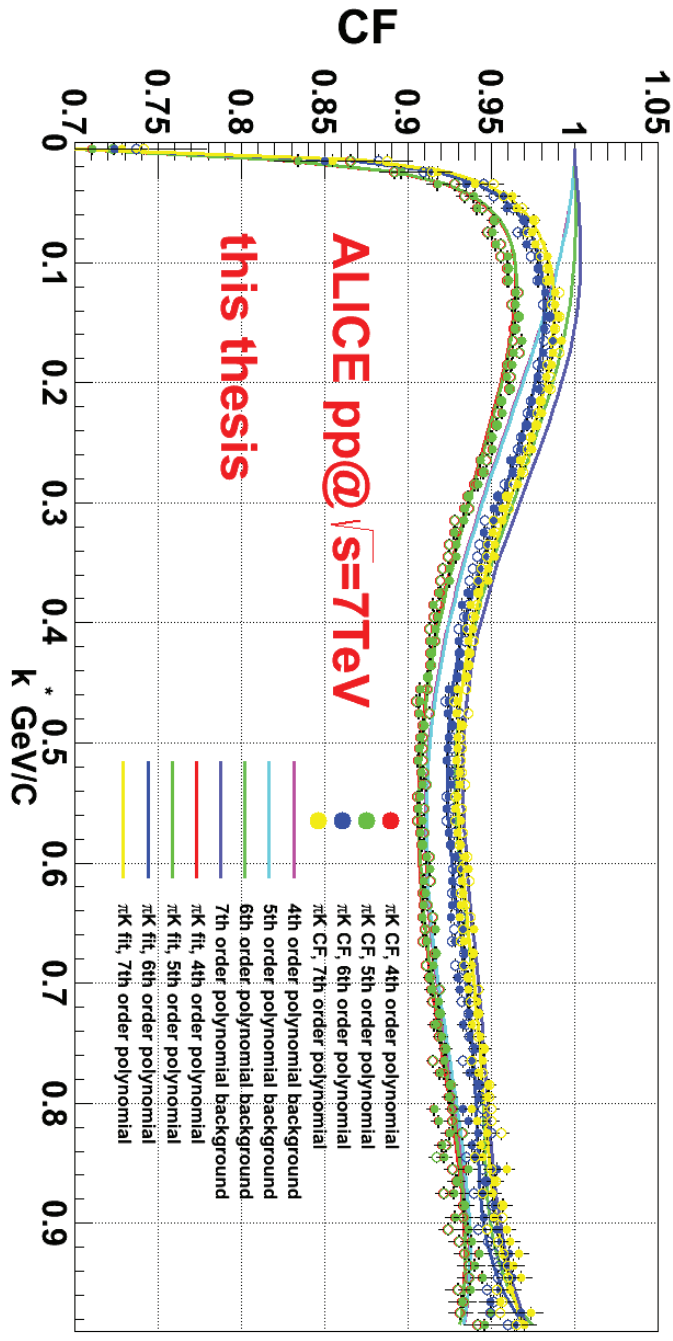

Figure 6.18: Comparison of same-sign πK fits

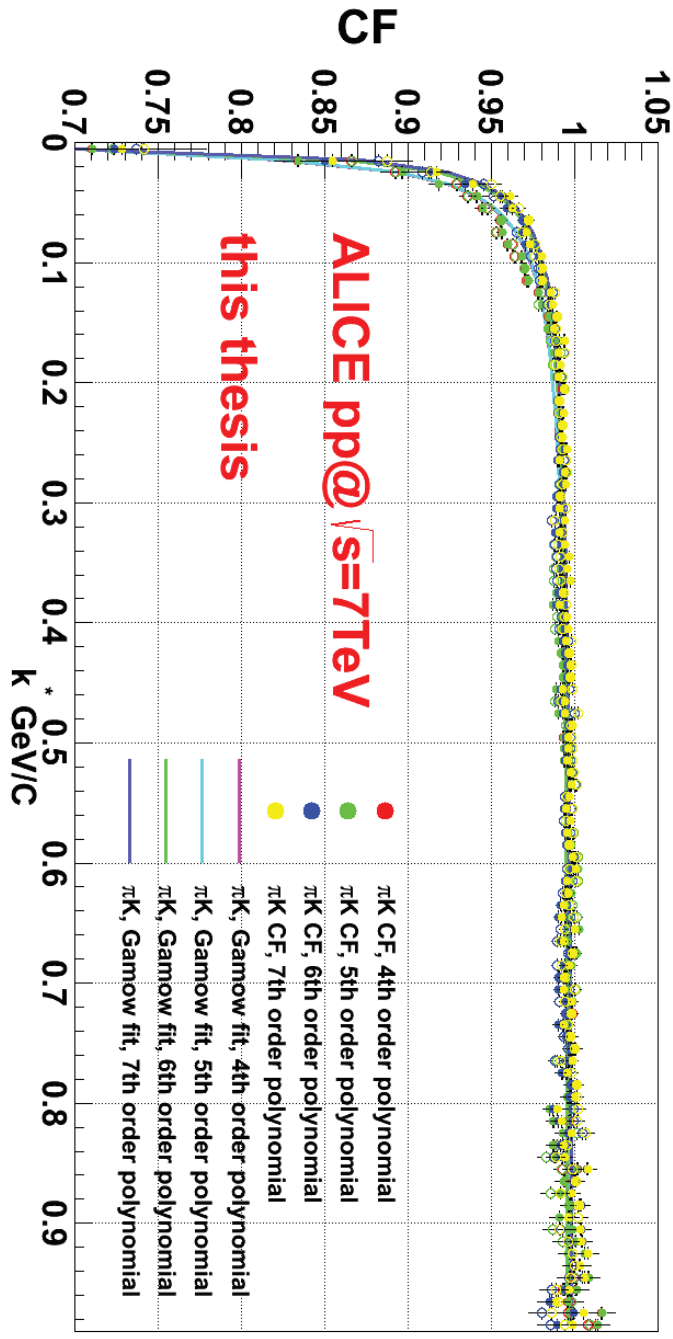

Figure 6.19: Comparison of same-sign πK fits with the polynomial background removed

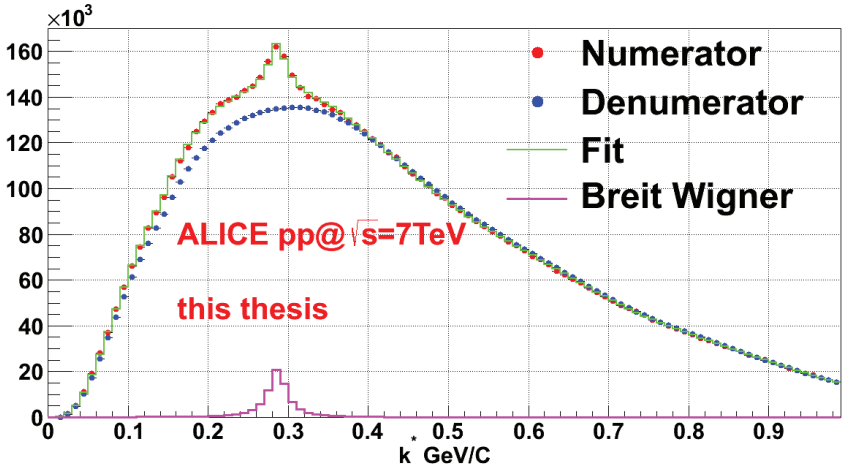

Figure 6.20: Opposite-sign pairs fit of numerator

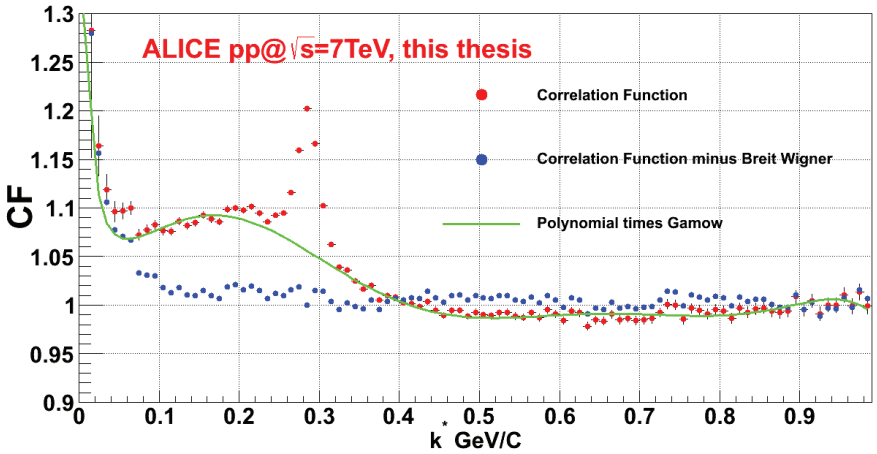

Figure 6.21: Opposite-sign pairs fit of correlation function, with and without Breit-Wigner correction

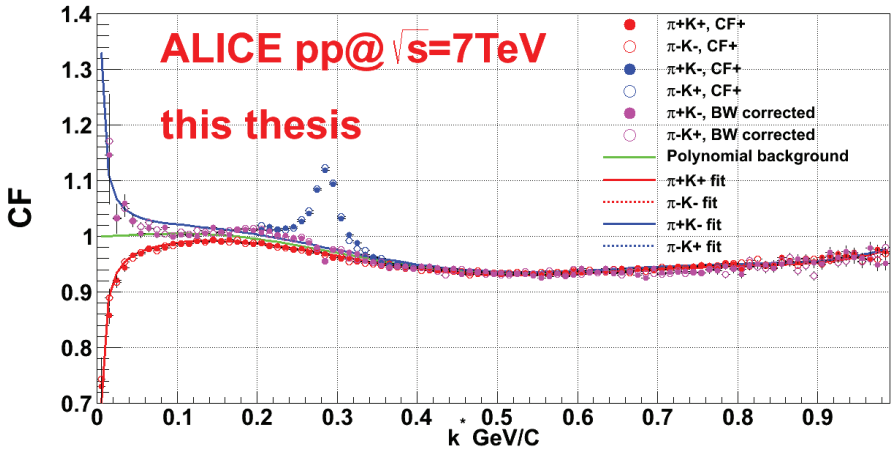

Figure 6.22: Simultaneous fit of all four pair types.

As seen in the figure the fit describes the same-sign pairs well, but is unable to fully account for the dip in the opposite-sign correlation functions in the region between the resonance effect and the femto effect.

6.4.3 Study of fitting techniques for same-sign pairs

In order to extract some reasonable first results from the πK analysis, two additional methods for fitting the same-sign pairs have been tested. The first idea is to use one of the newest tunes of PYTHIA Perugia 2011 to simulate the background, and use it as the baseline during the fitting process. One of the advantages of this method is that it has already been used for $\pi\pi$ and KK pairs, where it gives a good description of the experimental background. The main disadvantage is that it introduces a model dependence in the results.

The second idea is to use the FORTRAN code developed by R. Lednicky [113] that calculated the femto contribution to the correlation function for a given source size from quantum statistics, Coulomb and the strong interaction. The code can be run for different values of the source size, and can be used as the femtoscopic part in a fit. The source size which provides the best background fit can then be taken as the femtoscopic size of the source. The idea can be developed further by letting the femtoscopic part of the fit be an interpolation between several simulated source sizes.

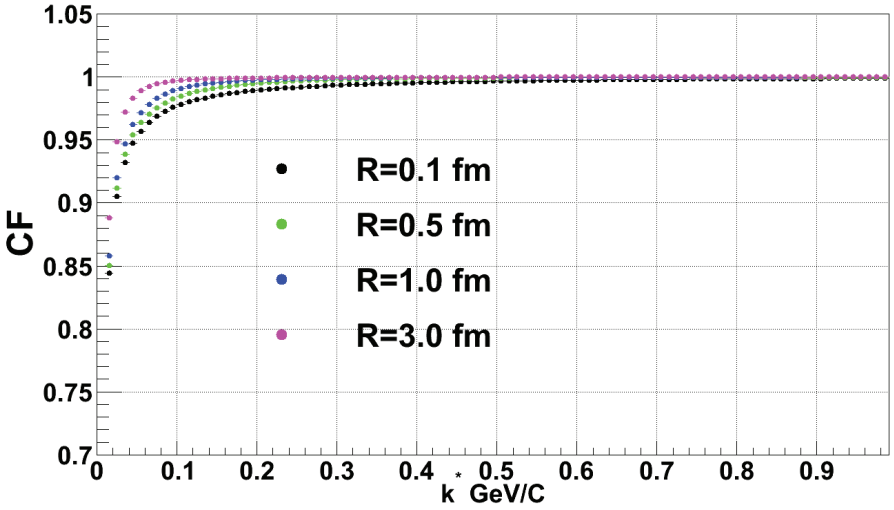

Figure 6.23: Pure theoretical π^+K^+ correlation functions calculated with the Lednicky code.

6.4.4 Using Lednicky's code to simulate the femtoscopic part of the correlation function

Using the FORTRAN code developed by Richard Lednicky it is possible to calculate the theoretical pure femtoscopic correlation functions. These CFs arise from either quantum statistics or Coulomb or the strong interaction, all three can be turned on or off. The code also allows for calculations for 32 different pair types, as well as different models for the Bethe-Salpeter amplitude. The code calculates the theoretical CF for a given value of the source size.

Using this code the theoretical π^+K^+ CF was calculated for the source size values: $R = (0.1, 0.5, 1.0, 3.0)\ fm$ as shown in Fig. 6.23. The narrowing of the CF for increasing sizes can be seen. In addition all the CFs converge to unity for large k^*, this behaviour is in stark contrast to the complicated background seen in experimental CFs.

Using the fitting function from Eq. 6.5 we can for the function $F(k^*)$ use a bin for bin interpolation of the four calculated theoretical CFs in Fig. 6.23. By doing this interpolation we can hopefully extract from the fit the average source size. To test this interpolation method the Lednicky CF is used as the input for the fit. The test fit is performed using a flat background and as seen in Table 6.3 it returns the radius of the input Lednicky CF with very good accuracy. This is a strong indication that the interpolation method can work as way to extract experimental femtoscopic sizes.

When applying this method to the experimental fit the interpolation of Lednicky CFs is assumed to handle the femtoscopic part of the CF while the polynomial is assumed to fit the non-

R for Lednicky CF	R from fit	Normalisation
0.31 fm	0.3308 fm	1.0
1.00 fm	1.00037 fm	0.9999
1.14 fm	1.1388 fm	1.0
2.50 fm	2.5407 fm	1.0

Table 6.3: Results of the interpolation fit using Lednicky CFs as input

Order of polynomial background	R, fm	Error, fm	χ^2/DoF
4	0.31	0.35	24.68/192
5	0.33	0.38	24.46/191
6	2.14	0.56	19.62/190
7	3.00	0.43	14.16/189

Table 6.4: Results of interpolated fits with different order polynomial backgrounds.

femtoscopic background, and should go to unity at low k^*. As seen in the results of the fits in Figs. 6.24, 6.25 and 6.26 this is not necessarily the case. One can see in the figures that the order of the polynomial chosen still has a big impact on the results. The fit with 4th order polynomial background gives a very low value of $R = 0.31\ fm$, visual comparison of the fit also shows that it's off around $k^* = 1.0 GeV/c$. For the 5th order polynomial the fit gives the value $R = 0.33\ fm$, but visually it looks a bit better with a flatter polynomial at low k^*. Unfortunately it fails to describe the high k^* background. For the 6th order polynomial background the fitted value is $R = 2.14\ fm$, visually one can see that the polynomial has gone above unity pulling the CF up and giving an nonphysical value, as discussed in section 6.3.2 we can expect the baseline to be flat at low q_{inv}.

The results of the fits are presented in table 6.4, and we can see that the femtoscopic size increases with the order of the polynomial, while the goodness of fit gets better. Unfortunately the goodness of fit does not measure whether the polynomial is describing the background or the femtoscopic effect, and from visual study of the plots the 6th and 7th order fits can be discarded on the ground that we demand the baseline to be flat at low q_{inv}. This means that the fit with the 5th order polynomial background provides the best results, but lack of consistency in the fits means that the results of the fit are very unstable.

Since the choice of the description of the non-femtoscopic background has a huge impact on the results of the fit another test was performed where the fit was only done in the first few bins, where presumably the background is close to unity. At this range we assume a flat background, and a polynomial is not used in the fit. The results for fitting the 10, 15 and 25 first bins of the experimental CF to the interpolated Lednicky CFs is shown in Figs. 6.27, 6.28 and 6.29 respectively. This test was performed for all possible first number of bins between 10 and the 25, the results of these tests are listed in Table 6.5. It can be clearly seen from the figures that using not enough bins will cause the fit to not describe the full effect, while using too many will

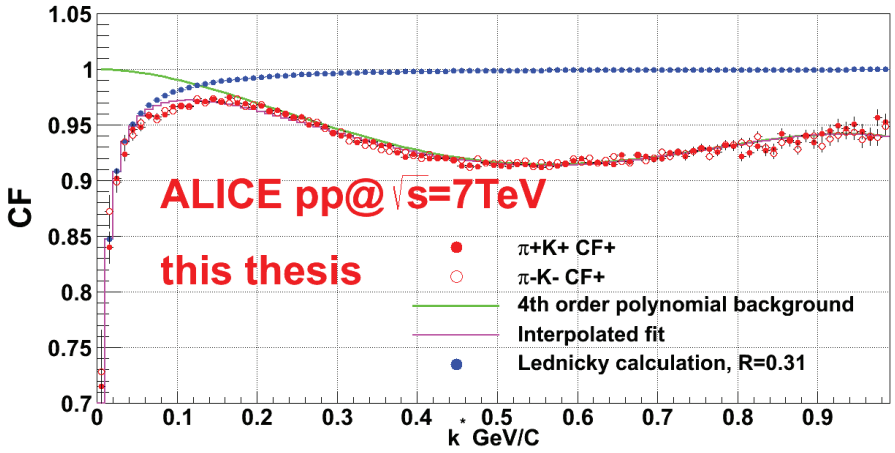

Figure 6.24: πK interpolated fit with $4th$ order polynomial background

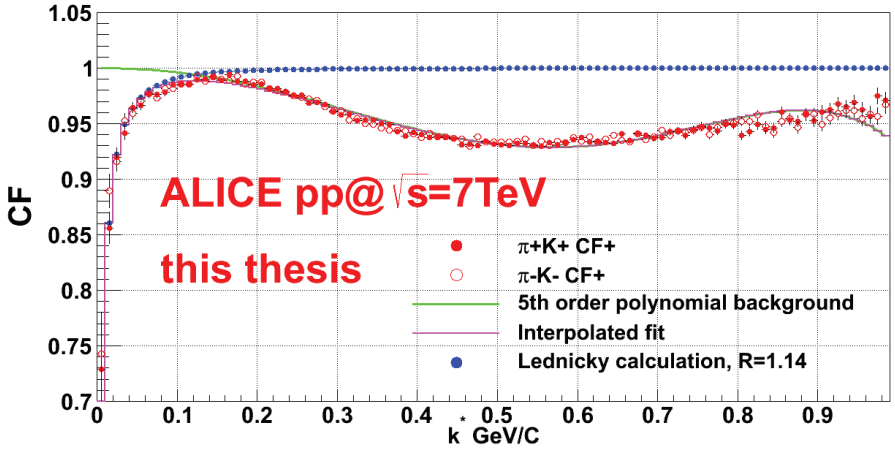

Figure 6.25: πK interpolated fit with $5th$ order polynomial background

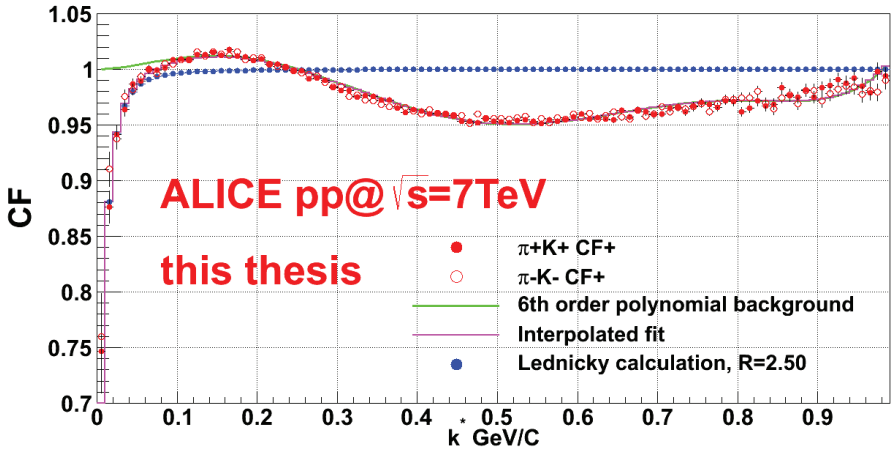

Figure 6.26: πK interpolated fit with $6th$ order polynomial background

include the non-femtoscopic background in the fit. By eye it looks as though 18 is the maximum number of bins that can be included without fitting the background, this value also corresponds to the lowest fitted value of the size $R = 1.2\ fm$. By studying the goodness of the fit χ^2 the same trend can be seen, with the best fit for fitting with the 19 first bins. This gives the size value of $R = 1.24\ fm$.

The assumption of a flat background at low k^* is necessary for these results, but it can be justified with the use of the calculations made with the PYTHIA models where such a flat background at low k^* is observed.

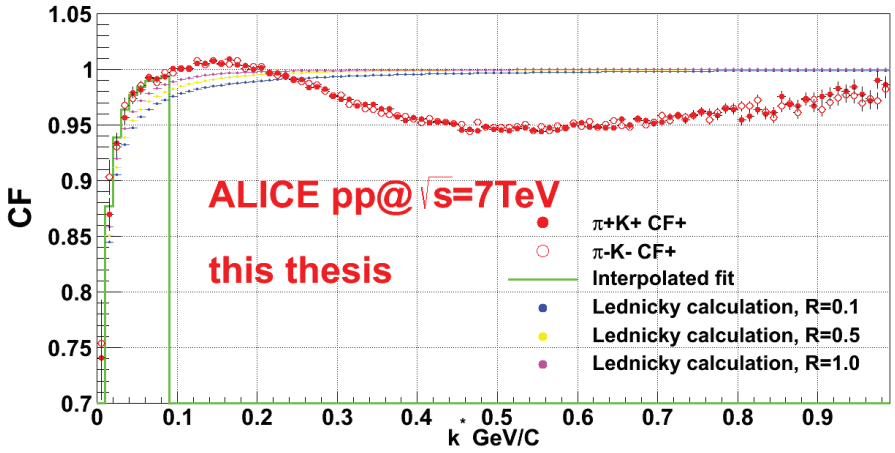

Figure 6.27: The interpolated fit performed for the 10 first bins only.

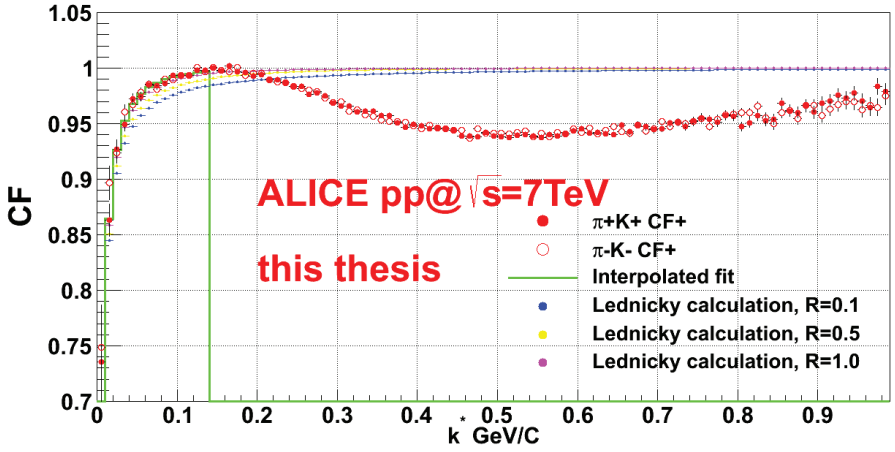

Figure 6.28: The interpolated fit performed for the 15 first bins only.

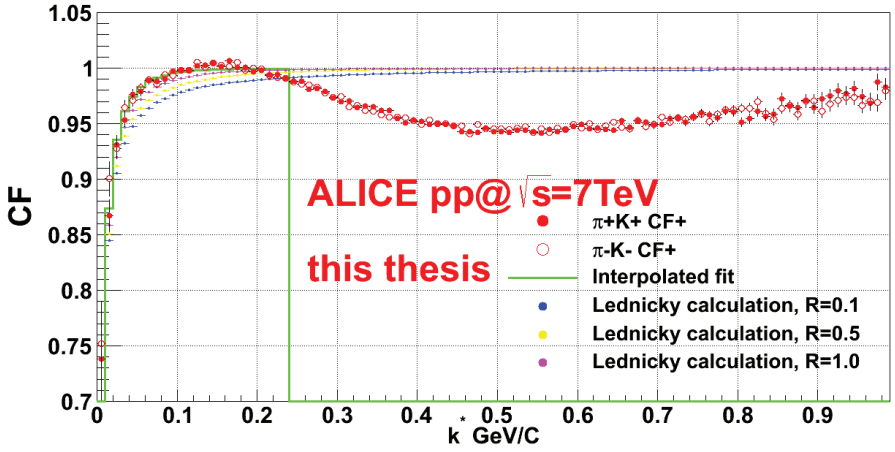

Figure 6.29: The interpolated fit performed for the 25 first bins only.

Number of bins	R, fm	Error, fm	χ^2/DoF
10	2.25	0.32	39.51/16
11	2.06	0.30	41.91/18
12	1.87	0.28	43.49/20
13	1.83	0.26	43.62/22
14	1.47	0.27	52.50/24
15	1.39	0.25	53.16/26
16	1.17	0.23	56.17/28
17	1.24	0.20	56.80/30
18	1.20	0.18	60.28/32
19	1.24	0.16	62.95/34
20	1.41	0.16	72.16/36
21	1.55	0.15	81.36/38
22	1.63	0.14	86.52/40
23	1.80	0.14	115.95/42
24	1.93	0.13	147.25/44
25	2.03	0.13	188.57/46

Table 6.5: Results of the interpolation fit for only the first number of bins with a flat background

Chapter 7

Conclusions

In this work studies of femtoscopic correlations in high-energy proton-proton collisions have been performed from the point of view of both theory and experiment. A general introduction to the field of particle and heavy-ion physics have been made in chapter 1 and 2, both in terms of theory and experimental facilities. The field of femtoscopy have been introduced with theoretical background, motivation and procedures for experimental analysis in chapter 3. The types of theoretical models most often used in the field have been introduced in chapter 4, and the microscopic models employed in this work have been presented in detail.

The simulations and analysis made with the Quark Gluon String Model have been presented in chapter 5. Collisions of minimum bias $\sqrt{s} = 200\ GeV$ and $\sqrt{s} = 900\ GeV$ pp events were simulated. Freeze-out information of coordinates and momentum of the particles in the model is available, and allowed to create freeze-out spectra. These distributions showed the hydro-like evolution of the system, the appearance of a resonance peak and inherent $p_x - x$ correlations in the model. Distributions were created for π,p,K and $\Lambda + \Sigma^0$, and showed the difference in multiplicity and formation time, arising from the different masses.

Femtoscopic analysis was performed and comparisons made to experimental data published by the STAR and ALICE experiments. Analysis procedure was done in such a way as to mimic the procedures of the experiments as closely as possible. Both 1-dimensional and 3-dimensional correlation functions were created, and fitting procedures extracted the femtoscopic sizes of the system.

The scaling parameter of the string tension in the QGSM model was used to tune the model results to the experimental. It was found that it was needed to be twice the size for the $\sqrt{s} = 900\ GeV$ data compared to the $\sqrt{s} = 200\ GeV$ data. QGSM reproduced well the k_T-dependence of the radius for the 1-dimensional case. The origin of this dependence was found to be in the relative contribution from resonances as well as a natural $p_x - x$ correlation in the model.

Pions in the QGSM model are created either directly through string fragmentation, or through the decays of resonances. The relative contribution of pions from long lived resonances to direct pions decrease with increasing k_T, giving rise to a decrease of R_{inv} with k_T. A two-Gaussian fitting method was performed, and allowed to separate the contributions of the direct pions from the contributions from pions from resonances. Similar to experiment the radii of $900\ GeV$ is smaller than the radii for $200\ GeV$. The analysis favours a reduction of the formation time with

increasing energy of the hadronic collision.

The full 3-dimensional correlation functions were fitted, and were found not to be perfect Gaussian. A good correspondence to experimental data was still present.

In chapter 6 the analysis of non-identical πK correlations from $\sqrt{s} = 7\ TeV$ ALICE data was presented. Two methods for particle identification were studied, with Number of Sigma as the preferred method. Experimental correlation functions were constructed in three multiplicity bins. A strong correlation effect at low k^* due to Coulomb final state interactions was observed. This effect is positive for the same sign pairs π^+K^+ and π^-K^-, while it was negative for the opposite sign pairs π^+K^- and π^-K^+. The K^* resonance can be clearly seen from a peak in the opposite sign correlation functions, originating from the decay of the resonance $K^* \rightarrow \pi^+K^-$ and $K^* \rightarrow \pi^-K^+$. At large k^* long-range non-femtoscopic correlations are observed.

Correlation functions constructed from the PYTHIA-0 and PYTHIA-2011 models were also introduced for comparison. Results from the models described the non-femtoscopic background qualitatively but not quantitatively, and could therefore not be used to exclude the background. Several fitting strategies were tried, with the main difficulty to find a stable procedure capable of separating the background from the femtoscopic effect. For all methods the simultaneous fitting procedure was used, employing data from different pair types.

A Gamow-like fitting function was tried, with polynomials used to simulate the background. The results for same sign pairs were found to depend heavily on the order of the polynomial. Opposite sign pairs were fitted using a Breit-Wigner function to separate the K^* resonance peak, and fitting for all four pair types simultaneously was tried. The fit was shown to be unable to describe the opposite sign pair correlation functions properly. PYTHIA Perugia 2011 was employed, but was unable to describe the background. The PYTHIA calculation did however show that the background should be flat at low k^*. A third attempt was made using the Lednicky code to simulate the femtoscopic effect. It was found to give a realistic value of $R = 1.14\ fm$ when the demand that the background should be flat at low k^* was enforced. By performing the same fitting procedure at only the lower bins of the correlation function, and still enforcing the same demand of a flat background, a value of $R = 1.24\ fm$ was the result.

Appendix A

Space-time coordinates of produced hadrons

Considering the production of particles in a Lund-type string model, as described in section 4.2.1, from the sequential breaking of strings. At time t_i the string breaks for the ith time, producing quark pair $q_i\bar{q}$. Hadrons are produced from quarks from different pairs $\bar{q}_{i-1}q_i$. The energy and momentum of hadron i is:

$$\begin{aligned} E_i &= \kappa(z_{i-1} - z_i) \\ p_i &= \kappa(t_{i-1} - t_i) \end{aligned} \tag{A.1}$$

where z_i is the initial position and t_i is the formation time of the ith quark.

It is useful to define the light-cone variables for a hadron:

$$\begin{aligned} p_i^{\pm} &= E_i \pm p_i \\ z_i^{\pm} &= t_i \pm z_i \end{aligned} \tag{A.2}$$

for "constituent" formation time we get:

$$\begin{aligned} p_i^+ = E_i + p_i &= \kappa\left[z_{i_1} - z_i + t_{i-1} - t_i\right] \\ &= \kappa\left[(z_{i_1} + t_{i-1}) - (z_i + t_i)\right] \\ &= \kappa\left[z_{i_1}^+ - z_i^+\right] \\ p_i^- = E_i - p_i &= \kappa\left[z_{i_1} + z_i - t_{i-1} + t_i\right] \\ &= \kappa\left[(z_{i_1} - t_{i-1}) - (z_i - t_i)\right] \\ &= \kappa\left[z_{i_1}^- - z_i^+\right] \end{aligned} \tag{A.3}$$

Arranging the equations we get:

$$\begin{aligned} z_i^+ &= z_{i-1}^+ - \frac{p_i^+}{\kappa} \\ z_i^- &= z_{i+1}^+ + \frac{p_i^-}{\kappa} \end{aligned} \tag{A.4}$$

using a recursive solution one can write:

$$\begin{aligned} z_i^+ &= z_0^+ - \frac{1}{\kappa}\sum_{j=1}^{i} p_j^+ \\ z_i^- &= z_0^+ + \frac{1}{\kappa}\sum_{j=1}^{i} p_j^- \end{aligned} \tag{A.5}$$

Inserting the boundary values $z_0^+ = \dfrac{E_0 + p_0}{\kappa} = \dfrac{M_s}{\kappa}$ and $z_0^- = 0$ [91], where M_s is the mass of the string, we get the expressions for the (t_i, z_i) coordinates of the produced hadrons:

$$\begin{aligned} z_i = \frac{1}{2}\left[z_i^+ - z_i^-\right] &= \frac{1}{2}\left[\frac{M_s}{\kappa} - \frac{1}{\kappa}\sum_{j=1}^{i} p_j^+ - \frac{1}{\kappa}\sum_{j=1}^{i} p_j^-\right] \\ &= \frac{1}{2\kappa}\left[M_s - \sum_{j=1}^{i}(p_j^+ + p_j^-)\right] \\ &= \frac{1}{2\kappa}\left[M_s - 2\sum_{j=1}^{i} E_j\right] \\ t_i = \frac{1}{2}\left[z_i^+ + z_i^-\right] &= \frac{1}{2}\left[\frac{M_s}{\kappa} - \frac{1}{\kappa}\sum_{j=1}^{i} p_j^+ + \frac{1}{\kappa}\sum_{j=1}^{i} p_j^-\right] \\ &= \frac{1}{2\kappa}\left[M_s - \sum_{j=1}^{i}(p_j^+ - p_j^-)\right] \\ &= \frac{1}{2\kappa}\left[M_s - 2\sum_{j=1}^{i} p_j\right] \end{aligned} \tag{A.6}$$

Bibliography

[1] H. Geiger, E. Marsden, Proc. Roy. Soc. **A82**, (1909) 495-500.

[2] ATLAS Collaboration et al, arXiv:1207.7214v1 [hep-ex].

[3] CMS Collaboration et al, arXiv:1207.7235v1 [hep-ex].

[4] "The Nobel Prize in Physics 2004". Nobelprize.org. 25 Sep 2012 http://www.nobelprize.org/nobel_prizes/physics/laureates/2004/

[5] D. Diakonov, Z. Phys. **A359** (1997) 305-314.

[6] R. Heuer, A. Wagner, CERN Courier Jan 21, 2008, http://cerncourier.com/cws/article/cern/32527

[7] "Quark-Gluon Plasma", edited by R. Hwa and X. N. Wang, vol. I-IV (World Scientific, Singapore, 1990, 1995, 2004, 2009).

[8] G. Løvhøiden, Lecture notes for FYS374 (unpublished).

[9] G. Odyniec, J. Phys. G: Nucl. Part. Phys. **37** 094028 (2010).

[10] I. Arsene et al (BRAHMS Collaboration), Nucl. Phys. **A757**, 1-27 (2005).

[11] B. B. Back et al (PHOBOS Collaboration), Nucl. Phys. **A757**, 28-101 (2005).

[12] J. Adams et al (STAR Collaboration), Nucl. Phys. **A757**, 102-183 (2005).

[13] K. Adcox et al (PHENIX Collaboration), Nucl. Phys. **A757**, 184-283 (2005).

[14] E. Shuryak, Prog. Part. Nucl. Phys. **53** (2004) 273-303.

[15] ALICE Collaboration et al, arXiv:1004.3514v2 [hep-ex]

[16] LHC website, http://public.web.cern.ch/public/en/lhc/lhc-en.html

[17] CERN website, http://public.web.cern.ch/public/

[18] RHIC website, http://www.bnl.gov/rhic/

[19] Tevatron website, http://www-bdnew.fnal.gov/tevatron/

[20] FAIR website, http://www.fair-center.de/index.php?id=1&L=0

[21] NICA website, http://nica.jinr.ru/

[22] CLIC website, http://clic-study.web.cern.ch/clic-study/

[23] ILC website, http://www.linearcollider.org/

[24] eRHIC website, http://www.phenix.bnl.gov/WWW/publish/abhay/Home_of_EIC/

[25] ALICE website, http://aliceinfo.cern.ch/Public/Welcome.html

[26] STAR website, http://www.star.bnl.gov/

[27] ATLAS website, http://atlas.ch/

[28] CMS website, http://cms.web.cern.ch/

[29] LHCb website, http://lhcb.web.cern.ch/lhcb/

[30] N. Antoniou et al., Letter of intent for a large ion collider experiment at the (CERN) Large Hadron Collider, CERN Report **CERN/LHCC/93-16** (1993).

[31] K. Werner, Iu. Karpenko,T. Pierog, Phys. Rev. Lett. **106**, (2011) 122004.

[32] K. Werner et al, Phys. Rev. **C83**, (2011) 044915.

[33] S. A. Voloshin, A. M. Poskanzer, Phys. Rev. C **58**, (1998) 1671-1678.

[34] S. A. Voloshin, Y. Zhang, Z. Phys. **C70** (1996) 665-672.

[35] S. A. Voloshin, A. M. Poskanzer, R. Snellings, arXiv:0809.2949 [nucl-ex] (2008).

[36] J. Y. Ollitrault, Phys. Rev. D **46**, (1992) 229-245.

[37] J. Jia (for the ATLAS Collaboration) J. Phys. G: Nucl. Part. Phys. **38** (2011) 124012 (8pp).

[38] N. Borghini, R. S. Bhalerao, J. Y. Ollitrault, J. Phys. **G30**, (2004) S1213-S1216.

[39] M. Luzum, J. Y. Ollitrault, arXiv:1209.2323 [nucl-ex]

[40] K. J. Eskola Nucl. Phys. **A698** (2002) 78-87.

[41] ALICE Collaboration et al, arXiv:1011.3916v3 [nucl-ex].

[42] D. Elia (for the ALICE Collaboration) arXiv:1102.2369v1 [hep-ex].

[43] Marek Chojnacki (for the ALICE Collaboration) 2011 J. Phys. G: Nucl. Part. Phys. **38** 124074.

[44] M. A. Braun, C. Pajares, Eur. Phys. J. **C16** (2000) 349-359.

[45] ALICE Collaboration et al, J. Phys. G: Nucl. Part. Phys. **30** 1517 (2004).

[46] ALICE Collaboration et al, J. Phys. G: Nucl. Part. Phys. **32** 1295 (2006).

[47] ALICE Collaboration et al, Phys. Rev. Lett. **105**, 252302 (2010).

[48] ALICE Collaboration et al, Phys. Rev. Lett. **107**, 032301 (2011).

[49] M. A. Stephanov, K. Rajagopal, E. Shuryak, Phys. Rev. **D60**, (1999) 114028.

[50] B. G. Zakharov, JETP Letters **63**, (1996) 952; ibid **65**, (1997) 615.

[51] R. Baier, Y. I. Dokshitzer, A. H. Mueller, S. Peigne and D. Schiff, Nucl. Phys. **B483**, (1997) 291; ibid. **B484**, (1997) 265

[52] W. Cassing, E. L. Bratkovskaya, Phys. Rept. **308**, (1999)

[53] T. Matsui, H. Satz, Phys. Lett. **B178**, (1986) 416.

[54] G. S. Bali, Phys. Rep. **343**, (2001).

[55] J. Schukraft ALICE Overview talk, Quark Matter 2011, Annecy, France.

[56] P. Pillot, Presentation at Quark Matter 2011, Annecy, France.

[57] R. Hanbury-Brown, R. Q. Twiss, Phil. Mag. **45** (1954) p 663-682.

[58] R. Hanbury-Brown, R. Q. Twiss, Nature **177** (1956).

[59] R. Hanbury-Brown, R. Q. Twiss, Nature **178** (1956).

[60] J. Davis, M. J. Ireland, J. R. North, J. G. Robertson, W. J. Tango, P. G. Tuthill, arXiv:1010.3790v1 [astro-ph.SR] (2010).

[61] G. Goldhaber, S. Goldhaber, W. Lee, A. Paist, Phys. Rev. **120** (1960) p 300.

[62] S. E. Koonin, Phys Lett **B70**, 43 (1977).

[63] S. Pratt, Phys. Rev. Lett. **53**, 1219 (1984).

[64] A. Makhlin, Y. M. Sinyukov, Z. Phys. **C39**, 69 (1988).

[65] M. A. Lisa, S. Pratt, R. Soltz, U. Wiedemann, Annu. Rev. Nucl. Part. Sci. 2005. 55:357-402.

[66] U. A. Wiedemann, U. Heinz, Phys. Rep. **319**, 145 (1999)

[67] M. A. Lisa et al, Phys. Lett. **B496**, 1 (2000).

[68] S. A. Voloshin, W. E. Cleland, Phys Rev **C53**, 896 (1996).

[69] STAR Collaboration (J. Adams et al), Phys. Rev. Lett. **93** (2004) 012301.

[70] J. Gramling, CERN-THESIS-2012-088.

[71] P. Danielewicz, S. Pratt, Phys. Rev. **C75**, (2007) 034907.

[72] A. Kisiel, D. A. Brown, Phys. Rev. **C80**, (2009) 064911.

[73] Z. Chajecki, M. Lisa, Phys. Rev. **C78**, (2008) 064903.

[74] A. Kisiel, PhD thesis (2004).

[75] S. Voloshin, R. Lednicky, S. Panitkin, N. Xu, Phys. Rev. Lett. **79** (1997) 4766-4769.

[76] M. M. Aggarwal et al (STAR Collaboration), Phys. Rev. **C83** (2011) 064905.

[77] ALICE Collaboration et al, Phys. Lett. **B696**, (2011) 328-337.

[78] A. Kisiel, PoS (WPCF2011) 003.

[79] M. P. Szymanski, Quark Matter 2012 presentation.

[80] ALICE Collaboration, Phys. Rev. **D82**, 052001 (2010).

[81] ALICE Collaboration, Phys. Rev. **D84**, 112004 (2011).

[82] T. J. Humanic, J. Phys. **G38**, 124058 (2011).

[83] ALICE Collaboration, arXiv:1206.2056.

[84] K. Werner, I. Karpenko, T. Pierog, M. Bleicher and K. Mikhailov, Phys. Rev. **C83**, 044915 (2011).

[85] K. Werner, K. Mikhailov, I. Karpenko and T. Pierog, arXiv:1104.2405 [hep-ph]

[86] ALICE Collaboration, Phys. Lett. **B717**, 151-161 (2012).

[87] L. D. Landau, Izv. Akad. Nauk Ser. Fiz. **17** (1953) 51.

[88] J. D. Bjorken, Phys. Rev. D. **27** (1983) 140.

[89] F. Cooper, G. Frye, Phys. Rev. **D10** 186 (1975).

[90] Iu. A. Karpenko, Yu. M. Sinykov, K. Werner, arXiv:1204.5351 [nucl-th].

[91] B. Andersson et al, Phys. Rept. **97** 31-145 (1983).

[92] A. Bialas, M. Gyulassy, Nucl. Phys. **B291**, 793 (1987).

[93] A.B. Kaidalov, Phys. Lett. **B116**, 459 (1982); A.B. Kaidalov and K.A. Ter-Martirosyan, Phys. Lett. **B117**, 247 (1982).

[94] G. t'Hooft, Nucl. Phys. **B72**, 461 (1974).

[95] G. Veneziano, Phys. Lett. B **52**, 220 (1974).

[96] M. Cifaloni, G. Marchesini, and G. Veneziano, Nucl. Phys. **B98**, 472 (1975).

[97] A.B. Kaidalov, Surveys in High Energy Phys. **13**, 265 (1999).

[98] N.S. Amelin and L.V. Bravina, Sov. J. Nucl. Phys. **51**, 133 (1990) [Yad. Fiz. **51**, 211 (1990)]; N.S. Amelin, L.V. Bravina, L.I. Sarycheva, and L.I. Smirnova, Sov. J. Nucl. Phys. **51**, 535 (1990) [Yad. Fiz. **51**, 841 (1990)].

[99] V. Abramovskii, V. Gribov, and O. Kancheli, Sov. J. Nucl. Phys. **18**, 308 (1974) [Yad. Fiz. **18**, 595 (1973)].

[100] S. A. Bass et al, Prog. Part. Nucl. Phys **41** (1998) 255-369.

[101] M. Bleicher et al, J. Phys. G: Nucl. Part. Phys. **25** (1999) 1859-1896.

[102] G.J. Alner *et al.* (UA5 Collab.), Phys. Rep. **154**, 247 (1987).

[103] G. Arnison *et al.* (UA1 Collab.), Phys. Lett. B **118**, 167 (1982); C. Albajar *et al.* (UA1 Collab.), Nucl. Phys. **B335**, 261 (1990).

[104] F. Abe *et al.* (CDF Collab.), Phys. Rev. Lett. **61**, 1819 (1988); Phys. Rev. D **41**, R2330 (1990).

[105] CMS Collaboration (K. Khachatryan *et al.*), Phys. Rev. Lett. **105**, 022002 (2010) (arXiv:1005.3299 [hep-ex]).

[106] ALICE Collaboration (K. Aamodt *et al.*), Eur. Phys. J. C **68**, 345 (2010) (arXiv:1004.3514 [hep-ex])

[107] M. S. Nilsson et al, Phys. Rev. **D84** (2011) 054006.

[108] L. V. Bravina, I. N. Mishustin, J. P. Bondorf, A. Faessler, E. E. Zabrodin, Phys. Rev. **C60** 044905 (1999).

[109] R. Lednicky, T. Progulova, Z. Phys. **C55**, 295 (1992).

[110] J. Adams et al (STAR Collaboration), Phys. Rev. Lett. **91** (2003) 262302.

[111] T. Sjostrand, S. Mrenna, P. Skands, JHEP 0605:026 (2006), arXiv:hep-ph/0603175

[112] P. Skands, Phys. Rev. **D82**, 074018 (2010).

[113] R. Lednicky, V. L. Lyoboshitz, Sov. J. Nucl. Phys. **35** (1982).

Part II

Papers

I

ISSN 1547-4771, Physics of Particles and Nuclei Letters, 2011, Vol. 8, No. 9, pp. 1000–1003. © Pleiades Publishing, Ltd., 2011.

Study of $\pi\pi$ Correlations at RHIC and LHC Energies in *pp* Collisions within the Quark-Gluon String Model[1]

M. S. Nilsson[a], L. V. Malinina[b], J. Bleibel[c, d], L. Bravina[a, b], and E. Zabrodin[a, b]

[a] *Department of Physics, University of Oslo, Oslo, Norway*
[b] *Institute for Nuclear Physics, Moscow State University, Moscow, Russia*
[c] *Institute for Physics, Johannes Gutenberg University Mainz, Germany*
[d] *Max-Planck-Institute for Metal Research, Stuttgart, Germany*

Abstract—The main goal of this work is to employ the Monte Carlo Quark Gluon String Model (QGSM) for description of femtoscopic characteristics in *pp* collisions at RHIC and LHC. It was found that experimental data can be reasonably well described within the pure string model by increasing the string tension by a factor of two with energy rising from $\sqrt{s} = 200$ GeV to $\sqrt{s} = 900$ GeV. The double-Gaussian fit reveals the contributions from resonances and directly produced particles.

DOI: 10.1134/S1547477111090263

1. INTRODUCTION

Experiments at RHIC have demonstrated that hot and dense matter with partonic collectivity has been formed in ultrarelativistic Au + Au collisions at $\sqrt{s} =$ 200 GeV. Proton-proton collisions are conventionally used as a reference to compare with nuclear collisions and to understand the observed collective effects. The new interest to general features of *pp* collisions at ultrarelativistic energies appeared after the first publication of Large Hadron Collider data at $\sqrt{s} =$ 900 GeV and $\sqrt{s} = 7$ TeV.

The system created in ultrarelativistic *pp* collisions at RHIC and especially LHC energies can be similar to the system created in non-central heavy-ion collisions because of the large energy deposited in the overlapping region and therefore can also demonstrate the collective behavior. The strong argument supporting this point of view comes from the observation of the same momentum dependence of the femtoscopic radii in *pp* and Au+Au collisions by STAR experiment at RHIC [1].

The Bose–Einstein correlations for *pp* collisions at $\sqrt{s} = 900$ GeV obtained in the ALICE experiment [2] have been successfully described within the EPOS+hydro model [3]. It was shown that the hydrodynamic expansion drastically modifies the space-time behavior of the evolution compared to the "classical" EPOS scenario with independent decay of flux-tube strings.

The quark-gluon string model based on Gribov-Regge theory gives a good description of the collective flow effects in Au+Au collisions at RHIC energies; the tuning of QGSM for *pp* collisions at LHC energies allowed authors to describe successfully the main characteristics of *pp* interactions, i.e. multiplicity, transverse momentum and (pseudo)rapidity distributions, up to top LHC energy $\sqrt{s} = 7$ TeV [4]. The aim of the present article is to study hadronization processes in *pp* collisions at ultrarelativistic energies using momentum correlations techniques with the QGSM model and to compare obtained results with the experimental data of RHIC and LHC. We try to understand to what extent one is able to describe the correlation functions (CFs) in ultrarelativistic *pp* collisions within the pure string model picture.

2. QGSM AND PARTICLE COORDINATES

The hadrons in QGSM are produced through the creation and decay of resonances, strings and minijets. The space-time evolution of the collisions starts from the interacting partons (quark, diquark and seaquarks) distributed randomly in the projectile-target overlapping region. The strings between them are stretching and decaying into the hadrons. Due to uncertainty principle it takes time to create a hadron from constituent quarks. It was supported by experiment that fast particles are created the last. In string models two definitions of formation time are accepted: the time when string is broken and all constituents of the hadron are created (constituent) or the time when the trajectories of hadron constituents (quarks) cross ("yo-yo"). In this version of QGSM we are using the smallest formation time—constituent. The formation time t_i^* and coordinate z_i^* of i-th hadron in the string center of

[1] The article is published in the original.

mass can be expressed thought its energy E_i^*, its longitudinal momentum p_{zi}^* and the longitudinal momenta/energies of all hadrons produced by the decay of this string:

$$t_i^* = \frac{1}{2\kappa}\left(M_s - 2\sum_{j=1}^{i-1} p_{zj}^*\right),$$
$$z_i^* = \frac{1}{2\kappa}\left(M_s - 2\sum_{j=1}^{i-1} E_j^*\right). \quad (1)$$

Then we calculate t_i in the laboratory frame and make the propagation of the coordinates to this point (x_i, y_i, z_i, t_i): $a_i = a_{0i} + t_i p_{ai}/E_i$, $a = x, y, z$. We have studied the influence of the strength of string tension κ on the space-time distributions and the corresponding correlation functions. Note that κ acts as a scaling parameter of the particle formation time.

3. THE TWO-PION CORRELATION FUNCTIONS

The momentum correlations are usually studied with the help of correlation functions of two or more particles. Particularly, the two-particle correlation function $CF(p_1, p_2) = A(p_1, p_2)/B(p_1, p_2)$ is defined as a ratio of the two-particle distribution from the same event $A(p_1, p_2)$ to the reference one. The reference distribution is typically constructed by mixing the particles from different events of a given class. In ππ correlations in *pp* collisions the Coulomb correction can be neglected.

In our simulations the weight of each particle pair is calculated according to quantum statistics, using particle four-momenta p_i and four-coordinates x_i of the emission points: $w = 1 + \cos(q \cdot \Delta x)$, where $q = p_1 - p_2$ and $\Delta x = x_1 - x_2$. The CF is defined as a ratio of the weighted histogram of the pair kinematic variables to the unweighted one.

The "ideal" case, $CF_{\text{ideal}}(p_1, p_2) = A(p_1, p_2, w)/A(p_1, p_2)$, uses unweighted pairs from the same events as the reference. A more realistic case, $CF_{\text{realistic}}(p_1, p_2) = A(p_1, p_2, w)/B(p_1, p_2)$, uses unweighted mixed pairs from different events as the reference. There is a difference between the ideal pair distribution $A(p_1, p_2)$ and the mixed one $B(p_1, p_2)$ due to presence of momentum conservation for the pairs from the same event and absence of it in pairs from the mixed ones. This causes a smooth increase of $CF_{\text{realistic}}$ with q_{inv}, which reflects the fact that due to momentum conservation the probability of two particles emitted in the same direction is smaller than that of two particles emitted in opposite directions. We take this into account by using more complicated fitting procedure for the "realistic CF" than for the "ideal CF".

In both the STAR [1] and the ALICE [2] experiments the correlation function is fitted to a single-Gaussian. However the fit is unable to describe the peak at low q_{inv}. We fit the CFs by two different fitting functions: a single-Gaussian, like in the experiment, and a double-Gaussian (reflecting 2 sizes presented in the data, direct π and the resonance halo):

$$CF_{\text{single}}(q_{\text{inv}}) = (1 + \lambda \exp(-R_{\text{inv}}^2 q_{\text{inv}}^2)) D(q_{\text{inv}}), \quad (2)$$

$$CF_{\text{double}}(q_{\text{inv}}) = (1 + \lambda_1 \exp(-R_{\text{inv},1}^2 q_{\text{inv}}^2) + \lambda_2 \exp(-R_{\text{inv},2}^2 q_{\text{inv}}^2)) D(q_{\text{inv}}), \quad (3)$$

where the function $D(q_{\text{inv}})$ takes into account any non-femtoscopic correlations. The parameters $R_{\text{inv}(1,2)}$ and $\lambda_{(1,2)}$ describe the sizes of pion sources and the correlation strength, respectively.

For the "realistic" case with mixed reference distribution we first approximate the non-femtoscopic correlations $CF(p_1, p_2) = A(p_1, p_2)/B(p_1, p_2)$ by a polynomial $D(q_{\text{inv}}) = a + bq_{inv} + cq_{inv}^2$. The parameters a, b, c are then fixed and the full correlation function $CF(p_1, p_2) = A(p_1, p_2, w)/B(p_1, p_2)$ is fitted to Eq. (2) or Eq. (3). In order to reproduce the experimental fitting procedures we will use a flat baseline $D(q_{\text{inv}}) = 1$ for STAR energies, while for ALICE energies we can use either a flat or a polynomial baseline.

4. RESULTS AND CONCLUSIONS

The correlation functions of two identical charged pions have been calculated within the QGSM models in the mid-rapidity region. Calculations have been done for both the "ideal" and the "realistic" cases. We find that using the realistic case with a mixed pair reference distribution we get radii which are slightly larger than in the ideal case.

The obtained one-dimensional CFs are fitted to Eq. (2) and Eq. (3) in different k_T-ranges in Fig. 1 (200 GeV) and Fig. 2 (900 GeV). For 200 GeV the results are shown for both single and double-Gaussian fitting with $\kappa = 1.32$ GeV/fm. We see that the double-Gaussian describes the shape of the CF well. For 900 GeV our results can be compared to the experimental CF. Unlike in the experiments our baseline $D(q_{\text{inv}})$ is flat at low q_{inv} for all k_t-bins for both 200 GeV and 900 GeV. The reason for this is the absence of jets in the present version of QGSM. By varying κ one can get a good agreement with experiment. Results for $\kappa = 0.88$ GeV/fm and $\kappa = 2.64$ GeV/fm are shown in Fig. 2, with the latter giving best agreement with experiment.

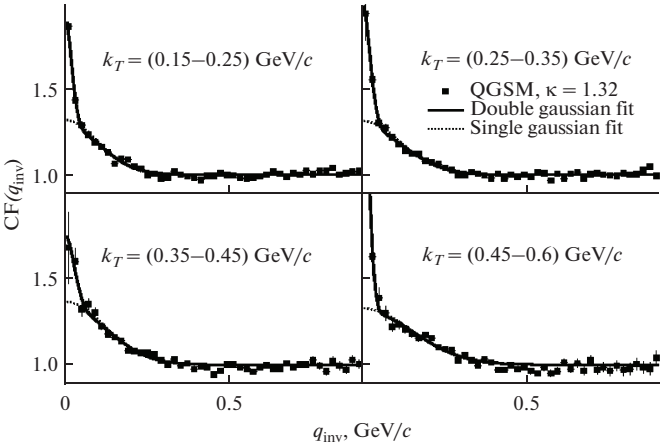

Fig. 1. The $\pi^+\pi^+$ CFs for pp at $\sqrt{s}$ = 200 GeV in four k_T bins, using mixed pair reference distribution. Cuts are $|\eta| < 0.5$ and $0.12\ \text{GeV}/c < p_T < 0.8\ \text{GeV}/c$. Calculations are performed with $\kappa = 1.32$ GeV/fm. Single-Gaussian and double-Gaussian fits are shown by dotted and full lines respectively.

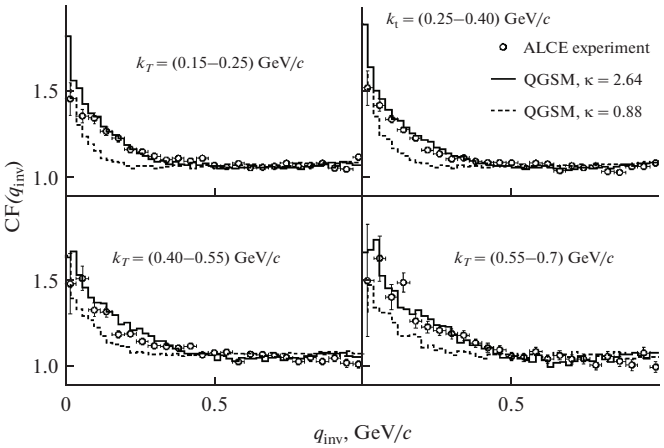

Fig. 2. The same as Fig. 1 but for $\sqrt{s}$ = 900 GeV/c. Cuts are $|\eta| < 0.8$ and $0.15\ \text{GeV}/c < p_T < 1.0\ \text{GeV}/c$. Calculations with $\kappa = 0.88$ GeV/fm (dashed line) and $\kappa = 2.64$ GeV/fm (full line) are compared to ALICE results [2] with multiplicity $7 \le M \le 11$.

The obtained R_{inv} fitting parameters are shown in Fig. 3. Radii from the single-Gaussian fit are close to experimental results. In order to make a model independent comparison, the standard single-Gaussian fit with *flat* baseline was chosen similar to that in STAR and ALICE experiments. Higher k_t-bins have smaller statistics, and larger deviation from experimental points.

The double-Gaussian fit gives us two sets of radii, $R_{\text{inv, 1}}$ which is lower than for a single-Gaussian, whereas $R_{\text{inv, 2}}$ is much larger. $R_{\text{inv, 1}}$ displays the radii of pions directly produced in the collision, while $R_{\text{inv, 2}}$ exhibits the radii of pions produced from resonance decays. This can be confirmed by selecting only either direct pions or pions from resonance decays in our simulated data. Both cuts give correlation functions

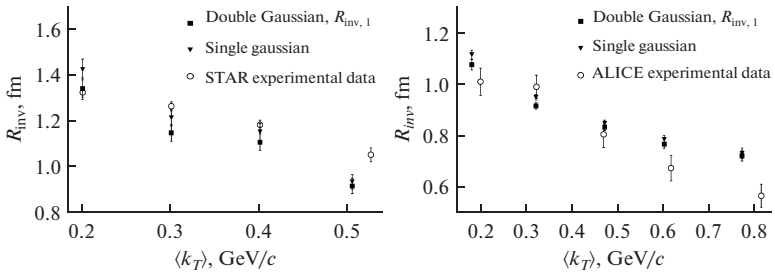

Fig. 3. The $\pi^+\pi^+$ correlation radii calculated by QGSM and compared with experimental data (STAR [1] and ALICE [2], flat baseline) at mid-rapidity in central *pp* collisions. We use $\kappa = 1.32$ GeV/fm for 200 GeV (left plot), and $\kappa = 2.64$ GeV/fm for 900 GeV (right plot).

that are well fitted to a single-Gaussian and give almost the same results as the two-Gaussian fit. The single-Gaussian fit, which does not include the low q_{inv} resonance peak, mostly describes the radii of direct pions and pions from short-lived resonances.

In conclusion, we find that the fitting values of both the STAR and ALICE experiments can be reproduced reasonably well by means of single-Gaussian fit. However the two-Gaussian fitting approach reproduces the correlation function better while retaining a physical interpretation of the extracted parameters. At 900 GeV the shape of the obtained correlation functions can be directly compared with experimental data. Better description of the data is demonstrated for the lower k_t-bins. To match the experimental results withing the framework of independent strings one has to increase the string tension from $\kappa = 1.32$ GeV/fm at $\sqrt{s} = 200$ GeV to $\kappa = 2.64$ GeV/fm at $\sqrt{s} = 900$ GeV. This can be taken as evidence for implementation of string-fusion processes in the model.

REFERENCES

1. J. Adams et al. (STAR Collab.), Phys. Rev. C **71**, 044906 (2005).
2. K. Aamodt et al. (ALICE Collab.), Phys. Rev. D **82**, 052001 (2010).
3. K. Werner et al., arXiv:1010.0400 [nucl-th].
4. J. Bleibel et al., arXiv:1011.2703 [hep-ph].

II

PHYSICAL REVIEW D **84,** 054006 (2011)

Study of $\pi\pi$ correlations at LHC and RHIC energies in pp collisions within the quark-gluon string model

M. S. Nilsson, L. V. Bravina, and E. E. Zabrodin*
Department of Physics, University of Oslo, PB 1048 Blindern, N-0316 Oslo, Norway

L. V. Malinina†
Skobeltzyn Institute for Nuclear Physics, Moscow State University, RU-119899 Moscow, Russia

J. Bleibel‡
Institut für Physik, WA 331, Johannes Gutenberg Universität Mainz, D-55099 Mainz, Germany
(Received 9 June 2011; published 12 September 2011)

The quark-gluon string model reproduces well the global characteristics of the pp collisions at energies of $\sqrt{s} = 200$ GeV (RHIC) and $\sqrt{s} = 900$ GeV (LHC). In present paper the quark-gluon string model is employed for the description of femtoscopic characteristics of identical pions produced in the aforementioned reactions. The study is concentrated on the low multiplicity and multiplicity averaged events, where no collective effects are expected. The different procedures for fitting the one-dimensional correlation functions of pions are studied and compared with the space-time distributions extracted directly from the model. Particularly, it is shown that the double-Gaussian fit reveals the contributions coming separately from resonances and from directly produced particles. The comparison of model results with the experimental data favors a decrease in particle formation time with rising collision energy.

DOI: 10.1103/PhysRevD.84.054006 PACS numbers: 25.75.Gz, 13.85.−t, 24.10.Lx

I. INTRODUCTION

Experiments at the Relativistic Heavy Ion Collider (RHIC) have demonstrated that hot and dense matter with partonic collectivity has been formed in ultrarelativistic Au + Au collisions at $\sqrt{s} = 200$ *A*GeV [1]. Proton-proton collisions are conventionally used as a reference to compare with nuclear collisions and to understand the observed collective effects. The new interest in general features of pp collisions at ultrarelativistic energies appeared after the first publications of Large Hadron Collider (LHC) data obtained in pp interactions at $\sqrt{s} = 900$ GeV and 7 TeV [2,3].

The Bose-Einstein enhancement in the production of two identical pions at low relative momenta was first observed in $\bar{p}p$ collisions about 50 years ago [4]. Since then, the developed correlation method, colloquially known at present as the ''femtoscopy technique,'' was successfully applied to the measurement of space-time characteristics of the production process at the distances of a few fermis (1 fm $= 10^{-15}$ m) (see, e.g., [5–7] and references therein). The space-time relative distances are ''measured'' by femtoscopy studies at the points where the particles stop to interact. This moment occurs at the very late stage of the collision, long after the quark-gluon plasma or any other exotic state of matter has disappeared. But signals like the geometric growth of the reaction zone and the specific features of the collective flow, generated by quark-gluon plasma pressure gradients, could be imprinted in the final state as very specific space-momentum correlations influencing particle spectra and femtoscopic radii.

The system created in ultrarelativistic pp collisions at RHIC and especially at LHC energies can be similar to the system created in noncentral heavy-ion collisions because of the large energy deposited in the overlapping region and therefore can also demonstrate collective behavior. The strong argument supporting this point of view comes from the observation of the almost identical multiplicity and momentum dependencies of the femtoscopic radii in pp and Au + Au collisions by the STAR collaboration at RHIC [8]. In particular, the transverse momentum dependence of the radii can be linked to the collective flow developed in the system [7]. The striking result obtained by the ALICE collaboration from study of the Bose-Einstein correlations in pp collisions at $\sqrt{s} = 900$ GeV [9] is the absence of the transverse momentum dependence, whereas the increase of correlation radii with rising multiplicity is similar to that observed in relativistic heavy-ion collisions at energies up to RHIC.

The aim of the present article is to study hadronization processes in pp collisions at ultrarelativistic energies using the momentum correlation technique within the Monte Carlo quark-gluon string model (QGSM) [10,11] and to compare results of calculations with the experimental data obtained at RHIC and LHC. This model describes

*Also at Skobeltzyn Institute for Nuclear Physics, Moscow State University, RU-119899 Moscow, Russia
†Also at Department of Physics, University of Oslo, PB 1048 Blindern, N-0316 Oslo, Norway
‡Also at Max-Planck-Institut für Intelligente Systeme, Heisenbergstr. 3, D-70569 Stuttgart, Germany

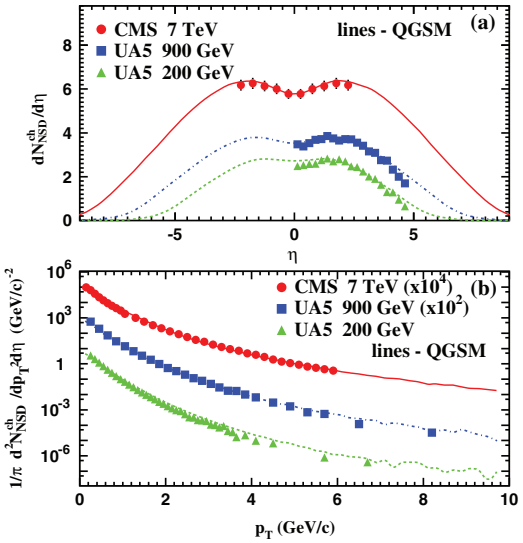

FIG. 1 (color online). (a) The charged particle pseudorapidity spectra and (b) their transverse momentum spectra in non-single-diffractive events calculated in QGSM for pp collisions at $\sqrt{s} =$ 200 GeV (dashed lines), 900 GeV (dash-dotted lines) and 7 TeV (solid lines). Symbols denote the experimental data taken from [2,3,30].

successfully the main characteristics of pp interactions, such as multiplicity, transverse momentum and (pseudo) rapidity distributions in a broad energy range from $\sqrt{s} =$ 200 GeV up to top LHC energy $\sqrt{s} = 7$ TeV [11]. We try to understand to what extent one is able to describe the correlation functions (CFs) in ultrarelativistic pp collisions within the pure string model picture.

The paper is organized as follows. A brief description of the model features is presented in Sec. II. Special attention is given to the concept of the formation time, which plays a very important role for study of the femtoscopy correlations. Section III introduces the method of correlation functions employed by both the STAR and the ALICE collaboration. Model results obtained for pp collisions at $\sqrt{s} = 200$ GeV and $\sqrt{s} = 900$ GeV are presented in Sec. IV. Comparison with the available experimental data is given as well. The proper choice of the baseline used in such measurements is discussed. The ability of the double-Gaussian fit to identify the contributions of string processes and resonances to the correlation functions is demonstrated. Finally, conclusions are drawn in Sec. V.

II. THE MODEL

A. Basic features

Our model is the Monte Carlo realization of the quark-gluon string model developed in [12]. Similarly to the dual parton model [13], QGSM is based on Gribov's Reggeon field theory (GRT) [14] accomplished by a string phenomenology of particle production in inelastic hadron-hadron collisions. The model incorporates the Field-Feynman algorithm [15] of string fragmentation. It enables one to consider emission of hadrons from both ends of the string with equal probabilities. As independent degrees of freedom QGSM includes octet and decuplet baryons, octet and nonet vector and pseudoscalar mesons, and their antiparticles. Pauli blocking is taken into account by excluding the already occupied final states from the available phase space.

Strings in the QGSM can be produced as a result of the color exchange mechanism or, like in diffractive scattering, due to momentum transfer. The Pomeron, which is a pole with an intercept $\alpha_P(0) > 1$ in the GRT, corresponds to the cylinder-type diagrams. The s-channel discontinuities of the diagrams, representing the exchange by n Pomerons, are related to the process of $2k(k \leq n)$ string production. If the contributions of all n-Pomeron exchanges to the forward elastic scattering amplitude are known, the Abramovskii-Gribov-Kancheli cutting rules [16] enable one to determine the cross sections for $2k$ strings. The hard gluon-gluon scattering and semihard processes with quark and gluon interactions are also incorporated in the model via the so-called hard Pomeron exchange [11,17], first discussed in [18]. The hard Pomeron is nowadays a standard feature attributed to a variety of GRT-based microscopic models, such as the dual parton model [13,19], PHOJET [20], QGSJET [21] and EPOS [22]. Its presence seems to be necessary to describe the rise of multiplicity at midrapidity and p_T spectra of secondaries in pp interactions at LHC energies within the QGSM [11]. Further details of the Monte Carlo version of QGSM and its extension to $A + A$ collisions can be found in [10,11,23].

Figure 1 displays the pseudorapidity and transverse momentum distributions of charged particles produced in nonsingle diffractive pp collisions at $\sqrt{s} = 200$ GeV, 900 GeV and 7 TeV, respectively. Experimental data are also plotted. Since the model reproduces the bulk characteristics of the collisions quite well, we are encouraged to apply the QGSM for the analysis of particle interferometry. Note, however, that the GRT does not provide the space-time picture of the system evolution, thus leaving room for the assumptions concerning the femtoscopy correlations quite open. Here one has to rely on approaches developed within the framework of the string phenomenology.

B. QGSM and particle coordinates

The space-time evolution of the collisions starts from the interacting partons, i.e., quarks, diquarks and sea quarks distributed randomly in the projectile-target overlapping region. The strings between them are stretching and subsequently decaying into hadrons. Because of the uncertainty principle it takes time to create a hadron from constituent

quarks. Also, hadrons are composite particles, and this circumstance makes the definition of the formation time model dependent. In the framework of the Lund string model [24] two definitions of the formation time or, equivalently, formation length are eligible [25]. In the "yo-yo" case it corresponds to the time/coordinate of the first intersection point of the hadron constituents ("yo-yo" formation time). In the so-called constituent case it corresponds to the time/coordinate of the point of rupture of the string (constituent formation time). In the present version of the QGSM the constituent formation time is used. The string length $L = M_s/2\kappa$ depends on its mass M_s and on the string tension κ. The mass of the string is not fixed. It is determined by the generation of longitudinal and transverse momenta of valence quarks at the string ends, that depend on the momenta of colliding hadrons. The length of the string varies from the maximum value determined by the momentum of the incident hadron to the minimum value determined by the pion mass. Therefore, for the formation of a resonance the mass and length of the string must be much larger than for production of a pion.

The formation time t_i^* and coordinate z_i^* of ith hadron in the string center of mass can be expressed via its energy E_i^*, its longitudinal momentum p_{zi}^* and the longitudinal momenta/energies of all hadrons produced by the decay of this string (see *Appendix*)

$$t_i^* = \frac{1}{2\kappa}\left(M_s - 2\sum_{j=1}^{i} p_{zj}^*\right), \tag{1}$$

$$z_i^* = \frac{1}{2\kappa}\left(M_s - 2\sum_{j=1}^{i} E_j^*\right). \tag{2}$$

Then we calculate t_i in the laboratory frame and make the propagation of the coordinates to this point (x_i, y_i, z_i, t_i): $a_i = a_{0i} + t_i p_{ai}/E_i$, $a = x, y, z$. The initial spatial distribution of partons in a proton is found to be insignificant for the pion coordinate distributions at freeze-out, which are dominated by both the formation time of hadrons and decay lengths of resonances. To study the possible reduction of the formation time because of, e.g., increase of the string tension with rising incident energy we introduce in Eqs. (1) and (2) the scaling parameter α, i.e., $\kappa = \alpha\kappa_0$, where $\kappa_0 = 0.88$ GeV/fm is the default value of the string tension coefficient in the QGSM found from comparison with experimental data at lower energies [10]. The coordinate distributions of pions at freeze-out are shown in Fig. 2 for pp collisions at $\sqrt{s} = 900$ GeV with $\alpha = 1$, 1.5 and 3. One can see that increase of α makes the coordinate distributions narrower.

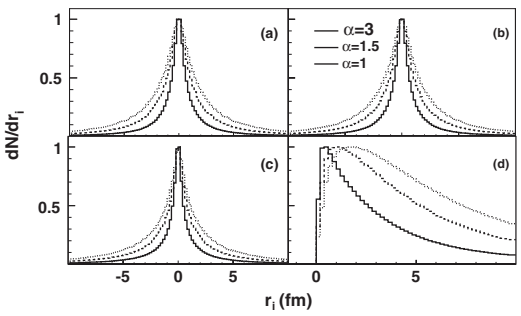

FIG. 2. The dN/dr_i, $r_i = x$ (a), y (b), z (c), t (d) distributions of pions at freeze-out in pp collisions at $\sqrt{s} = 900$ GeV with $\alpha = 1$ (dotted line), $\alpha = 1.5$ (dashed line) and $\alpha = 3$ (solid line).

III. THE CORRELATION FUNCTION REPRESENTATIONS

The momentum correlations are usually studied with the help of correlation functions of two or more particles. Particularly, the two-particle correlation function $\mathrm{CF}(p_1, p_2) = A(p_1, p_2)/B(p_1, p_2)$ is defined as a ratio of the two-particle distribution from the same event $A(p_1, p_2)$ to the reference one. In experimental analysis the reference distribution is typically constructed by mixing the particles from different events of a given class.

In our simulations the weight of each particle pair is calculated according to quantum statistics, using particle four-momenta p_i and four-coordinates x_i of the emission points: $w = 1 + \cos(q \cdot \Delta x)$, where $q = p_1 - p_2$ and $\Delta x = x_1 - x_2$. Note that the weight w used here has equally enhanced and reduced values. In this way quantities like the average multiplicity are not systematically affected by the weighting. The CF is here defined as a ratio of the weighted histogram of the pair kinematic variables to the unweighted one. This "ideal" case, $\mathrm{CF}_{\mathrm{ideal}}(p_1, p_2) = A(p_1, p_2, w)/A(p_1, p_2)$, uses unweighted pairs from the same events as the reference.

In experiments one utilizes unweighted mixed pairs from different events as the reference, namely $\mathrm{CF}_{\mathrm{realistic}}(p_1, p_2) = A(p_1, p_2, w)/B(p_1, p_2)$. Among other effects there is a difference between the ideal pair distribution $A(p_1, p_2)$ and the mixed one $B(p_1, p_2)$ due to the presence of energy-momentum conservation for the pairs from the same event and absence of it in pairs from the mixed ones. This causes a smooth increase of $\mathrm{CF}_{\mathrm{realistic}}$ with q, which reflects the fact that due to energy-momentum conservation the probability of two-particle emittence in the same direction is smaller than that in opposite directions. Therefore, a more complex fitting procedure is needed for the "realistic CF" than for the "ideal CF."

Generally, the correlations are measured as a function of pair relative momentum four vector q. An invariant form of this momentum difference commonly used in the one-dimensional correlation analysis is $q_{\mathrm{inv}} = \sqrt{q_0^2 - |q|^2}$. In both the STAR [8] and the ALICE [9] experiments the correlation function is fitted to a single-Gaussian

$$\mathrm{CF}_{\mathrm{single}}(q_{\mathrm{inv}}) = [1 + \lambda \exp(-R_{\mathrm{inv}}^2 q_{\mathrm{inv}}^2)]D(q_{\mathrm{inv}}), \tag{3}$$

where the function $D(q_{\rm inv})$ takes into account any non-femtoscopic correlations including the long-range correlations due to energy-momentum conservation described above. The parameters $R_{\rm inv}$ and λ describe the size of pion sources and the correlation strength, respectively. Here $R_{\rm inv}$ is defined in the pair rest frame (PRF). Concerning the fit given by Eq. (3) we have to note that the best way to compare the model simulations with the experimental data is the direct comparison of the correlation functions. Unfortunately, the CFs are not always available and one has to compare the results of the fit, that is more complicated. For instance, choice of the baseline $D(q_{\rm inv})$ is rather arbitrary. The baseline should describe the CF behavior at large $q_{\rm inv}$ where only the *conservation laws* work, but the region of small $q_{\rm inv}$ remains *terra incognita*. Different experiments employ different extrapolations of the baseline to small $q_{\rm inv}$, e.g., polynomial extrapolations, EMCIS-FIT [8], Monte Carlo simulations with PYTHIA and PHOJET [9], that give some specific behavior at small $q_{\rm inv}$ due to strong jet contribution in these models, especially noticeable at large k_t. In order to reproduce the experimental fitting procedures in a model independent way and make a consistent comparison of our simulations with different experiments we will use below a flat baseline with $D(q_{\rm inv}) = 1$ for STAR and ALICE data.

The correlation strength parameter λ can differ from unity due to the contribution of long-lived resonances, particle misidentification and coherence effects. The 1D correlation functions were studied within the different ranges of the average pair transverse momentum $k_T = |\vec{p}_{t,1} + \vec{p}_{t,2}|/2$ in the midrapidity region.

If large statistics sets are available it is possible to perform the 3D correlation analysis. Within realistic models, the directional and velocity dependence of the correlation function can be used to get information about both the duration of the emission and the form of the emission region, as well as to reveal the details of the production dynamics [5–7]. For these purposes the correlation functions can be analyzed in terms of the out, side and logitudinal components of the relative momentum vector $\mathbf{q} = \{q_{\rm out}, q_{\rm side}, q_{\rm long}\}$ [26,27]. Here $q_{\rm out}$ and $q_{\rm side}$ denote the transverse components of the vector $\mathbf{q}$, and the direction of $q_{\rm out}$ is parallel to the transverse component of the pair three-momentum. The corresponding correlation widths are usually parametrized in terms of the Gaussian correlation radii R_i

$$\mathrm{CF}(p_1, p_2) = 1 + \lambda \exp(-R_{\rm out}^2 q_{\rm out}^2 - R_{\rm side}^2 q_{\rm side}^2 - R_{\rm long}^2 q_{\rm long}^2). \quad (4)$$

The three-dimensional analysis is performed in the longitudinal comoving system (LCMS), where the pair momentum along the beam vanishes. It is possible to compare the radii measured in LCMS with $R_{\rm inv}$ by making a boost of all radii from LCMS to PRF, namely, $R_{\rm out\,PRF} = \gamma_T R_{\rm out}$, $R_{\rm side\,PRF} = R_{\rm side}$, $R_{\rm long\,PRF} = R_{\rm long}$ and averaging these radii.

The method used by STAR and ALICE experiments is to create a 3D correlation function by filling a three-dimensional histogram with the full $\mathbf{q} = \{q_{\rm out}, q_{\rm side}, q_{\rm long}\}$ vector in different ranges of the average pair transverse momentum $k_T = |\vec{p}_{t,1} + \vec{p}_{t,2}|/2$.

IV. RESULTS AND DISCUSSION

The two-pion correlation functions $\mathrm{CF}(q_{\rm inv})$ simulated for pp collisions within the QGSM model with the scaling parameters $\alpha = 1, 2$ and 3 are shown in different k_T ranges in Fig. 3 and 4 for $\sqrt{s} = 200$ GeV and $\sqrt{s} = 900$ GeV, respectively. The denominator of the CF was calculated by means of the mixing procedure described in Sec. III. As expected, smaller formation times lead to smaller freeze-out radii of the particle sources and, therefore, to

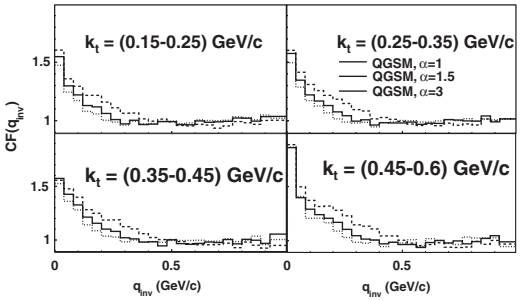

FIG. 3. The $\pi^+\pi^+$ CFs for pp at $\sqrt{s} = 200$ GeV in four k_T bins obtained by mixed pair reference distribution. Cuts are $|\eta| < 0.5$ and $0.12\ \mathrm{GeV}/c \leq p_T \leq 0.8\ \mathrm{GeV}/c$, as in the STAR experiment. Calculations are performed with $\alpha = 1$ (dotted line), $\alpha = 1.5$ (solid line) and $\alpha = 3$ (dashed line).

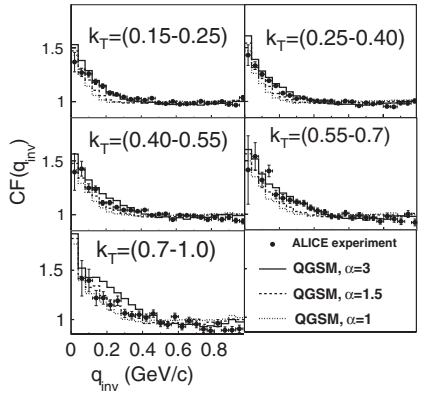

FIG. 4. The same as Fig. 3 but for $\sqrt{s} = 900\ \mathrm{GeV}/c$. Cuts are $|\eta| < 0.8$ and $0.15\ \mathrm{GeV}/c \leq p_T \leq 1.0\ \mathrm{GeV}/c$. Calculations with $\alpha = 1$ (dotted line), $\alpha = 1.5$ (dashed line) and $\alpha = 3$ (solid line) are compared to ALICE results [9] with multiplicity $M \leq 6$.

larger CFs in the interval $0 \leq q_{\rm inv} \leq 0.5$ GeV/c. In Fig. 4 the correlation functions obtained with the QGSM are directly compared to those measured by the ALICE collaboration. The ALICE analysis performed for the minimum bias event sample gives for the value of the average pseudorapidity density $\langle dN_{\rm ch}/d\eta \rangle = 3.6$, that coincides with the results of the QGSM simulations. We compare the QGSM low multiplicity sample with the ALICE data at low multiplicity bin $M \leq 6$. The best description is achieved for the scaling parameter equal to 3. In Fig. 4 one can see that the agreement between the shapes of the correlation functions calculated within the QGSM and measured by the ALICE is rather good till $k_T < 0.7$ GeV/c. In the last k_T bin $0.7 \leq k_T \leq 1.0$ GeV/c the experimental correlation function is about 15% narrower than the QGSM one. To understand this effect better the realistic correlation functions without quantum statistics weights, i.e."baselines'', were constructed in different k_T bins as displayed in Fig. 5. The energy-momentum conservation produces the long-range correlation effects at large $q_{\rm inv}$, for which the calculated values of the CFs lie above the unity. In Ref. [9] a good description of the long-range correlations was obtained within the PYTHIA and PHOJET models. In Fig. 5 the QGSM baseline $D(q_{\rm inv})$ demonstrates complicated behavior qualitatively similar to that of the PYTHIA/PHOJET baselines but a bit flatter in low $q_{\rm inv}$ interval for large k_T bins.

Figure 6 presents the k_T dependence of $R_{\rm inv}$ obtained from the fit to Eq. (3) with the flat baseline of the QGSM CFs, shown in Figs. 3 and 4. The available STAR and ALICE data points with flat baselines [8,9] are averaged over the multiplicity and compared with the multiplicity averaged QGSM correlation functions. The best agreement with the STAR data [8] was obtained for calculations with $\alpha = 1.5$.

It was reported in [9] that if PHOJET/PYTHIA baselines are chosen the correlation radii are practically independent on k_T within the studied transverse momentum range, however, the strength of the k_T dependence relies heavily on the baseline hypothesis. The ALICE conclusion about the absence of k_T dependence is based on the assumption that both PHOJET and PYTHIA correctly describe the nonfemtoscopic effects at low $q_{\rm inv}$ possibly related to minijets. In this case the enhancement at low $q_{\rm inv}$ in the large k_T bins is misinterpreted as Bose-Einstein enhancement. We see, however, that by assigning Bose-Einstein weights to all pion pairs we are able to reproduce the enhancement at low-$q_{\rm inv}$ shown in Fig. 4. In such a case it will be improper to use the PHOJET/PYTHIA or our own QGSM baseline to exclude the assumed nonfemtoscopy correlations at low $q_{\rm inv}$. The rather successful description of the ALICE points within such an approach suggests that there is no room for nonfemtoscopic correlations at low $q_{\rm inv}$ up to $k_T < 0.7$ GeV/c.

The ALICE and STAR data points obtained with the flat baseline reveal a similar slope in Fig. 6, which is described rather well by the QGSM calculations with the scaling factors $\alpha = 1.5$ and $\alpha = 3$, respectively. However, the higher k_T bins have larger deviations from the experimental points.

It is helpful to understand the origin of the strong k_T dependence of the correlation radii in the QGSM model. The Lund hadronization schema described by Eqs. (1) and (2) introduces automatically the space-momentum correlations. The "p-x" correlations for the direct pions displayed in Fig. 7 look similar to the space-momentum correlations in hydrodynamic models, where they arise

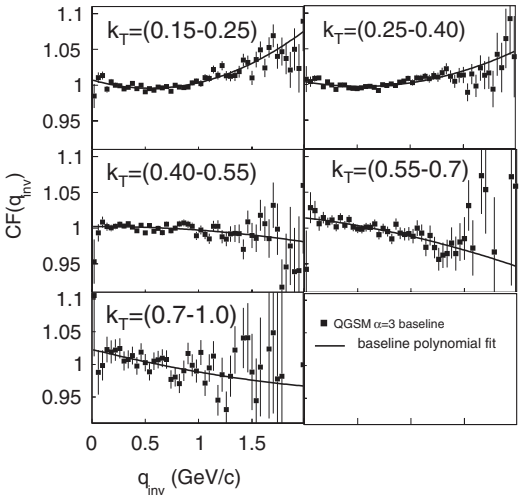

FIG. 5. The baseline for $\pi^+\pi^+$ correlation functions extracted from QGSM calculations (full circles) of pp collisions at $\sqrt{s} = 900$ GeV in different k_T intervals. Solid lines denote the fit to polynomial $D(q_{\rm inv}) = a + bq_{\rm inv} + cq_{\rm inv}^2$.

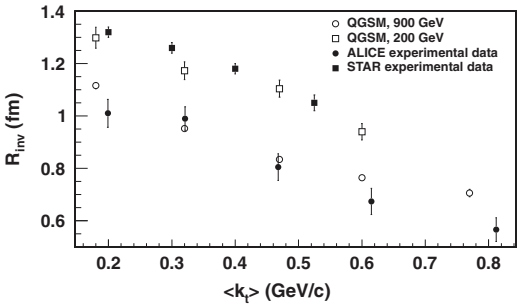

FIG. 6. One-dimensional $\pi^+\pi^+$ correlation radii as functions of k_T in pp collisions at $\sqrt{s} = 200$ GeV (squares) and $\sqrt{s} = 900$ GeV (circles). Open symbols denote STAR [8] and ALICE [9] experimental data, full symbols present QGSM calculations with $\alpha = 1.5$ (200 GeV) and $\alpha = 3.0$ (900 GeV), respectively. Both the model results and the data are obtained from the fit to Eq. (3) with the flat baseline.

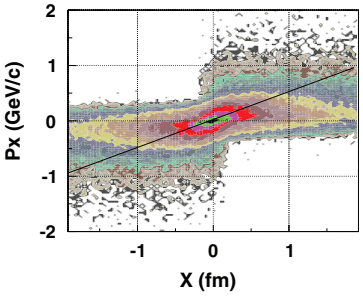

FIG. 7 (color online). The space-momentum correlations of direct pions produced in QGSM calculated pp collisions at $\sqrt{s} = 900$ GeV. Line is drawn to guide the eye.

due to transverse collective flow. Note that only the particles with nearby velocities in their center-of-mass system contribute to the correlation function. If the "p-x" correlations are absent, the whole source is "seen" by the CF in any chosen k_T range. Thus, there should be no k_T dependence of the correlation radii. In the presence of the "p-x" correlations the particles with close momenta come from nearby space regions of the source. Therefore, one is measuring not the real geometrical size of the source, but rather the size of the regions which emit particles of a given momenta, the so-called regions of homogeneity [28]. Higher k_T pairs should have narrower coordinate distributions due to larger "focusing effect". It originates from the fact that particles with large momenta fly away from each other much quicker than particles with small momenta, so in order to be correlated they have to be very close in the coordinate space. In Fig. 8(a) and 8(b) the transverse coordinate distributions are shown in the pair rest frame together with the corresponding correlation functions $\mathrm{CF_{ideal}}$ for the direct pions in three k_T ranges, namely KT1 = (0.1–0.25) GeV/c; KT3 = (0.4–0.55) GeV/c and KT5 = (0.7–1.0) GeV/c. We see that the widths of the X_{PRF} distributions decrease with rising k_T and the corresponding $\mathrm{CF_{ideal}}$ become narrower. These widths are reproduced within error bars by the fit of $\mathrm{CF_{ideal}}$ to the Gaussian given by Eq. (3) with $D(q_{\mathrm{inv}}) = 1$.

The important factor influencing the coordinate distributions is the ratio of direct pions to pions from resonance decay. Table I presents the fractions of pions from decay of the resonances most essentially contributed to the correlation functions. The path length $l^* \simeq p_d/m_\pi\Gamma$ of these states in the c.m. frame of two identical pions at small value of q_{inv} is listed in Table I also. Here p_d is the momentum of the decay pion in the resonance rest frame [29], m_π is the pion mass and Γ is the decay width. The pions from the decays of rather long-lived resonances ω and K^* cause appearance of the exponential tails in the pion emission function, which distorts the Gaussian-like shape of the CF,

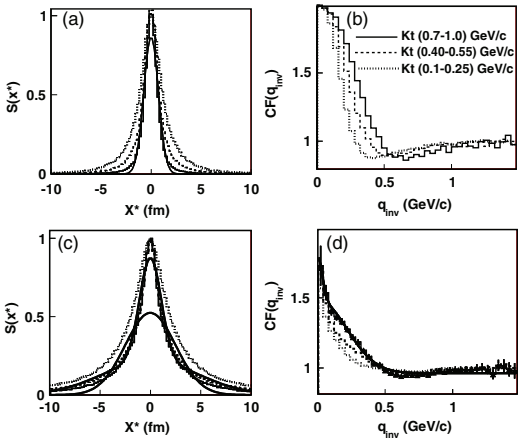

FIG. 8 (color online). (a) Coordinate distributions of the direct pions in PRF in QGSM calculated pp collisions at $\sqrt{s} = 900$ GeV with $\alpha = 3$. The three transverse momentum intervals are KT1 = (0.1–0.25) GeV/c (dotted histogram), KT3 = (0.4–0.55) GeV/c (dashed histogram) and KT5 = (0.7–1.0) GeV/c (solid histogram). The single-Gaussian fit for the KT5 bin is shown by the solid line. (b) $\mathrm{CF_{ideal}}$ for KT1 (dotted histogram), KT2 (dashed histogram) and KT3 (solid histogram). (c) The same as (a) but for all pions, the single and the double-Gaussian fits are shown for KT5 bin by the solid lines. (d) The same as (b) but for all pions, the double-Gaussian fit is shown for KT5 bin by the solid line.

see Fig. 8(c) and 8(d). Their relative contribution decreases with increasing k_T due to kinematical reasons, whereas the relative contributions of direct pions and pions from ρ decays increase as displayed in Fig. 9. This effect also leads to decrease of the correlation radii with increasing k_T. The essentially non-Gaussian coordinate distributions that include contributions from resonances cannot be fitted well to a single Gaussian, however, the double-Gaussian fit reproduces its shape properly, see Fig. 8(c). By fitting the corresponding CFs to a single Gaussian one cannot describe the narrow peak produced by pions from the resonance decays at low q_{inv}. On the other hand, using the double-Gaussian fitting procedure similar to the one suggested in [29]

TABLE I. The fraction of pions from decay of main resonance species in QGSM and the path length l^* of these states.

	l^* (fm)	200 GeV	900 GeV
Direct π^+	⋯	46.9%	37.5%
π^+ from $\rho^{0,+} \to \pi^{-,0}\pi^+$	3.3	37.1%	40.7%
π^+ from $\omega \to \pi^0\pi^-\pi^+$	28.1	11.2%	15.9%
π^+ from $K^{*,+}(\bar{K}^{*,0}) \to K\pi^+$	8.0	4.2%	5.5%

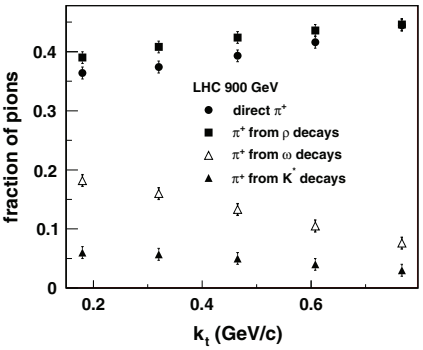

FIG. 9 (color online). The fractions of pions coming from resonance decays and direct ones as functions of the average pair momentum k_T in QGSM calculated pp collisions at $\sqrt{s} = 900$ GeV. The symbols denote directly produced pions (full circles) and pions coming from the decays of ρ mesons (full squares), ω mesons (open triangles) and K^* (full triangles), respectively.

$$\mathrm{CF}_{\mathrm{double}}(q_{\mathrm{inv}}) = [1 + \lambda_1 \exp(-R^2_{\mathrm{inv},1} q^2_{\mathrm{inv}}) + \lambda_2 \exp(-R^2_{\mathrm{inv},2} q^2_{\mathrm{inv}})] D(q_{\mathrm{inv}}), \quad (5)$$

where parameters $R_{\mathrm{inv}(1,2)}$ and $\lambda_{(1,2)}$ describe the sizes and the correlation strengths of the direct pion source and the one of the pions from the resonance decays, respectively, one gets a much better description of the CF shape at low q_{inv}, as shown in Fig. 8(d).

In order to understand to what extent one is able to describe the correlation functions of all particles including the resonances by the different fitting procedures we make a comparison of the extracted values of R_{inv} with the

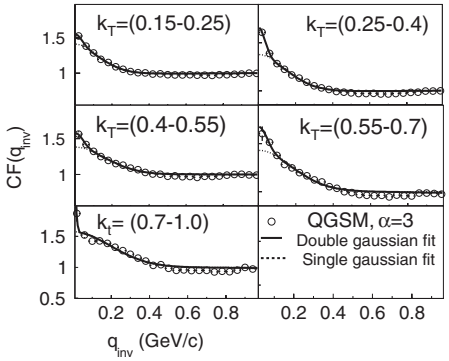

FIG. 10. The fit of pion correlation functions, obtained in QGSM calculated pp collisions at $\sqrt{s} = 900$ GeV with $\alpha = 3$, to single Gaussian (dotted line) and double Gaussian (solid line) in five k_T bins.

TABLE II. Gaussian widths $\sigma X^{\mathrm{all}}_{\mathrm{PRF}}$ of the coordinate distributions in PRF shown in Fig. 8(c) for single and double-Gaussian fit in three transverse momentum intervals $0.1 \le k_T \le 0.25$ GeV/c (KT1), $0.4 \le k_T \le 0.55$ GeV/c (KT3) and $0.7 \le k_T \le 1.0$ GeV/c (KT5), respectively.

	$\sigma X^{\mathrm{all}}_{\mathrm{PRF}}$ (fm)		
Method	KT1	KT3	KT5
single-Gaussian	3.37	2.45	2.96
double-Gaussian	1.48	1.08	1.00
	5.35	4.72	4.23

Gaussian widths of the coordinate distributions in the pair rest frame. The comparison is presented in Fig. 8(c) for the ideal correlation functions $\mathrm{CF}_{\mathrm{ideal}}$ and in Fig. 10 for the realistic CFs. The extracted parameters are listed in Table II and III, respectively, for three k_T ranges, namely, KT1 = (0.1–0.25) GeV/c; KT3 = (0.4–0.55) GeV/c and KT5 = (0.7–1.0) GeV/c. Because of the sharp peak of the correlation functions at low q_{inv} the two radii restored by the double-Gaussian fit vary considerably. The first one is of the order of 1 fm and has a tendency to decrease with rising k_T, whereas the second one is always larger than 3 fm and increases to 13–14 fm at high transverse momenta. The second Gaussian is quite narrow thus leading to a hair-width difference between the single-Gaussian and double-Gaussian curves at $q_{\mathrm{inv}} > 0.1$ GeV/c.

The ideal 3D correlation functions for $\sqrt{s} = 200$ GeV and $\sqrt{s} = 900$ GeV, constructed for the minimum bias events and low multiplicity bin, are displayed in Fig. 11 and 12, respectively. The calculations were done with $\alpha = 1.5$ and $\alpha = 3.0$, and the full 3D fit to the 3D Gaussian given by Eq. (4) was performed. The extracted R_i as

TABLE III. Parameters R_{inv} extracted from Fig. 8(c) and 10 by using different fitting strategies: *1*—ideal CF is fitted to the single-Gaussian Eq. (3) with $D(q_{\mathrm{inv}}) = 1$; *2*—"realistic" CF is fitted to the single-Gaussian Eq. (3) with $D(q_{\mathrm{inv}}) = 1$; *3*—realistic CF is fitted to the single-Gaussian Eq. (3) with $D(q_{\mathrm{inv}}) = a + bq_{\mathrm{inv}} + cq^2_{\mathrm{inv}}$; *4*—realistic CF is fitted to the double-Gaussian Eq. (5) with $D(q_{\mathrm{inv}}) = 1$; *5*—realistic CF is fitted to the double-Gaussian Eq. (5) with $D(q_{\mathrm{inv}}) = a + bq_{\mathrm{inv}} + cq^2_{\mathrm{inv}}$. The selected transverse momentum intervals are the same as in Table II.

	$R_{\mathrm{inv1(2)}}$ (fm)		
Method	KT1	KT3	KT5
1	1.00	0.77	0.66
2	1.26	0.84	0.71
3	1.10	0.84	0.71
4	1.23	0.81	0.71
	5.04	3.26	13.97
5	1.05	0.81	0.71
	3.61	3.25	13.83

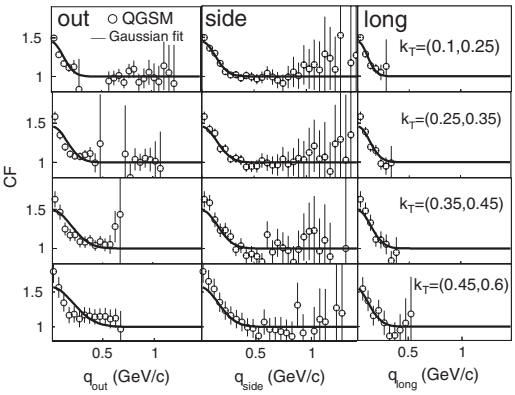

FIG. 11. Projections of the 3D Cartesian representations of the correlation functions onto the $q_{\rm out}$, $q_{\rm side}$, and $q_{\rm long}$ axes, for the minimum bias events from pp collisions at 200 GeV for four k_T ranges. To project onto one q component, the others are integrated over the range $0 \le q_i \le 0.12$ GeV$/c$.

functions of average k_T are presented in Fig. 13 and 14. One can see that the experimental points are rather close to the QGSM ones especially for ALICE experimental data, see Fig. 14, where the low multiplicity bin is considered. Note that no integration over multiplicity was done in both cases. At 200 GeV all radii demonstrate the weak decrease with k_T, whereas at 900 GeV the radii $R_{\rm out}$ and $R_{\rm side}$ are rather flat, the first point in $R_{\rm out}$ is lower than the other ones, and only $R_{\rm long}$ demonstrates the decrease with rising k_T as was observed by the ALICE collaboration at low multiplicity.

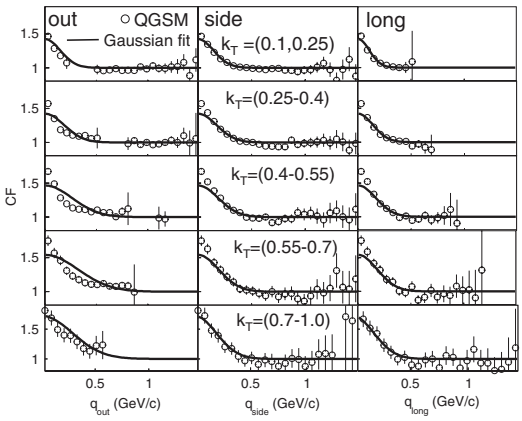

FIG. 12. The same as Fig. 11 but for the low multiplicity bin $N_{\rm ch} < 11$ of pp collisions at 900 GeV in five k_T ranges.

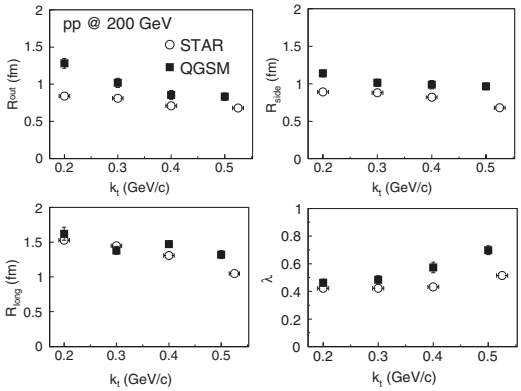

FIG. 13. Three-dimensional $\pi^+\pi^+$ correlation radii as functions of k_T in pp collisions at $\sqrt{s} = 200$ GeV for minimum bias events. Open circles denote STAR experimental data, full squares present QGSM calculations with $\alpha = 1.5$. Both the model results and the data are obtained from the fit to Eq. (4).

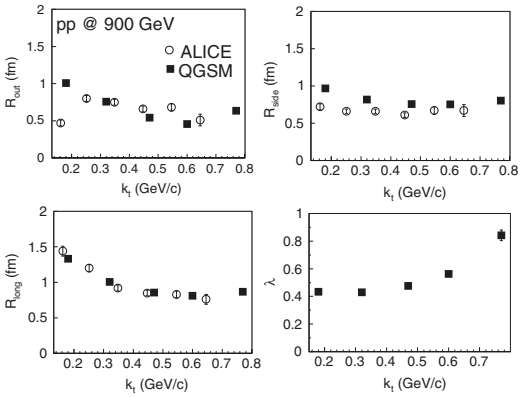

FIG. 14. The same as Fig. 13 but for the low multiplicity bin $N_{\rm ch} < 11$ of pp collisions at $\sqrt{s} = 900$ GeV. QGSM calculations are with $\alpha = 3$.

V. CONCLUSIONS

The following conclusions can be drawn from our study. QGSM calculations show strong dependence of the correlation radius on the transverse momentum of a pion pair. Similar dependence has been observed by the STAR Collaboration, while the ALICE Collaboration reported almost constant $R_{\rm inv}$ with increasing k_T. However, if the flat baseline is employed instead of the one simulated by PYTHIA and PHOJET, the ALICE data demonstrate the noticeable k_T dependence as well. The origin of such a dependence in the QGSM is traced to the space-momentum correlations attributed to microscopic string models. If these correlations

would be absent, the correlation radius $R_{\rm inv}$ would be independent on the pair transverse momentum.

Pions in the model are produced either directly in the processes of string fragmentation or from the decays of resonances. The relative contribution of the long-lived resonances to pion emission function decreases with rising k_T, while the corresponding contributions of direct processes and short-lived resonances increase. Therefore, the correlation radii of pions also decrease with an increase in the pair transverse momentum. The fit of the 1D correlation functions to the double Gaussian provides a good description of the shape of the CFs at low $q_{\rm inv}$ range and enables us to separate the contributions from the direct pions and pions from the resonances.

It was expected that the size of the freeze-out region in pp collisions should increase with rising c.m. energy from $\sqrt{s} = 200$ GeV to $\sqrt{s} = 900$ GeV due to the increase of interaction cross section and the number of produced resonances. Surprisingly, the radii measured by femtoscopy at $\sqrt{s} = 200$ GeV are the same or even smaller than the ones at $\sqrt{s} = 900$ GeV, as seen in Fig. 6. The radii obtained within the standard Lund scenario of string breaking and the constituent formation time, implemented in the QGSM, appear to be larger compared to the experimental data. Our analysis favors reduction of the formation time with increasing energy of hadronic collision. One of the possible solutions is the process of string-string interaction via, e.g., fusion of strings that leads to an increase of the string tension.

ACKNOWLEDGMENTS

Fruitful discussions with A. Kisiel, R. Kolevatov, K. Mikhailov and Yu. Sinyukov are gratefully acknowledged. This work was supported by the Norwegian Research Council (NFR) under Contract No. 185664/V30.

APPENDIX: SPACE-TIME COORDINATES OF PRODUCED HADRONS

Following Refs. [24,25] let us consider 1 + 1 fragmentation model of $q\bar{q}$ string of mass M_s with massless constituents at the ends, as displayed in Fig. 15. The Hamiltonian of such a system is

$$H = |p_1| + |p_2| + \kappa|z_1 - z_2|, \tag{A1}$$

where $|p_1|$ and $|p_2|$ are the momenta of the quark and antiquark, z_1 and z_2 are their coordinates, and κ is the string tension. The equation of motion for the constituents reads

$$\frac{dp}{dt} = \pm\kappa, \tag{A2}$$

with the sign depending on the direction of motion of the constituent. At a certain time t_i the string breaks via formation of $q_i\bar{q}_i$ pair. The final hadrons are produced as a result of $\bar{q}_{i-1}q_i$ coalescence. Their energy and momentum are

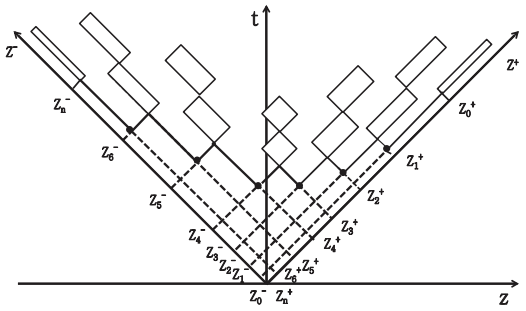

FIG. 15. Space-time evolution of the 1 + 1 dimensional Lund string. See text for details.

$$E_i = \kappa(z_{i-1} - z_i), \tag{A3}$$

$$p_i = \kappa(t_{i-1} - t_i), \tag{A4}$$

respectively. In terms of the light cone variables $p^{\pm} = E \pm p$, $z^{\pm} = t \pm z$ one gets for the ith hadron within the "constituent" picture of hadron formation

$$p_i^+ = \kappa(z_{i-1}^+ - z_i^+), \tag{A5}$$

$$p_i^- = \kappa(z_i^- - z_{i-1}^-). \tag{A6}$$

Therefore,

$$z_i^+ = -\frac{p_i^+}{\kappa} + z_{i-1}^+, \tag{A7}$$

$$z_i^- = \frac{p_i^-}{\kappa} + z_{i-1}^-. \tag{A8}$$

Applying the recurrence procedure to Eqs. (A7) and (A8) we arrive to

$$z_i^+ = -\frac{1}{\kappa}\sum_{j=1}^{i} p_j^+ + z_0^+, \tag{A9}$$

$$z_i^- = \frac{1}{\kappa}\sum_{j=1}^{i} p_j^- + z_0^-. \tag{A10}$$

Taking into account that $z_0^+ = (E_0 + p_0)/\kappa = M_s/\kappa$, whereas $z_0^- = 0$ we finally get expressions for the (t_i, z_i) coordinates of produced hadrons

$$z_i = \frac{1}{2\kappa}\left[M_s - \sum_{j=1}^{i}(p_j^+ + p_j^-)\right] = \frac{1}{2\kappa}\left[M_s - 2\sum_{j=1}^{i} E_j\right], \tag{A11}$$

$$t_i = \frac{1}{2\kappa}\left[M_s - \sum_{j=1}^{i}(p_j^+ - p_j^-)\right] = \frac{1}{2\kappa}\left[M_s - 2\sum_{j=1}^{i} p_j\right]. \tag{A12}$$

[1] I. Arsene *et al.* (BRAHMS Collaboration), Nucl. Phys. **A757**, 1 (2005); B. B. Back *et al.* (PHOBOS Collaboration), Nucl. Phys. **A757**, 28 (2005); J. Adams *et al.* (STAR Collaboration), Nucl. Phys. **A757**, 102 (2005); K. Adcox *et al.* (PHENIX Collaboration), Nucl. Phys. **A757**, 184 (2005).

[2] K. Aamodt *et al.* (ALICE Collaboration), Eur. Phys. J. C **68**, 89 (2010); **68**, 345 (2010); Phys. Lett. B **693**, 53 (2010).

[3] K. Khachatryan *et al.* (CMS Collaboration), J. High Energy Phys. 02 (2010) 041; K. Khachatryan *et al.* (CMS Collaboration), Phys. Rev. Lett. **105**, 022002 (2010).

[4] G. Goldhaber, S. Goldhaber, W.-Y. Lee, and A. Pais, Phys. Rev. **120**, 300 (1960).

[5] M. I. Podgoretsky, Fiz. Elem. Chastits At. Yadra **20**, 628 (1989), (in Russian).

[6] R. Lednicky, Phys. At. Nucl. **67**, 72 (2004).

[7] M. Lisa, S. Pratt, R. Soltz, and U. Wiedemann, Annu. Rev. Nucl. Part. Sci. **55**, 357 (2005).

[8] J. Adams *et al.* (STAR Collaboration), Phys. Rev. C **71**, 044906 (2005).

[9] K. Aamodt *et al.* (ALICE Collaboration), Phys. Rev. D **82**, 052001 (2010).

[10] N. S. Amelin and L. V. Bravina, Yad. Fiz. **51**, 211 (1990) [Sov. J. Nucl. Phys. **51**, 133 (1990)]; N. S. Amelin, L. V. Bravina, L. I. Sarycheva, and L. N. Smirnova, Yad. Fiz. **51**, 841 (1990) [Sov. J. Nucl. Phys. **51**, 535 (1990)].

[11] J. Bleibel, L. V. Bravina, A. B. Kaidalov, and E. E. Zabrodin, arXiv:1011.2703.

[12] A. B. Kaidalov, Phys. Lett. B **116**, 459 (1982); A. B. Kaidalov and K. A. Ter-Martirosyan, *ibid.* **117**, 247 (1982).

[13] A. Capella and J. Tran Thanh Van, Phys. Lett. B **93**, 146 (1980); A. Capella, U. Sukhatme, C.-I. Tan, and J. Tran Thanh Van, Phys. Rep. **236**, 225 (1994).

[14] V. N. Gribov, Sov. Phys. JETP **26**, 414 (1968); L. V. Gribov, E. M. Levin, and M. G. Ryskin, Phys. Rep. **100**, 1 (1983).

[15] R. D. Field and R. P. Feynman, Nucl. Phys. **B136**, 1 (1978).

[16] V. A. Abramovskii, V. N. Gribov, and O. V. Kancheli, Yad. Fiz. **18**, 595 (1973) [Sov. J. Nucl. Phys. **18**, 308 (1974)].

[17] N. S. Amelin, E. F. Staubo, and L. P. Csernai, Phys. Rev. D **46**, 4873 (1992).

[18] A. Capella, J. Tran Thanh Van, and J. Kwiecinski, Phys. Rev. Lett. **58**, 2015 (1987).

[19] J. Ranft, K. Hahn, P. Aurenche, P. Maire, F. W. Bopp, A. Capella, J. Tran Thanh Van, and J. Kwiecinski, Lawrence Berkeley Laboratory Report No. SSC-149, Berkeley, CA, 1987 (unpublished).

[20] R. Engel, J. Ranft, and S. Roesler, Phys. Rev. D **52**, 1459 (1995).

[21] S. Ostapchenko, Phys. Rev. D **83**, 014018 (2011).

[22] K. Werner, F.-M. Liu, and T. Pierog, Phys. Rev. C **74**, 044902 (2006).

[23] E. Zabrodin, C. Fuchs, L. Bravina, and Amand Faessler, Phys. Lett. B **508**, 184 (2001); E. Zabrodin, L. Bravina, C. Fuchs, and Amand Faessler, Prog. Part. Nucl. Phys. **53**, 183 (2004); G. Burau, J. Bleibel, C. Fuchs, Amand Faessler, L. V. Bravina, and E. E. Zabrodin, Phys. Rev. C **71**, 054905 (2005); J. Bleibel, G. Burau, and C. Fuchs, Phys. Lett. B **659**, 520 (2008).

[24] B. Andersson, G. Gustafson, G. Ingelman, and T. Sjostrand, Phys. Rep. **97**, 31 (1983).

[25] A. Bialas and M. Gyulassy, Nucl. Phys. **B291**, 793 (1987).

[26] M. I. Podgoretsky, Yad. Fiz. **37**, 455 (1983) [Sov. J. Nucl. Phys. **37**, 272 (1983)]; R. Lednicky, JINR Report No. B2-3-11460, 1978 (unpublished); P. Grassberger, Nucl. Phys. **B120**, 231 (1977).

[27] G. F. Bertsch, P. Danielewicz, and M. Herrmann, Phys. Rev. C **49**, 442 (1994); S. Pratt, in *Quark Gluon Plasma 2*, edited by R. C. Hwa (World Scientific, Singapore, 1995), p. 700; S. Chapman, P. Scotto, and U. Heinz, Phys. Rev. Lett. **74**, 4400 (1995).

[28] S. V. Akkelin and Yu. M. Sinyukov, Phys. Lett. B **356**, 525 (1995); Yu. M. Sinyukov, Nucl. Phys. **A566**, 589 (1994).

[29] R. Lednicky and T. Progulova, Z. Phys. C **55**, 295 (1992).

[30] G. J. Alner *et al.* (UA5 Collaboration), Phys. Rep. **154**, 247 (1987).

III

BULK OBSERVABLES, LONG-RANGE CORRELATIONS AND FLOW IN *pp* COLLISIONS AT LHC*

L. Bravina[a], R. Kolevatov[a], L. Malinina[a,b]
M.S. Nilsson[a], E. Zabrodin[a,b]

[a]Department of Physics, University of Oslo, PB 1048, 0316 Oslo, Norway
[b]Skobeltzyn Institute for Nuclear Physics, Moscow State University
119899 Moscow, Russia

(Received December 27, 2011)

Bulk observables like multiplicity, rapidity and transverse momentum distributions of hadrons produced both in inelastic and non-diffractive *pp* collisions at energies from $\sqrt{s} = 200$ GeV to 7 TeV are described within the Monte Carlo quark-gluon string model. The short-range correlations of particles in the strings and interplay between the multi-string processes at ultra-relativistic energies lead to violation of Feynman scaling at midrapidity. Model predicts strong increase of the slope with energy in forward–backward multiplicity dependence $\langle n_{\rm F}(n_{\rm B})\rangle$ due to long-range correlations between particles produced in the multi-string processes. The comparison of model results on pion–pion femtoscopic correlations with the experimental data favors significant decrease of particle formation time with rising collision energy. The possibility to produce anisotropic flow on the initial stages of *pp* reactions, both directed v_1 and elliptic v_2, from the decay of the strings is discussed.

DOI:10.5506/APhysPolBSupp.5.419
PACS numbers: 25.75.Gz, 24.10.Lx, 13.85.–t, 12.40.Nn

1. Introduction

One of the goals of CERN experiments at LHC is a search for signals of the hot and dense matter created in relativistic heavy ion collisions. The main signatures of such matter are considered to be *e.g.* jet quenching, strong anisotropic flow and ridge. These effects were found in Au + Au collisions at $\sqrt{s} = 200$ *A*GeV at RHIC. Similar effects, detected at LHC at energies of one order of magnitude higher, $\sqrt{s} = 2.76$ *A*TeV, showed that the density of the matter becomes larger, the particle multiplicities and magnitude of anisotropic flow are growing gradually but not very significantly. High

* Presented at the Conference "Strangeness in Quark Matter 2011", Kraków, Poland, September 18–24, 2011.

multiplicity pp data at $\sqrt{s} = 7$ TeV reveal the presence of near-side ridge similar to that detected in Au–Au collisions at RHIC. They also show the possible existence of radial flow in identified particle p_{T} spectra, dependent on m_{T} of the particle, which was supported by femtoscopic radii of the particles. The scientists put forward the idea that hot and dense matter with very particular properties can be created also in central pp collisions at very high energies. For theoretical models it means that these collective effects in pp collisions can be described by hydrodynamics, usually applied only to nucleus–nucleus collisions, where the matter with many degrees of freedom is formed. The question arises whether it can also be explained by initial state effects as was suggested within the Gribov's Reggeon Field Theory (GRT) [1]. In the present paper, we discuss the predictions of Quark Gluon String Model (QGSM) [2] for pp collisions at RHIC and LHC energies. The QGSM is based on the GRT accomplished by the string phenomenology. Its brief description is given in the next section.

2. Basic features of the model

The QGSM is based on the $1/N$ expansion, where N is number of colors or flavors, of the amplitude for a QCD process. The diagrams arising in this approach correspond to processes with the exchange of Regge singularities in the t-channel and, therefore, can be calculated within the perturbative GRT. The theoretically obtained statistical weights, structure functions of hadrons and fragmentation functions of leading quarks are utilized in the present Monte Carlo version of the QGSM [3] to choose the subprocesses of hadronic interactions, to calculate the mass and momentum of each string and, finally, to simulate the string fragmentation into hadrons.

As independent degrees of freedom the QGSM includes the nonets of vector and pseudoscalar mesons, the baryon octet and decuplet, and their antistates. Pauli blocking of occupied final states is implemented by excluding the already occupied final states from the available phase space. Strings in the QGSM can be produced as a result of both the momentum transfer (diffraction) and color exchange mechanism. The Pomeron, which is a pole with an intercept $\alpha_{\mathbb{P}}(0) > 1$ in the GRT, corresponds to the cylinder-type diagrams. The s-channel discontinuities of the diagrams, representing the exchange by n-Pomerons, are related to process of $2k$ ($k \leq n$) string production. If the contributions of all n-Pomeron exchanges to the forward elastic scattering amplitude are known, the AGK cutting rules [4] enable one to determine the cross sections for $2k$-strings. The hard gluon–gluon scattering and semi-hard processes with quark and gluon interactions are also incorporated in the model via the so-called hard Pomeron exchange. Its presence seems to be necessary to describe the rise of multiplicity at midrapidity and p_{T} spectra of secondaries in pp interactions at LHC within the QGSM [5].

For the modeling of string fragmentation the Field–Feynman algorithm [7] is employed. It enables one to consider emission of hadrons from both ends of the string with equal probabilities. The break-up procedure invokes the energy-momentum conservation and the preservation of the quark numbers. Due to the uncertainty principle it takes some time to create a hadron from constituent quarks, *e.g.*, fast particles are created the last. In string models two definitions of formation time are accepted [8]: the time when the string is broken and all constituents of the hadron are created (constituent) or the time when the trajectories of hadron constituents (quarks) cross ("yo–yo"). In this version of QGSM we are using the constituent formation time. Further details of the MC version of QGSM and its extension to $A + A$ collisions can be found in [3, 5, 6].

3. Pseudorapidity and transverse momentum distributions

For the comparison with model calculations the experimental data reported for pp and $\bar{p}p$ collisions in [9, 10, 11, 12, 13] are used. Pseudorapidity distributions of charged particles obtained for inelastic and non-single diffraction (NSD) pp interactions at energies from $\sqrt{s} = 200\,\text{GeV}$ to $14\,\text{TeV}$ are presented in Fig. 1 (a) together with the available experimental data. According to the hypothesis of Feynman scaling the density of charged particles $dN^{\text{ch}}/d\eta$ at midrapidity should be saturated at very high energies. This scaling regime is obviously not reached yet. Moreover, at LHC energies $dN^{\text{ch}}/d\eta\,|_{\eta=0}$ demonstrates a non-linear rise with $\ln s$, as suggested by the saturation of the Froissart bound. For pp collisions at top LHC energy $\sqrt{s} =$ 14 TeV the QGSM predicts $dN_{\text{inel}}/d\eta\,|_{\eta=0} = 6.1$, $dN_{\text{NSD}}/d\eta\,|_{\eta=0} = 7.0$, respectively.

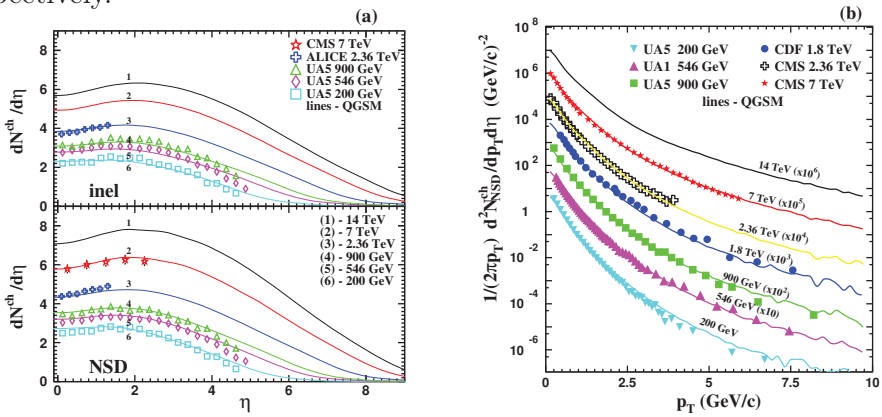

Fig. 1. (Color online) (a) Pseudorapidity spectra for charged particles in inelastic and NSD pp collisions at 200 GeV $\leq \sqrt{s} \leq$ 14 TeV. (b) Transverse momentum distribution of the invariant cross section in NSD pp collisions in the same energy range.

Figure 1 (b) shows the transverse momentum distribution of the invariant cross sections of charged particles in NSD pp events. The contribution of hard processes increases with rising $\sqrt{s}$, therefore, the $p_{\rm T}$ spectra of secondaries become harder, especially at $p_{\rm T} \geq 2.5$ GeV/c. The average transverse momentum of the produced hadrons also increases. For the NSD pp collisions at $\sqrt{s} = 14$ TeV the model predicts $\langle p_{\rm T} \rangle = 0.56 \pm 0.03$ GeV/c.

4. Long-range and femtoscopy correlations

The term "long-range correlations" is used for correlations between charged particles emitted in forward (F) and backward (B) hemispheres. These correlations were first observed experimentally in [9]. The dependencies $\langle n_{\rm B}(n_{\rm F}) \rangle$ of the mean charged-particle multiplicities measured in the pseudorapidity intervals $-4 \leq \eta \leq 0$ and $0 \leq \eta \leq 4$ are shown in Fig. 2 for pp collisions at four different energies. We see good agreement between the model results and the available experimental data. Also, these dependencies are quite linear

$$\langle n_{\rm B}(n_{\rm F}) \rangle = a + b\, n_{\rm F}\,, \tag{1}$$

whereas the slope parameter b increases with the rising energy. Note that hard processes do not alter the observed correlations, *i.e.* the strength of the correlations is fully determined by the processes with increasing number of soft Pomerons.

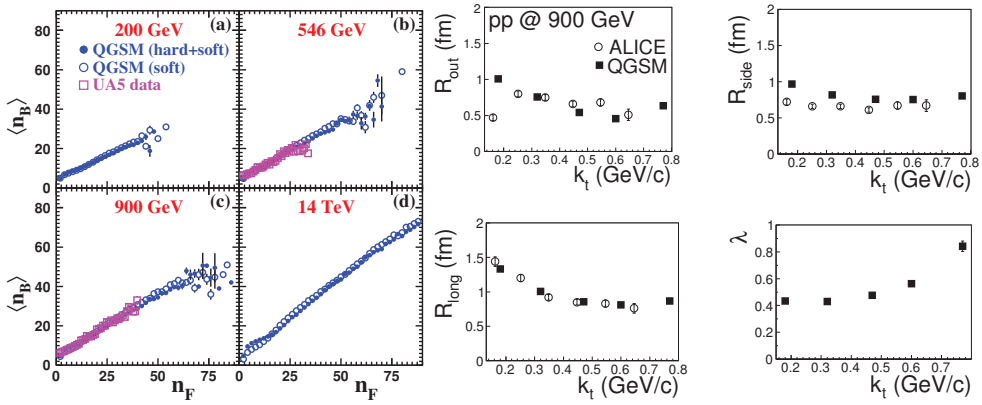

Fig. 2. (Color online) Left: Backward–forward multiplicity correlations $\langle n_{\rm B}(n_{\rm F}) \rangle$ for $0 \leq |\eta| \leq 4$ in NSD pp interactions at $\sqrt{s} = 200$ GeV, 546 GeV, 900 GeV and 14 TeV. Open circles denote contributions of soft processes, full symbols are for all processes, open squares represent UA5 data. Right: Three-dimensional $\pi^+\pi^+$ correlation radii as functions of $k_{\rm T}$ in pp collisions at $\sqrt{s} = 900$ GeV for minimum bias events. Open circles denote ALICE experimental data, full squares present QGSM calculations.

The 3D femtoscopy correlation analysis can provide information about both the form of the emitting source and the duration of the emission [14,15]. Here, the momentum correlation functions are analyzed in terms of the *out*, *side* and *longitudinal* components of the relative momentum vector $\boldsymbol{q} = \{q_{\rm out}, q_{\rm side}, q_{\rm long}\}$, where $q_{\rm out}$ and $q_{\rm side}$ denote the transverse components of the vector $\boldsymbol{q}$, and the direction of $q_{\rm out}$ is parallel to the transverse component of the pair three-momentum. The corresponding correlation widths are usually parametrized in terms of the Gaussian correlation radii

$$\mathrm{CF}(p_1, p_2) = 1 + \lambda \exp\left(-R^2_{\rm out} q^2_{\rm out} - R^2_{\rm side} q^2_{\rm side} - R^2_{\rm long} q^2_{\rm long}\right). \qquad (2)$$

The extracted R_i as functions of average pair transverse momentum $k_{\rm T} = |\vec{p_{\rm t,1}} + \vec{p_{\rm t,2}}|/2$ are presented in Fig. 2 (b) for the low multiplicity bin in *pp* interactions at $\sqrt{s} = 900$ GeV. One can see that the QGSM points are rather close to the ALICE experimental ones [16]. However, this implies significant reduction of the formation time with increasing energy [17] or, equivalently, rise of the string tension.

5. Directed and elliptic flow in *pp* collisions

The possible formation of anisotropic flow or rather its two first components, directed v_1 and elliptic v_2 flow, in *pp* collisions at LHC energies is a very popular topic nowadays. Several scenarios have been discussed

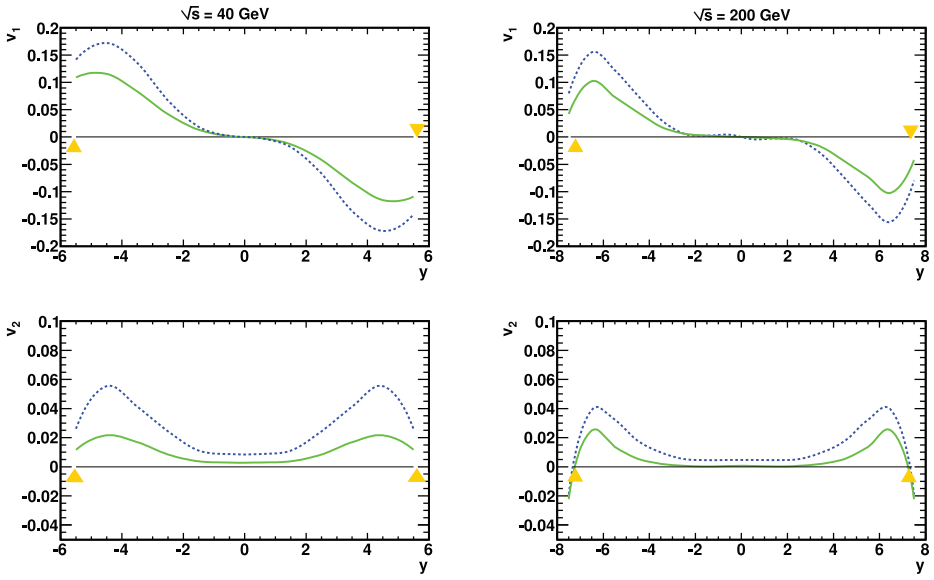

Fig. 3. (Color online) Flow coefficients v_1 and v_2 obtained for a decay of a string with energy $\sqrt{s} = 40$ GeV and 200 GeV and with impact parameters $b = 0.5$ fm (solid lines) and $b = 1.0$ fm (dashed lines).

(see *e.g.* [18] and references therein). In the color exchange mechanism of string excitation, strings are stretching between constituents belonging to different hadrons. Therefore, these strings usually have some slopes in the transverse direction. In [19] the fragmentation of a classical relativistic string with a certain transverse separation of the ends has been considered. It was shown that the fragmentation process of such a string could generate both directed and elliptic flow as displayed in Fig. 3.

This work was supported by the Norwegian Research Council (NFR) under Contract No. 185664/V30.

REFERENCES

[1] V. Gribov, *Sov. Phys. JETP* **26**, 414 (1968); L.V. Gribov, E.M. Levin, M.G. Ryskin, *Phys. Rep.* **100**, 1 (1983).

[2] A.B. Kaidalov, *Phys. Lett.* **B116**, 459 (1982); A.B. Kaidalov, K.A. Ter-Martirosyan, *Phys. Lett.* **B117**, 247 (1982).

[3] N.S. Amelin, L.V. Bravina, *Sov. J. Nucl. Phys.* **51**, 133 (1990).

[4] V. Abramovskii, V. Gribov, O. Kancheli, *Sov. J. Nucl. Phys.* **18**, 308 (1974).

[5] J. Bleibel *et al.*, `arXiv:1011.2703 [hep-ph]`.

[6] L.V. Bravina *et al.*, *Phys. Rev.* **C60**, 044905 (1999); E.E. Zabrodin *et al.*, *Phys. Lett.* **B508**, 184 (2001).

[7] R.D. Field, R.P. Feynman, *Nucl. Phys.* **B136**, 1 (1978).

[8] A. Bialas, M. Gyulassy, *Nucl. Phys.* **B291**, 793 (1987).

[9] G.J. Alner *et al.* [UA5 Collab.], *Phys. Rep.* **154**, 247 (1987).

[10] G. Arnison *et al.* [UA1 Collab.], *Phys. Lett.* **B118**, 167 (1982); C. Albajar *et al.* [UA1 Collab.], *Nucl. Phys.* **B335**, 261 (1990).

[11] F. Abe *et al.* [CDF Collab.], *Phys. Rev. Lett.* **61**, 1819 (1988); *Phys. Rev.* **D41**, 2330 (1990).

[12] K. Aamodt *et al.* [ALICE Collab.], *Eur. Phys. J.* **C68**, 89 (2010); **C68**, 345 (2010); *Phys. Lett.* **B693**, 53 (2010).

[13] K. Khachatryan *et al.* [CMS Collab.], *J. High Energy Phys.* **1002**, 041 (2010); *Phys. Rev. Lett.* **105**, 022002 (2010).

[14] M.I. Podgoretsky, *Fiz. Elem. Chast. Atom. Yadra* **20**, 628 (1989) (in Russian).

[15] R. Lednicky, *Phys. Atom. Nucl.* **67**, 72 (2004).

[16] K. Aamodt *et al.* [ALICE Collab.], *Phys. Rev.* **D82**, 052001 (2010).

[17] M.S. Nilsson *et al.*, *Phys. Rev.* **D84**, 054006 (2011).

[18] D. d'Enterria *et al.*, *Eur. Phys. J.* **C66**, 173 (2010).

[19] R. Kolevatov, *Eur. Phys. J.* **C68**, 513 (2010).